UNIVERSITY OF CALIFORNIA, SAN DIEGO

Multi-Core Beamformer for Spatio-Temporal MEG Source Activity Reconstruction

A dissertation submitted in partial satisfaction of the requirements for the degree Doctor of Philosophy

in

Bioengineering

by

Mithun Diwakar

Committee in charge:

Professor Gabriel Silva, Chair
Professor Ming-Xiong Huang, Co-Chair
Professor Roland Lee
Professor Thomas Liu
Professor Rebecca Theilmann
Professor Shyni Varghese

2011

The Dissertation of Mithun Diwakar is approved, and it is acceptable in quality and form for publication on microfilm and electronically:

Co-Chair

Chair

University of California, San Diego

2011

DEDICATION

I would like to dedicate this manuscript to all of the people that have supported me scientifically and emotionally during the last few years. In particular, I would like to thank Professor Ming-Xiong Huang for his constant availability and desire to answer any and every question I posed to him. I would also like to thank my father, Dr. Ramachandra Diwakar, for providing me all the inspiration I have ever needed to succeed as a scientist. I would like to thank the love of my life, Ms. Aileen Ung, for never giving up on me and always being there for me through thick and thin. Finally, I would like to thank my wonderful brother, Mr. Manu Diwakar, and my late mother, Mrs. Shobadevi Diwakar. Though her life was cut short, she gave me the best childhood any person could ever hope for and she is always with me. Thank you.

TABLE OF CONTENTS

LIST OF FIGURES

LIST OF TABLES

ACKNOWLEDGEMENTS

I would like to acknowledge Professor Ming-Xiong Huang, Professor Gabriel Silva, and Professor Roland Lee for their support as members of my doctoral committee and the members of the MEG group for help with my research. Finally, I would like to thank Omer Tal for working closely with me on my work.

Chapter 2, in part, is a reprint of the material as it appears in NeuroImage 54, pp. 253-263, 2011. Diwakar, Mithun; Huang, Ming-Xiong; Srinivasan, Ramesh; Harrington; Deborah L.; Robb, Ashley; Angeles, Annemarie; Muzzatti, Laura; Pakdaman, Reza; Song, Tao; Theilmann, Rebecca J.; Lee, Roland R. The dissertation author was the co-first author of this publication.

Chapter 3, in part, is a reprint of the material as it appears in NeuroImage 56, pp. 1918-1928, 2011. Diwakar, Mithun; Tal, Omer; Liu, Thomas T.; Harrington, Deborah L.; Srinivasan, Ramesh; Muzzatti, Laura; Song, Tao; Theilmann, Rebecca J.; Lee, Roland R.; Huang, Ming-Xiong. The dissertation author was the co-first author of this publication.

Chapter 4, in part, has been submitted for publication of the material as it may appear in NeuroImage, 2011. Tal, Omer; Diwakar, Mithun; Liu, Thomas T.; Harrington, Deborah L.; Lee, Roland R.; Muzzatti, Laura; Theilmann, Rebecca J.; Srinivasan, Ramesh; Huang, Ming-Xiong. The dissertation author was the co-first author of this material.

VITA

2004-2006	Teaching Assistant, California Institute of Technology
2006	Bachelor of Science, California Institute of Technology
2008-2010	Graduate Student Instructor, University of California, San Diego
2011	Doctor of Philosophy, University of California, San Diego
2014	Doctor of Medicine (Expected), University of California, San Diego

PUBLICATIONS

Diwakar, M., Huang, M.X., Srinivasan, R., Harrington, D.L., Robb, A., Angeles, A., Muzzatti, L., Pakdaman, R., Song., T., Theilmann, R.J., Lee, R.R., 2011a. Dual-Core Beamformer for obtaining highly correlated neuronal networks in MEG. NeuroImage 54, 253-263.

Diwakar, M., Tal, O., Liu, T.T, Harrington, D.L., Srinivasan, R., Muzzatti, L., Song, T., Theilmann, R.J., Lee, R.R., Huang, M.X., 2011b. Accurate Reconstruction of Temporal Correlation for Neuronal Sources using the Enhanced Dual-core MEG Beamformer. NeuroImage 56, 1918-1928.

ABSTRACT OF THE DISSERTATION

Multi-Core Beamformer for Spatio-Temporal MEG Source Activity Reconstruction

by

Mithun Diwakar

Doctor of Philosophy in Bioengineering

University of California, San Diego, 2011

Professor Gabriel Silva, Chair
Professor Ming-Xiong Huang, Co-Chair

Beamformer adaptive spatial filters have been used extensively in the field of magnetoencephalography (MEG) as tools to reconstruct functional activation of the brain. Conventional single beamformer techniques suffer from distortion in the presence of coherent activation of the cortex or are difficult to use due to the need of *a priori* information. These qualities present a major disadvantage to analyzing human brain responses, as coordinated functional responses require a degree of synchronous activation in different parts of the active cortex. In this dissertation, a novel beamformer technique, the multi-core beamformer, is developed that is robust to source correlation and does not require the use of *a priori* information. This novel approach is

tested in both simulated and real experiments, including auditory and median-nerve stimulation, which provide well-studied systems to gauge the effectiveness of our new technique. Simulations show that the multi-core beamformer can successfully determine source time-courses, source powers, and source locations while minimizing or eliminating the distortion present in other methods. Results from real-life experiments show that the multi-core beamformer produces physiologically meaningful solutions that agree with previous functional imaging and neurophysiology studies. The use of the multi-core beamformer is expected to greatly contribute to the analysis of MEG recordings and, in general, improve our understanding of functional brain activity.

INTRODUCTION

Magnetoencephalography (MEG) is a functional neuroimaging technique capable of detecting neuronal activation on the millisecond time scale with good spatial resolution. Though MEG is a relatively new technology, it has already improved our understanding of the human brain in both states of health and disease. MEG has been used for functional mapping of the brain during various tasks designed to test somatosensory, motor, auditory, visual, language, attention, and memory function. In states of disease, MEG has played an important role in developing our understanding of Schizophrenia, Traumatic Brain Injury (TBI), Stroke, Autism, Alzheimer's disease, and Post-traumatic Stress Disorder (PTSD) (Huang et al., 2009; Huang et al., 2010; Hunter et al., 2011; Tsiaras et al., 2011; Wilson et al., 2011; Zamrini et al., 2011). MEG has also been routinely used in clinical settings for localizing seizure foci in epileptic patients and for pre-surgical functional mapping in patients with brain tumors.

MEG offers several advantages over other imaging modalities. Functional Magnetic Resonance Imaging (fMRI) provides a good description of neural activity in space. However, the fMRI signal is based on the BOLD response which detects the level of blood oxygenation present at each voxel. The BOLD response, while a useful indicator of increased blood flow to cortical areas during activation, is an indirect measure of neural activation. Since the time-resolution of the BOLD response is in seconds, fMRI has

trouble detecting different sequences of neuronal activity in time domain and differentiating bands of brain oscillations in frequency domain. Detecting such properties of brain activity is highly important for understanding normal brain function. To achieve such goals, high time-resolution functional imaging is needed. Electroencephalography (EEG) is capable of millisecond temporal resolution through directly detecting neuronal activity by means of the scalp potential. However, EEG suffers from poor spatial resolution due to the spatial distortion of head tissues and low conductivity of the skull. MEG, on the other hand, directly detects neuronal activity (i.e. neuronal current) via neuronal magnetic fields with millisecond time resolution and has better spatial resolution than EEG since the magnetic permeability of the head is equal to that of free space (i.e. no distortion due to head tissues) (Hamalainen et al., 1993).

The most challenging issue of MEG is determining a solution for the neuronal source configuration in the brain (MEG inverse problem) using the sensor-space MEG measurements. In fact, the MEG inverse problem has no unique solution for given sets of magnetic measurements. Because of this, additional constraints on the neuronal sources (source models) are needed to make the MEG inverse solution unique. The viability of a given MEG source reconstruction technique (source model) directly impacts the general applicability of MEG to studying neural activity in both health and disease.

Thus, the development of different techniques of source localization and activity reconstruction is an active and important field of research in MEG.

One popular reconstruction method, the beamformer adaptive spatial filter, has been used extensively in MEG studies. Such conventional beamformer approaches assume different neuronal generators are *uncorrelated.* As a result, these beamformer techniques suffer from time-course distortion and source power suppression in the presence of coherent activity in the brain. In fact, fully correlated generators are completely missed during source localization (Van Drongelen et al., 1996; Van Veen et al., 1997; Robinson and Vrba, 1998; Sekihara et al., 2004). This poses a serious disadvantage as neural communication often requires coherent activity between different parts of the brain. Nonetheless, the beamformer has been widely used in brain connectivity studies (Brookes et al., 2011; Mantini et al., 2011).

This dissertation describes the development of a new beamformer, termed the multi-core beamformer (MCBF), an adaptive spatial filter capable of reconstructing the activities of multiple correlated sources without source suppression and without *a priori* information on source activity and location (Diwakar et al., 2011a; Diwakar et al., 2011b). First, a background chapter is presented to familiarize the reader with the MEG system, basic MEG physics, and the mathematics of beamformer adaptive spatial filters. Next, each step of the development of the MCBF, along with supporting results from both

simulation and real data, is presented. It is hoped that use of the MCBF spatial filter in MEG analyses will improve our understanding of brain activity by providing a better estimation of true source activity than conventional beamformer technologies.

References

Brookes, M.J., Hale, J.R., Zumer, J.M., Stevenson, C.M., Francis, S.T., Barnes, G.R., Owen, J.P., Morris, P.G., Nagarajan, S.S., 2011. Measuring functional connectivity using MEG: methodology and comparison with fcMRI. NeuroImage 56, 1082-1104.

Diwakar, M., Huang, M.X., Srinivasan, R., Harrington, D.L., Robb, A., Angeles, A., Muzzatti, L., Pakdaman, R., Song., T., Theilmann, R.J., Lee, R.R., 2011a. Dual-Core Beamformer for obtaining highly correlated neuronal networks in MEG. NeuroImage 54, 253-263.

Diwakar, M., Tal, O., Liu, T.T, Harrington, D.L., Srinivasan, R., Muzzatti, L., Song, T., Theilmann, R.J., Lee, R.R., Huang, M.X., 2011b. Accurate Reconstruction of Temporal Correlation for Neuronal Sources using the Enhanced Dual-core MEG Beamformer. NeuroImage 56, 1918-1928.

Hamalainen, M.S., Hari, R., Ilmoniemi, R.J., Knuutila, J., Lounasmaa, O., 1993. Magnetoencephalography – theory, instrumentation, and applications to noninvasive studies of the working human brain. Rev. Mod. Physics 65, 413-497.

Huang, M.X., Lee, R.R., Gaa, K.M., Song, T., Harrington, D.L., Loh, C., Theilmann, R.J., Edgar, J.C., Miller, G.A., Canive, J.M., Granholm, E., 2010. Somatosensory System Deficits in Schizophrenia Revealed by MEG during a Median-Nerve Oddball Task. Brain Topography 23 (1), 82-104.

Huang, M.X., Theilmann, R.J., Robb, A., Angeles, A., Nichols, S., Drake, A., D'Andrea, J., Levy, M., Holland, M., Song, T., Ge, S., Hwang, E., Yoo, K., Cui, L., Baker, D.G., Trauner, D., Coimbra, R., Lee, R.R., 2009. Integrated imaging approach with MEG and DTI to detect mild traumatic brain injury in military and civilian patients. J. Neurotrauma 26, 1213-1226.

Hunter, M., Villarreal, G., McHaffie, G.R., Jimenez, B., Smith, A.K., Calais, L.A., Hanlon, F., Thoma, R.J., Canive, J.M., 2011. Lateralized abnormalities in auditory M50 sensory gating and cortical thickness of the superior temporal gyrus in post-traumatic stress disorder: preliminary results. Psychiatry Res. 191, 138-144.

Mantini, D., Della Penna, S., Marzetti, L., de Pasquale, F., Pizzella, V.,

Corbetta, M., Romani, G.L., 2011. A signal-processing pipeline for magnetoencephalography resting-state networks. Brain Connectivity 1, 49-59.

Robinson, S., Vrba, J., 1998. Functional neuroimaging by synthetic aperture magnetometry. In: Yoshimoto, T., Kotani, M., Kuriki, S., Karibe, H., Nakasato, N. (Eds.), Recent Advances in Biomagnetism. Tohoku Univ. Press, Sendai, pp. 302-305.

Sekihara, K., Nagarajan, S., Poeppel, D., Marantz, A., 2004. Asymptotic SNR of scalar and vector minimum-variance beamformers for neuromagnetic source reconstruction. IEEE Trans. Biomed.Eng. 51 (10), 1726-1733.

Tsiaras, V., Simos, P.G., Rezaie, R., Sheth, B.R., Garyfallidis, E., Castillo, E.M., Papanicolaou, A.C., 2011. Extracting biomarkers of autism from MEG resting-state functional connectivity networks. Comput. Biol. Med. May 16, Epub ahead of print.

Van Drongelen, W., Yuchtman, M., Van Veen, B.D., Van Huffelen, A.C., 1996. A spatial filtering technique to detect and localize multiple sources in the brain. Brain Topogr. 9 (1), 39-49.

Van Veen, B.D., Van Drognelen, W., Yuchtman, M., Suzuku, A., 1997. Localisation of brain electrical activity via linearly constrained minimum variance spatial filtering. IEEE Trans. Biomed. Eng. 44 (9).

Wilson, T.W., Fleischer, A., Archer, D., Hayasaka, S., Sawaki, L., 2011. Oscillatory MEG motor activity reflects therapy-related plasticity in stroke patients. Neurorehabil. Neural Repair 25, 188-193.

Zamrini, E., Maestu, F., Pekkonen, E., Funke, M., Makela, J., Riley, M., Bajo, R., Sudre, G., Fernandez, A., Castellanos, N., Del Pozo, F., Stam, C.J., van Dijk, B.W., Bagic, A., Becker, J.T., 2011. Magnetoencephalography as a putative biomarker for Alzheimer's disease. Int. J. Alzheimers Dis. Apr 10, 280289.

CHAPTER 1

Background on Magnetoencephalography

1.1 Neuronal Generation of Magnetic Field Signals

The cellular mechanisms responsible for generating neuronal signals must first be examined in any in-depth discussion of Magnetoencephalography (MEG). The human brain is composed of, roughly, two distinct types of tissue. White matter, which lies under the cortical surface, contains neuronal support cells as well as axons, the cellular projections responsible for propagating signals to downstream neurons. The axon is a single, long portion of the cell which carries the nerve impulse away from the body (soma) of the cell, generally located in the gray matter, the second type of tissue. Gray matter mainly resides in the cortex, a thin layer at the surface of the brain, and is also present in deeper subcortical structures. Gray matter consists of neural support cells (glia), neuron bodies (somas), and dendrites, the neural cell structure responsible for receiving nerve impulses. The cortical surface, or gray matter, has a total surface area of about 2500 cm^2 and fits in the skull due to a highly invaginated and folded structure. The hills of the cortex (gyri) and the valleys (sulci) allow the human brain to house many more soma than would a smooth surface (Kandel et al., 2000).

Interestingly, the structure of the cortex is conserved extremely well across a particular species and has similar structure between species. Many

of the important functional areas of the human cortex have been mapped out through various functional studies such as cortical electrode placement, functional magnetic resonance imaging (fMRI), positron emission tomography (PET), and MEG. Furthermore, many surface and depth cortical electrode experiments performed on animal subjects are directly applicable to the human brain due to conservation of structure.

The anatomy of the head is very important in the field of MEG. Cellular structures determine how incredibly small electrical currents sum up to create a detectable magnetic field. Furthermore, the macroscopic anatomy is important as it provides structure to determine electromagnetic field propagation through various layers of electrical conductivity. Finally, good knowledge of functional anatomy can provide *a priori* information for aid in solving the MEG inverse problem (Hillebrand and Barnes, 2003).

Important electrical currents are present in both the axons and dendrites of neurons while they are active. The axonal current, which is responsible for sending nerve impulses to downstream or efferent neurons, is generated through active ion exchange, requiring the presence of a membrane potential maintained by expenditure of adenosine triphosphate (ATP). The axonal current is extremely fast, having a typical duration of 1 ms. The current is quadrupolar in nature, propagating along the axon in all longitudinal and radial directions. Once the axonal current reaches the tip of the axon, neurotransmitters are released across the synaptic cleft to bind to

receptors on the dendritic portion of the efferent neuron. The bound receptors then allow an influx of sodium ions which raises the membrane potential in the dendrites. This membrane potential is passively propagated along the dendrite until it reaches the soma. Since the dendritic (post-synaptic) current is not actively generated, it is much slower, typically lasting tens of milliseconds. If the membrane potential near the junction of the soma and the axon (axon hillock) reaches a high enough level, a new action potential is generated along the axon (Hamalainen et al., 1993, Kandel et al., 2000).

The magnetic fields produced by these neuronal currents can be predicted by the quasi-static approximations to the Maxwell Field Equations. Because of the quadrupolar nature of the axonal current and the resulting spatial cancellation, the magnetic field intensity decreases with distance from the source as $1/r^3$. Due to this rapid reduction in magnetic field intensity and the fast nature of the action potential, axonal currents in white matter are not detectable by electroencephalography (EEG) and MEG.

The passively generated magnetic field from the dipolar post-synaptic current, however, reduces with distance as $1/r^2$. Furthermore, the microscopic structure of the cortical gray matter shows it is composed of multiple highly-organized layers of neurons. The pyramidal cells in layers 4 through 6 of the cortex, in particular, are arranged in a parallel orientation and fire synchronously in large functional groups (~100,000 neurons) known as cortical columns. The spatial organization of these columns allows for

temporal and spatial summation of the post-synaptic current, generating a much larger magnetic field for a cortical patch than for a single neuron. Thus, due to the combination of these factors, post-synaptic currents are the driving force behind measurable MEG and EEG signals. Also, since these currents are primarily located within the cortical gray matter, MEG is most sensitive to activity in the cortex (Hamalainen et al., 1993; Kandel et al., 2000).

1.2 MEG Design and Detection of Magnetic Field

The typical magnetic field strength generated by an active cortical patch of neurons is 50-500 femtoTesla, about 8 to 9 orders of magnitude smaller than the earth's own electromagnetic field. Thus, it is necessary to have extremely sensitive magnetic field detectors in addition to a shielded environment suitable for blocking out the earth's static field. The detectors used in magnetoencephalography are superconducting quantum interference devices or SQUIDs. SQUIDs are composed of superconducting rings with one or more weak junctions that limit current flow to an upper bound called the maximum critical current. In order to be superconducting, the SQUIDs must be at or below the critical superconducting temperature. Cooling is achieved through the use of a liquid Helium bath which has a temperature of less than 4 Kelvin.

The neuromagnetic field is typically brought to the SQUIDs through the use of flux transformers. Flux transformers are pickup coils which are used to

limit the contribution of the background field to the signal detected by the SQUIDs. Two types of flux transformers are used in MEG: gradiometers and magnetometers. Gradiometers are mainly sensitive to nearby magnetic fields (i.e. the neuronal magnetic fields generated by the cortex), but less sensitive to magnetic fields from remote sources (i.e. subcortical gray matter and artifacts from generators far from the sensor). In contrast, magnetometers are sensitive to both nearby and remote sources.

To further ensure that static fields generated by the earth, power lines, passing cars, etc. do not influence the neuromagnetic measurements, MEG machines are housed in shielded rooms. At the University of California, San Diego (UCSD), the MEG situated at the Radiology Imaging Laboratory has a multiple layer shielded room with shielding factors of 65, 73, 108, and 160 dB at 0.01, 0.1, 1, and 10 Hz respectively. The use of a well-shielded room is essential in MEG as it significantly increases the signal-to-noise ratio (SNR) of the magnetic recordings.

Though a single SQUID and flux transformer may be used to record the magnetic field produced by neural activity, such a system is not ideal because it requires moving the sensor around the head to sample a whole magnetic field map. In many cases, such as in the detection of epileptic discharges, events are not easily reproducible and do not allow the practice of moving the sensor to different locations. Thus, recent developments in MEG design have focused on implementing multiple SQUID and flux transformer arrays that

provide good whole brain coverage. Such a system is much preferable as the entire local magnetic field surrounding the skull can be detected simultaneously, greatly reducing the time required to gather enough information for neuronal activity reconstruction. The MEG housed at UCSD is an Elekta VectorView system containing 102 magnetometers and 204 gradiometers, which provides whole-head coverage and more than adequate sites of measurement for accurate reconstruction of brain activity.

1.3 Forward Modeling

The previous sections illustrated how magnetic fields are generated by the brain during cellular activity and how we may design a system to detect these weak fields. However, we do not yet have a description of the characteristics of these generated fields. Maxwell's Field Equations serve as the basis for computing these generated fields. If the conductor profile of the head is known, along with the neuronal current distribution, Maxwell's equations may be used to straightforwardly compute the expected magnetic field pattern at the sensor locations.

The field equations are simplified in the case of MEG in two ways. First, the magnetic permeability of tissue is the same as free space. Second, we may employ the quasi-static approximation to Maxwell's equations. In the quasi-static approximation, induction terms which depend on the time-derivative of the electric and magnetic fields are assumed to be zero. This

assumption is valid because neuronal activity is generally less than 100 Hz, resulting in induced fields that are too small to play a significant role in the sensor measurements (Hamalainen et al., 1993).

When applying the quasi-static field equations to the brain, the neuronal currents are split into two components. The primary current is the current generated by the dendrites in active cortical patches and is the primary measure of neural activity in both MEG and EEG. Since the charges in the current must complete a circuit to maintain charge neutrality, current propagates through the general medium in a distributed fashion (return current). The volume current, $\boldsymbol{J}^v(\boldsymbol{r})$, is described by the electric field, $\boldsymbol{E}(\boldsymbol{r})$, and conductivity profile, $\sigma(\boldsymbol{r})$ (Hamalainen et al., 1993):

$$\boldsymbol{J}^v(\boldsymbol{r}) = \sigma(\boldsymbol{r})\boldsymbol{E}(\boldsymbol{r}) \tag{1.1}$$

The total current density, $\boldsymbol{J}(\boldsymbol{r})$, is composed of the primary current, $\boldsymbol{J}^p(\boldsymbol{r})$, and the return current:

$$\boldsymbol{J}(\boldsymbol{r}) = \boldsymbol{J}^p(\boldsymbol{r}) + \sigma(\boldsymbol{r})\boldsymbol{E}(\boldsymbol{r}) = \boldsymbol{J}^p(\boldsymbol{r}) - \sigma(\boldsymbol{r})\nabla V(\boldsymbol{r}) \tag{1.2}$$

In the quasi-static approximation, the divergence of the total current density is zero. Simplifying Equation 1.2 under these conditions yields:

$$\nabla \cdot (\sigma \nabla V) = \nabla \cdot \boldsymbol{J}^p \tag{1.3}$$

In developing the forward model, we are primarily interested in developing a relationship between the primary currents (actual source activity)

and the magnetic field distribution at each sensor while taking into account the contributions from the volume current. Solving Equation 1.3 for the electric potential allows straightforward computation of the magnetic field distribution from the primary current using the Ampere-LaPlace Law:

$$\boldsymbol{B}(\boldsymbol{r}) = \frac{\mu_0}{4\pi}\int \left(\boldsymbol{J}^p(\boldsymbol{r}') + V(\boldsymbol{r}')\nabla'\sigma(\boldsymbol{r}')\right) \times \frac{\boldsymbol{R}}{R^3}\, dv' ; \;\; \boldsymbol{R} = \boldsymbol{r} - \boldsymbol{r}' \tag{1.4}$$

Primed coordinates indicate source space. In order to solve Equation 1.3 for the electric potential, it is necessary to have a description of the conductivity (head model) and a model for the primary currents, $\boldsymbol{J}^p$. Two common head models, the spherical head model and boundary element method (BEM) head model will be described in more detail in the coming sections. Using Equation 1.4, a lead-field matrix may be developed that describes the gain at each sensor location to dipolar currents modeled across a source grid at various locations.

1.3.1 Equivalent Current Dipole Model (ECD)

Since MEG detects signals from dendritic current, the continuous primary current can be modeled as a set of discrete Dirac delta function current dipoles (ECD or equivalent current dipole):

$$\boldsymbol{J}^p(\boldsymbol{r}) = \boldsymbol{Q}\delta\left(\boldsymbol{r} - \boldsymbol{r}_{\boldsymbol{Q}}\right) \tag{1.5}$$

$\boldsymbol{Q}$ describes the current strength and orientation while $\boldsymbol{r_Q}$ specifies the spatial location of the ECD. Though, in reality, the current dipole generated by a cortical patch has a finite thickness, the current dipole model provides a simpler mathematical tool for both the forward and inverse problems.

1.3.2 Spherical Head Model

Though, realistically, the human skull geometry is complex with different layers of conductivity, a simple and useful approximation is the spherical head model. The spherical head model uses two, three, or more concentric spherical shells of conductivity for computation of Maxwell's equations. Computation of the forward model from such a system can be accomplished with simple analytic expressions, greatly reducing computational time. The magnetic field response to a current dipole $\boldsymbol{Q}$ (described in Section 1.3.1) is given by the Sarvas Formula (Ilmoniemi et al., 1985; Sarvas, 1987):

$$\boldsymbol{B}(\boldsymbol{r}) = \frac{\mu_0}{4\pi}\frac{F\boldsymbol{Q}\times\boldsymbol{r_Q} - (\boldsymbol{Q}\times\boldsymbol{r_Q}\cdot\boldsymbol{r})\nabla F(\boldsymbol{r},\boldsymbol{r_Q})}{F(\boldsymbol{r},\boldsymbol{r_Q})^2} \tag{1.6}$$

where

$$F(\boldsymbol{r},\boldsymbol{r_Q}) = a(ra + r^2 - \boldsymbol{r_Q}\cdot\boldsymbol{r}) \tag{1.7}$$

with $\boldsymbol{a} = (\boldsymbol{r} - \boldsymbol{r_Q}),\ a = |\boldsymbol{a}|,\ r = |\boldsymbol{r}|$

The number of concentric spherical shells is irrelevant since the forward solution to the spherical MEG head model is independent of the conductivity

values of each individual shell and is only a function of the center of the sphere. Furthermore, Equation 1.6 also implies that electric potential does not need to be explicitly computed for the spherical head model. Though the forward model computed through the spherical head conductor geometry is not fully accurate, especially in regions that do not conform well to the sphere shape, the model is generally accurate enough to use for real magnetic measurements.

Because of the spherical geometry, radially directed currents do not affect the magnetic field pattern outside of the conductor (the cross-products in Equation 1.6 vanish) (Grynszpan and Geselowitz, 1973; Hamalainen et al., 1993). Thus, MEG is generally insensitive to radially directed dipolar currents, but rather mostly detects non-radially oriented currents. In terms of brain anatomy, this means that source activity in the gyri is difficult to detect, whereas source activity in the sulci are readily detectable (Hillebrand and Barnes, 2002). Fortunately, most of the important functional regions of the brain contain plenty of activity in the sulci, ensuring that MEG is a useful functional tool.

1.3.3 BEM Head Model

The BEM head model attempts to construct the MEG forward model through the use of a piecewise homogenous conductor description. Typically, this realistic head model uses two layers whose boundary is the inner-skull

surface, which is usually obtained by segmentation of structural MRI images. Unlike the spherical head model, the BEM model requires numerical computation of the electric potential on the boundaries between layers. Though computationally more intensive, the BEM model provides a realistic subject-by-subject model that does not suffer from distortions near regions, such as the inferior frontal lobe, that are not well described by a spherical shape. The work presented in this dissertation uses a BEM forward model developed in our laboratory (Meijs et al., 1987; Hamalainen and Sarvas, 1989; Mosher et al., 1999; Huang et al., 2007).

The BEM head model assumes a piecewise homogenous conductor model in which the conductivity of each layer is constant and the gradient of the conductance is non-zero only at the layer boundaries. The layers or regions of conductivity can be denoted $G_i, i = 1, \cdots, m$, with their boundaries denoted ∂G_i, and the surfaces between layers G_i and G_j denoted S_{ij}. We may re-write Equation 1.4 as the sum of two integrals:

$$\boldsymbol{B}(\boldsymbol{r}) = \frac{\mu_0}{4\pi}\int \boldsymbol{J}^p(\boldsymbol{r}') \times \frac{\boldsymbol{R}}{R^3}\,dv' + \frac{\mu_0}{4\pi}\int V(\boldsymbol{r}')\nabla'\sigma(\boldsymbol{r}') \times \frac{\boldsymbol{R}}{R^3}\,dv' \qquad (1.8)$$

Defining $\boldsymbol{B}_0(\boldsymbol{r}) = \frac{\mu_0}{4\pi}\int \boldsymbol{J}^p(\boldsymbol{r}') \times \frac{\boldsymbol{R}}{R^3}\,dv'$ and writing the second integral in Equation 1.8 as a sum of piecewise integrals while using the identity $-\nabla \times (V\nabla\sigma) = \nabla\sigma \times \nabla V = \nabla \times (\sigma\nabla \mathrm{V})$ yields:

$$\boldsymbol{B}(\boldsymbol{r}) = \boldsymbol{B}_0(\boldsymbol{r}) - \frac{\mu_0}{4\pi}\sum_{i=1}^{m}\sigma_i \int_{G_i} \nabla' \mathrm{V} \times \frac{\boldsymbol{R}}{R^3}\, dv' \tag{1.9}$$

Converting the volume integral in Equation 1.9 into a surface integral yields Geselowitz' formula (Geselowitz, 1970):

$$\boldsymbol{B}(\boldsymbol{r}) = \boldsymbol{B}_0(\boldsymbol{r}) + \frac{\mu_0}{4\pi}\sum_{ij}(\sigma_i - \sigma_j) \int_{S_{ij}} V(\boldsymbol{r}') \frac{\boldsymbol{R}}{R^3} \times d\boldsymbol{S}'_{ij} \tag{1.10}$$

Thus, computation of the magnetic fields at the sensors first requires computation of the potential, $V(\boldsymbol{r}')$, at all surfaces S_{ij}. Applying Equation 1.3 to these boundary constraints and letting $\boldsymbol{r}$ approach a value on the boundary yields an expression that can be used to numerically compute these surface potentials (Geselowitz, 1967; Vladimirov, 1971):

$$\big(\sigma_i + \sigma_j\big)V(\boldsymbol{r}) = 2\sigma_0 V_0(\boldsymbol{r}) - \frac{1}{2\pi}\sum_{ij}\big(\sigma_i - \sigma_j\big) \int_{S_{ij}} V(\boldsymbol{r}') \frac{\boldsymbol{R}}{R^3} \cdot d\boldsymbol{S}'_{ij} \tag{1.11}$$

where $\sigma_0 = 1/(\Omega m)$ and V_0 is the potential due to the primary current in an infinite homogenous medium:

$$V_0 = \frac{1}{4\pi\sigma_0} \int_G \frac{\nabla' \cdot \boldsymbol{J}^p}{\boldsymbol{R}}\, dv' \tag{1.12}$$

1.3.4 MEG Signal Equation

Let $\boldsymbol{b}(t)$ be an *m x 1* vector of sensor measurements at time *t*, $\boldsymbol{n}(t)$ be an *m x 1* vector of sensor noise measurements, $\boldsymbol{s}(t)$ be a *2p x 1* matrix of vector source amplitudes, and $\tilde{\boldsymbol{s}}(t)$ be a *p x 1* matrix of scalar source amplitudes, where *m* is the number of sensors and *p* is the number of pre-defined dipolar sources. Let the lead-field matrix defined in two directions θ and ϕ for the i^{th} source be denoted by the *m x 2* matrix $\boldsymbol{L}_i = [\boldsymbol{l}_{\theta,i} \quad \boldsymbol{l}_{\phi,i}]$. In the spherical MEG forward head model, θ and ϕ represent the two tangential orientations for each dipole location, whereas in a realistic MEG forward model using the boundary element method (BEM), the θ and ϕ orientations are obtained as the two dominant orientations from the singular value decomposition (SVD) of the *m x 3* lead-field matrix for each dipole, as previously documented (Huang et. al., 2006). If the orientations are known, the vector lead-field matrix may be simplified into the *m x 1* scalar lead-field vector $\boldsymbol{l}_i = \boldsymbol{L}_i\overline{\boldsymbol{\eta}}_{\boldsymbol{i}}$, where $\overline{\boldsymbol{\eta}}_{\boldsymbol{i}}$ are the unit orientation vectors in the θ and ϕ directions.

The lead-fields contain the multiplicative coefficients that describe the magnetic field pattern imparted to the sensors by current dipoles located at each of the *p* locations as computed by the forward model (Equation 1.5). The vector composite lead-field matrix or gain matrix is defined as the *m x 2p* matrix $\boldsymbol{L} = [\boldsymbol{L}_1 \quad \boldsymbol{L}_2 \quad \boldsymbol{L}_3 \quad \cdots \quad \boldsymbol{L}_p]$. The scalar composite lead-field matrix is

defined as the *m x p* matrix $\tilde{\boldsymbol{L}} = [\boldsymbol{l}_1 \quad \boldsymbol{l}_2 \quad \boldsymbol{l}_3 \quad \cdots \quad \boldsymbol{l}_p]$. The MEG signal equation can be written as (vector formulation):

$$\boldsymbol{b}(t) = \boldsymbol{L}\boldsymbol{s}(t) + \boldsymbol{n}(t) \tag{1.13}$$

or equivalently as (scalar formulation):

$$\boldsymbol{b}(t) = \tilde{\boldsymbol{L}}\tilde{\boldsymbol{s}}(t) + \boldsymbol{n}(t) \tag{1.14}$$

Taking the covariance of Equation 1.13 and assuming that the noise and signal are uncorrelated leads to the covariance relationship:

$$\boldsymbol{R}_b = \boldsymbol{L}\boldsymbol{R}_s^p\boldsymbol{L}^T + \boldsymbol{R}_n \tag{1.15}$$

$\boldsymbol{R}_b$ is the *m x m* sensor covariance matrix, $\boldsymbol{R}_s^p$ is the 2*p x 2p* source covariance matrix, and $\boldsymbol{R}_n$ is the *m x m* noise covariance matrix.

1.4 Inverse Modeling for the Lead-field Approach

Up to this point, discussion has focused on the generation, detection, and prediction of magnetic field patterns in MEG. However, for MEG to be a truly useful technology, one must solve the "MEG inverse problem." The inverse problem consists of obtaining the underlying source current distribution that generates a specific magnetic field pattern at the sensors. This is of particular importance in real experiments as the only known parameters are the conductivity profile of the head, the locations of the sensors, and finally the sensor magnetic field measurements.

Unfortunately, it was shown by Helmholtz that a solution to the underlying current distribution inside a conductor cannot be determined uniquely for any given field pattern. For example, radially oriented currents are invisible to the MEG sensors. Thus, different source distributions with different radially-directed currents may satisfy a given set of sensor measurements. Due to this problem, additional constraints must be placed on the source configuration (i.e. source modeling) in order to obtain a unique solution for the source current distribution which represents brain activity.

Different constraints placed upon the system yield different solutions with different qualities. For example, the L2-minimum norm approach seeks to minimize the total source power across all *p* grid points while satisfying the original sensor recordings. L2-minimum norm approaches tend to yield spatially distributed reconstructions that have relatively low resolution. However, time-courses generated from the L2-minimum norm reconstruction are continuous in nature (Hamalainen and Ilmoniemi, 1994; Dale et al., 2000; Dale and Halgren, 2001; Marinkovic et al., 2003). The L1-minimum norm approach seeks to minimize the absolute value of the source amplitude from the *p* grid points while still fitting the sensor recordings. Such an approach yields spatially focal reconstructions with high resolution but yields discontinuous time-courses with activity oftentimes jumping from grid point to grid point (Uutela et al., 1999; Vanni and Uutela, 2000; Tesche, 2000;

Stenbacka et al., 2002; Pulvermuller et al., 2003; Osipova et al., 2005; Auranen et al., 2005; Liljestrom et al., 2005).

1.5 Scalar Single Beamformer Solution

Another approach to the inverse problem is to use the covariance matrix of the sensor recordings to design a spatial filter that individually reconstructs source activities for each grid point sequentially. Like the L1- and L2-minimum norm approaches, the spatial filtering approach has advantages and drawbacks which will be described in full detail in the coming sections. The original research presented in this dissertation focuses on developing an adaptive spatial filter for the MEG that is less susceptible to many common problems of this approach.

The basic adaptive spatial filtering approach was first described by the single beamformer (Van Drongelen et al., 1996; Van Veen et al., 1997; Robinson and Vrba, 1998; Sekihara et al., 2002). The scalar beamformer spatial filter seeks to find an *m x 1* weighting vector $\boldsymbol{w}$ for each source location such that source time-courses are reconstructed as a linear combination of the sensor waveforms. The source time-course estimate is modeled as (Van Drongelen et al., 1996; Sekihara and Nagarajan, 2008):

$$\hat{s}(t) = \boldsymbol{w}^T \boldsymbol{b}(t) \tag{1.16}$$

The source power $|\hat{s}|^2$ is given by:

$$|\hat{s}|^2 = \langle \hat{s}(t)\hat{s}(t)^T \rangle = \boldsymbol{w}^T \boldsymbol{R}_b \boldsymbol{w} \tag{1.17}$$

The scalar weighting vector ($\boldsymbol{w}$) depends on both the source location and source orientation. Though source locations can be fixed through a source grid covering the cortical space, source orientations are unknown and depend upon the nature of source activation in the brain. The minimum-variance solution for $\boldsymbol{w}$ seeks to minimize the total source power from the filter pointing location while reducing the contributions of other sources and noise to the filter output (Van Veen et al., 1997). Mathematically, this minimization is stated as:

$$\boldsymbol{w} = \arg\min_{\boldsymbol{w}} \boldsymbol{w}^T \boldsymbol{R}_b \boldsymbol{w} \text{ subject to } \boldsymbol{w}^T \boldsymbol{l} = 1 \tag{1.18}$$

The constraint $\boldsymbol{w}^T \boldsymbol{l} = 1$ ensures unit gain for the filter pointing location. The solution to this problem may be obtained by Lagrangian minimization and results in the following formulation of the weighting vector (Robinson and Vrba, 1998; Vrba and Robinson, 2001; Sekihara et al., 2004):

$$\boldsymbol{w}^T = (\boldsymbol{l}^T \boldsymbol{R}_b^{-1} \boldsymbol{l})^{-1} \boldsymbol{l}^T \boldsymbol{R}_b^{-1} \tag{1.19}$$

A source time-course for each filter pointing location is computed with Equation 1.16. Ideally, such source time-courses could be used to produce a volumetric 4-D image of brain activity spanning the whole brain. However, it is well known that signal-to-noise ratio decreases with increasing depth of sources. Furthermore, forward modeling may generate inaccurate estimates

of the lead-field at each filter pointing location. Thus, a measure of source space signal-to-noise (SNR) can be computed to aid in localizing brain activity and removing bias associated with the lead-fields. Similarly to Equation 1.17, an estimate of noise power at each location can be computed (Robinson and Vrba, 1998; Vrba and Robinson, 2001; Sekihara et al., 2004):

$$|\hat{n}|^2 = \langle \hat{n}(t)\hat{n}(t)^T \rangle = \boldsymbol{w}^T \boldsymbol{R}_n \boldsymbol{w} \tag{1.20}$$

Dividing the source power estimate by the noise power estimate, yields the traditional pseudo-Z-score, a measure of source space SNR:

$$Z_{SBF} = \frac{|\hat{s}|^2}{|\hat{n}|^2} = \frac{\boldsymbol{w}^T \boldsymbol{R}_b \boldsymbol{w}}{\boldsymbol{w}^T \boldsymbol{R}_n \boldsymbol{w}} \tag{1.21}$$

The scalar beamformer assumes that each source orientation is known. Source pseudo-Z-score and time-course estimates are contingent on the orientation chosen for the lead-fields ($\boldsymbol{l}$) and therefore the orientation chosen for the beamformer weight ($\boldsymbol{w}$). In reality, source orientation is not known *a priori*. However, choosing the correct source orientation is expected to maximize the source space SNR. Thus, the source orientation for each filter pointing location can be found through maximization of Z_{SBF} as a function of orientation ($\overline{\boldsymbol{\eta}}$):

$$Z_{SBF}^{opt} = \max_{\overline{\boldsymbol{\eta}}} (Z_{SBF}) \tag{1.22}$$

The optimized orientation can then be used to compute the optimum pseudo-Z-score Z_{SBF}^{opt} and time-course for each pointing location. Typically, non-linear search algorithms are used to compute the optimal orientations and represent a time-consuming step of source reconstruction.

1.5.1 Correlated Source Problem

The minimization step in Equation 1.18 is directly responsible for beamformer distortion in the presence of correlated sources (Sekihara and Nagarajan, 2008). Expanding the minimized expression $\boldsymbol{w}^T\boldsymbol{R}_b\boldsymbol{w}$, we find that:

$$\boldsymbol{w}^T(\boldsymbol{r}_i)\boldsymbol{R}_b\boldsymbol{w}(\boldsymbol{r}_i)$$

$$= \langle \left[\boldsymbol{w}^T(\boldsymbol{r}_i)\sum_{j=1}^{p} s(\boldsymbol{r}_j,t)\boldsymbol{l}(\boldsymbol{r}_j)\right]\left[\boldsymbol{w}^T(\boldsymbol{r}_i)\sum_{j=1}^{p} s(\boldsymbol{r}_j,t)\boldsymbol{l}(\boldsymbol{r}_j)\right]^T \rangle \qquad (1.23)$$

By applying the unit-gain constraint, the above expression reduces to:

$$\boldsymbol{w}^T(\boldsymbol{r}_i)\boldsymbol{R}_b\boldsymbol{w}(\boldsymbol{r}_i) = \langle s(\boldsymbol{r}_i,t)\rangle^2$$

$$+\sum_{i\neq j}\langle s(\boldsymbol{r}_j,t)\rangle^2\left|\boldsymbol{w}^T(\boldsymbol{r}_i)\boldsymbol{l}(\boldsymbol{r}_j)\right|^2$$

$$+\sum_{j_1\neq j_2}\langle s(\boldsymbol{r}_{j_1},t)s(\boldsymbol{r}_{j_2},t)\rangle\boldsymbol{w}^T(\boldsymbol{r}_i)\boldsymbol{l}(\boldsymbol{r}_{j_1})\boldsymbol{l}^T(\boldsymbol{r}_{j_2})\,\boldsymbol{w}(\boldsymbol{r}_i) \qquad (1.24)$$

The third term in the above expression only vanishes if source activities are uncorrelated, i.e. $\langle s(\boldsymbol{r}_{j_1},t)s(\boldsymbol{r}_{j_2},t)\rangle = 0$. The second term in the above expression vanishes as minimization ensures $\boldsymbol{w}^T(\boldsymbol{r}_i)\boldsymbol{l}(\boldsymbol{r}_j) = 0$. Thus, for the

beamformer weight to satisfy $\boldsymbol{w}^T(\boldsymbol{r}_i)\boldsymbol{R}_b\boldsymbol{w}(\boldsymbol{r}_i) = \langle s(\boldsymbol{r}_i, t)\rangle^2$ and only reflect the intended source power, source activities must be uncorrelated. When source activities are correlated, the third term does not vanish and creates significant distortion in both power and time-course estimates at the filter pointing location. Since neural activity typically requires a degree of communication and hence synchrony between active sources, application of the unmodified beamformer to real experiments does not generate ideal reconstructions of source activity.

1.6 Dual Source Beamformer

As explained in Section 1.5.1, a significant issue affecting source power and time-course estimates from the scalar single beamformer is distortion in the presence of spatially separate yet temporally correlated sources. Brookes and colleagues tackled this problem through increasing the size of the scalar single beamformer filter to account for two locations simultaneously. This approach allows two temporally correlated sources to be modeled simultaneously in order to avoid power suppression and allow localization of temporally correlated sources.

The dual source beamformer (DSBF) spatial filter is designed to pass the signals of two separate spatial locations in its output (Brookes et al., 2007). The filter is designed such that it is responsive to a combined lead-field of two sources denoted $\boldsymbol{l}_{12}$:

$$\boldsymbol{l}_{12} = \alpha \boldsymbol{l}_1 + (1-\alpha)\boldsymbol{l}_2 \tag{1.25}$$

The combined lead-field for the two sources is defined as a linear combination of the individual lead-fields weighted by the weighting factor α which depends on the source power ratio of the two locations being examined. The solution to the combined dual source weighting vector $\boldsymbol{w}_{12}$ is obtained identically to the single source scalar beamformer:

$$\boldsymbol{w}_{12}^T = (\boldsymbol{l}_{12}^T \boldsymbol{R}_b^{-1} \boldsymbol{l}_{12})^{-1} \boldsymbol{l}_{12}^T \boldsymbol{R}_b^{-1} \tag{1.26}$$

The resulting scalar time-course for the two sources is given by:

$$\hat{s}(t) = \boldsymbol{w}_{12}^T \boldsymbol{b}(t) \tag{1.27}$$

The dual-source pseudo-Z-score, a measure of combined source-space SNR is given by:

$$Z_{12} = \frac{\boldsymbol{w}_{12}^T \boldsymbol{R}_b \boldsymbol{w}_{12}}{\boldsymbol{w}_{12}^T \boldsymbol{R}_n \boldsymbol{w}_{12}} \tag{1.28}$$

The dual source pseudo-Z-score is a function of the two source orientations $\overline{\boldsymbol{\eta}}_1$ and $\overline{\boldsymbol{\eta}}_2$ as well as the source power weighting factor α. In practice, time-consuming non-linear searches must be carried out over these three parameters to optimize the dual-source pseudo-Z-score for a particular combination of two source locations. Furthermore, if the two optimal source locations are not known *a priori*, a computationally expensive search must be carried out for the dual-source combination that yields the maximum Z_{12}.

Since typical source grids consist of 7000-9000 points, exhaustive computation of all possible optimized combined dual-source pseudo-Z-scores is expensive and impractical. Finally, since $\boldsymbol{l}_{12}$ is a single-ranked linear combination of lead-field vectors, individual source time-courses, power estimates, and source correlation cannot be computed with the DSBF.

1.7 Minimum Variance Vector Beamformer

The vector beamformer spatial filter seeks to find an *m x 2* weighting vector $\boldsymbol{W}$ for each source location in a pre-defined basis spanned by θ and ϕ such that source time-courses are reconstructed as a linear combination of the sensor waveforms (Van Veen et al., 1997; Robinson and Vrba, 1998; Vrba and Robinson, 2001; Sekihara et al., 2002; Sekihara et al., 2004; Sekihara and Nagarajan, 2008). The vector source time-course estimate is modeled as:

$$\hat{\boldsymbol{s}}(t) = \boldsymbol{W}^T \boldsymbol{b}(t) \tag{1.29}$$

while the scalar source time-course estimate is obtained as:

$$\hat{s}(t) = \overline{\boldsymbol{\eta}}^T \boldsymbol{W}^T \boldsymbol{b}(t) \tag{1.30}$$

$\overline{\boldsymbol{\eta}}$ is a *2 x 1* unit vector containing the source orientation. The source power $|\hat{s}|^2$ is given by:

$$|\hat{s}|^2 = \langle \hat{s}(t)\hat{s}(t)^T \rangle = \overline{\boldsymbol{\eta}}^T \boldsymbol{W}^T \boldsymbol{R}_b \boldsymbol{W} \overline{\boldsymbol{\eta}} = tr(\boldsymbol{W}^T \boldsymbol{R}_b \boldsymbol{W}) \tag{1.31}$$

The minimum-variance solution for $\boldsymbol{W}$ seeks to minimize the source power from the filter pointing location while reducing the contributions of other sources and noise to the filter output. Mathematically, this minimization is stated as:

$$\boldsymbol{W} = \arg\min_{\boldsymbol{W}} tr\{\boldsymbol{W}^T \boldsymbol{R}_b \boldsymbol{W}\} \text{ subject to } \boldsymbol{W}^T \boldsymbol{L} = \boldsymbol{I} \tag{1.32}$$

The solution to this problem may be obtained by Lagrangian minimization and results in the following formulation of the weighting vector:

$$\boldsymbol{W}^T = (\boldsymbol{L}^T \boldsymbol{R}_b^{-1} \boldsymbol{L})^{-1} \boldsymbol{L}^T \boldsymbol{R}_b^{-1} \tag{1.33}$$

Since the *2 x 2* matrix product $\boldsymbol{Q}^{-1} = \boldsymbol{W}^T \boldsymbol{R}_b \boldsymbol{W} = (\boldsymbol{L}^T \boldsymbol{R}_b^{-1} \boldsymbol{L})^{-1}$ contains source power estimates in both the θ and ϕ directions, the eigenvector corresponding to the minimum eigenvalue of $\boldsymbol{Q}^{-1}$ provides the optimum source orientation $\overline{\boldsymbol{\eta}}$ as shown previously (Sekihara et al., 2004). Thus, the vector implementation of the beamformer eliminates the need to search for source optimal orientations. A source time-course for each filter pointing location can then be computed with Equation 1.29. Since signal-to-noise ratio decreases with increasing depth of sources, and forward modeling may generate inaccurate estimates of the lead-field at each filter pointing location, a measure of source space signal-to-noise (SNR) can be computed to aid in localizing brain activity and removing bias associated with the lead-fields similarly to the

scalar beamformer. First, a *2 x 2* matrix representing the source-space SINR can be computed (Sekihara et al., 2004):

$$\boldsymbol{K}^{-1} = \frac{\boldsymbol{W}^T \boldsymbol{R}_b \boldsymbol{W}}{\boldsymbol{W}^T \boldsymbol{R}_n \boldsymbol{W}} = \frac{\boldsymbol{L}^T \boldsymbol{R}_b^{-1} \boldsymbol{R}_n \boldsymbol{R}_b^{-1} \boldsymbol{L}}{\boldsymbol{L}^T \boldsymbol{R}_b^{-1} \boldsymbol{L}} \tag{1.34}$$

The optimum pseudo-Z-score can then be straightforwardly computed as the inverse of the minimum eigenvalue of this matrix:

$$Z_{SBF}^{opt} = \left(\min\left(eig(\boldsymbol{K})\right)\right)^{-1} \tag{1.35}$$

Though the minimum variance vector beamformer handles determination of source orientation admirably, it is still subject to the same distortions created by the presence of coherent source activity as described in Section 1.5.1.

1.8 Nulling Beamformer and Coherent Source Suppression Model

The nulling beamformer (NB) and the coherent source suppression model (CSSM) are two independently developed single vector beamformer modifications designed to address the problem of correlated interference in beamformer reconstruction (Dalal et al., 2006; Hui and Leahy, 2006; Hui and Leahy, 2010; Quuran and Cheyne, 2010). The NB and CSSM modify the vector beamformer by applying additional nulling constraints to known nulling locations denoted $\boldsymbol{r}_j$. The solution to the NB is obtained by minimizing Equation 1.31 while applying the standard unit gain constraint $\boldsymbol{W}^T \boldsymbol{L} = \boldsymbol{I}$ for the

location of interest along with nulling constraints $\boldsymbol{W}^T(\boldsymbol{r}_j)\boldsymbol{L}(\boldsymbol{r}_j) = \boldsymbol{0}$. This leads to the following solution of the weighting vector:

$$\boldsymbol{W}^T = \begin{pmatrix} 1 & 0 & \boldsymbol{0} \\ 0 & 1 & \boldsymbol{0} \\ \boldsymbol{0} & \boldsymbol{0} & \boldsymbol{0} \end{pmatrix} \left(\left[\boldsymbol{L}\, \boldsymbol{L}(\boldsymbol{r}_j) \right]^T \boldsymbol{R}_b^{-1} \left[\boldsymbol{L}\, \boldsymbol{L}(\boldsymbol{r}_j) \right] \right)^{-1} \left[\boldsymbol{L}\, \boldsymbol{L}(\boldsymbol{r}_j) \right]^T \boldsymbol{R}_b^{-1} \qquad (1.36)$$

The nulling beamformer is able to successfully remove the distortion caused by correlated sources by preventing the correlated sources from having any impact on the weighting vector for the filter pointing location. Although it has been demonstrated that this method is successful, application to real experiments is difficult as *a priori* information about the nulling constraints is required. Furthermore, matrix inverses become unstable if extensive regions are chosen for nulling constraints due to loss of degrees of freedom in the system.

1.9 References

Auranen, T., Nummenmaa, A., Hamalainen, M.S., Jaaskelainen, I.P., Lampinen, J., Vehtari, A., Sams, M., 2005. Bayesian analysis of the neuromagnetic inverse problem with l(p)-norm priors. NeuroImage 26, 870-884.

Brookes, M.J., Stevenson, C.M., Barnes, G.R., Hillebrand, A., Simpson, M.I.G., Francis, S.T., Morris, P.G., 2007. Beamformer reconstruction of correlated sources using a modified source model. NeuroImage 34, 1454-1465.

Dalal, S.S., Sekihara, K., Nagarajan, S.S., 2006. Modified Beamformers for Coherent Source Region Suppression. IEEE Trans. Biomed. Eng. 53, 1357-1363.

Dale, A.M., Halgren, E., 2001. Spatiotemporal mapping of brain activity by integration of multiple imaging modalities. Curr. Opin. Neurobiol. 11, 202-208.

Dale, A.M., Liu, A.K., Fischl, B.R., Buckner, R.L., Belliveau, J.W., Lewine, J.D., Halgren, E., 2000. Dynamic statistical parametric mapping: combining fMRI and MEG for high-resolution imaging of cortical activity. Neuron 26, 55-67.

Geselowitz, D.B., 1967. On bioelectric potentials in an inhomogenous volume conductor. Biophys. J. 7, 1-11.

Geselowitz, D.B., 1970. On the magnetic field generated outside an inhomogeneous volume conductor by internal current sources. IEEE Trans. Magn. MAG-6, 346-347.

Grynszpan, F., Geselowitz, D.B., 1973. Model studies of the magnetocardiogram. Biophys. J. 13, 911-925.

Hamalainen, M.S., Hari, R., Ilmoniemi, R.J., Knuutila, J., Lounasmaa, O., 1993. Magnetoencephalography – theory, instrumentation, and applications to noninvasive studies of the working human brain. Rev. Mod. Physics 65, 413-497.

Hamalainen, M.S., Ilmoniemi, R.J., 1994. Interpreting magnetic fields of the brain: minimum norm estimates. Med. Biol. Eng. Comput. 32, 35-42.

Hamalainen, M.S., Sarvas, J., 1989. Realistic conductivity geometry model of the human head for interpretation of neuromagnetic data. IEEE Trans. Biomed. Eng. 36, 165-171.

Hillebrand, A., Barnes, G.R., 2002. A quantitative assessment of the sensitivity of whole-head MEG to activity in the adult human cortex. NeuroImage 16, 638-650.

Hillebrand, A., Barnes, G.R., 2003. The use of anatomical constraints with MEG beamformers. NeuroImage 20, 2302-2313.

Huang, M., Dale, A.M., Song, T., Halgren, E., Harrington, D.L., Podgorny, I., Canive, J.M., Lewis, S., Lee, R.R., 2006. Vector-based spatial-temporal minimum L1-norm solution for MEG. NeuroImage 31, 1025-1037.

Huang, M.X., Song, T., Hagler, D.J., Podgorny, I., Jousmaki, V., Cui, L., Gaa, K., Harrington, D.L., Dale, A.M., Lee, R.R., Elman, J., Halgren, E., 2007. A novel integrated MEG and EEG analysis method for dipolar sources. NeuroImage 37, 731-748.

Hui, H.B., Leahy, R.M., 2006. Linearly constrained MEG beamformers for MVAR modeling of cortical interactions. 3rd IEEE International Symposium on Biomedical Imaging: Nano to Macro, 2006, pp. 237–240.

Hui, H.B., Pantazis, D., Bressler, S.L., Leahy, R.M., 2010. Identifying true cortical interactions in MEG using the nulling beamformer. NeuroImage 49, 3161-3174.

Ilmoniemi, R.J., Hamalainen, M.S., Knuutila, J., 1985. “The forward and inverse problems in the spherical model” in Biomagnetism: Applications & Theory. New York, Pergamon, 278-282.

Kandel, E.R., Schwartz, J.H., Jessell, T.M., 2000. Principles of Neural Science. McGraw Hill, New York.

Liljestrom, M., Kujala, J., Jensen, O., Salmelin, R., 2005. Neuromagnetic localization of rhythmic activity in the human brain: a comparison of three methods. NeuroImage 25, 734-745.

Marinkovic, K., Dhond, R.P., Dale, A.M., Glessner, M., Carr, V., Halgren, E., 2003. Spatiotemporal dynamics of modality-specific and supra-modal word processing. Neuron 38, 487-497.

Meijs, J.W.H., Bosch, F.G.C, Peters, M.J., da Silva, F.H.L, 1987. On the magnetic field distribution generated by a dipolar current source situated in a realistically shaped compartment model of the head. Electroencephalogr. Clin. Neurophysiol. 66, 286-298.

Mosher, J.C., Leahy, R.M., Lewis, P.S., 1999. EEG and MEG: forward solutions for inverse methods. IEEE Trans. Biomed. Eng. 46, 245-259.

Osipova, D., Ahveninen, J., Jensen, O., Ylikoski, A., Pekkonen, E., 2005. Altered generation of spontaneous oscillations in Alzheimer's disease. NeuroImage 27, 835-841.

Pulvermuller, F., Shtyrov, Y., Ilmoniemi, R., 2003. Spatiotemporal dynamics of neural language processing: an MEG study using minimum-norm current estimates. NeuroImage 20, 1020-1025.

Quuran, M.A., Cheyne, D., 2010. Reconstruction of correlated brain activity with adaptive spatial filters in MEG. NeuroImage 49, 2387-2400.

Robinson, S., Vrba, J., 1998. Functional neuroimaging by synthetic aperture magnetometry. In: Yoshimoto, T., Kotani, M., Kuriki, S., Karibe, H., Nakasato, N. (Eds.), Recent Advances in Biomagnetism. Tohoku Univ. Press, Sendai, pp. 302-305.

Sarvas, J., 1987. Basic mathematical and electromagnetic concepts of the biomagnetic inverse problem. Phys. Med. Biol. 32, 11-22.

Sekihara, K., Nagarajan, S., 2008. Adaptive spatial filters for electromagnetic brain imaging. Berlin, Heidelberg: Springer-Verlag.

Sekihara, K., Nagarajan, S., Poeppel, D., Marantz, A., 2002. Performance of an MEG adaptive-beamformer technique in the presence of correlated neural activities: effects on signal intensity and time course estimates. IEEE Trans. Biomed. Eng. 49 (12), 1534-1546.

Sekihara, K., Nagarajan, S., Poeppel, D., Marantz, A., 2004. Asymptotic SNR of scalar and vector minimum-variance beamformers for neuromagnetic source reconstruction. IEEE Trans. Biomed. Eng. 51 (10), 1726-1733.

Stenbacka, L., Vanni, S., Uutela, K., Hari, R., 2002. Comparison of minimum current estimate and dipole modeling in the analysis of simulated activity in the human visual cortices. NeuroImage 16, 936-943.

Tesche, C., 2000. Evidence for somatosensory evoked responses in human temporal lobe. NeuroReport 11, 2655-2658.

Uutela, K., Hamalainen, M., Somersalo, E., 1999. Visualization of magnetoencephalographic data using minimum current estimates. NeuroImage 10, 173-180.

Van Drongelen, W., Yuchtman, M., Van Veen, B.D., Van Huffelen, A.C., 1996. A spatial filtering technique to detect and localize multiple sources in the brain. Brain Topogr. 9 (1), 39-49.

Van Veen, B.D., Van Drognelen, W., Yuchtman, M., Suzuku, A., 1997. Localisation of brain electrical activity via linearly constrained minimum variance spatial filtering. IEEE Trans. Biomed. Eng. 44 (9).

Vanni, S., Uutela, K., 2000. Foveal attention modulates responses to peripheral stimuli. J. Neurophysiol. 83, 2443-2452.

Vladimirov, V.S., 1971. Equations of Mathematical Physics. New York: Marcel Dekker.

Vrba, J., Robinson, S.E., 2001. Signal processing in magnetoencephalography. Methods 25, 249-271.

CHAPTER 2

Dual-Core Beamformer for Obtaining Highly Correlated Neuronal Networks in MEG

2.1 Abstract

The “Dual-Core Beamformer” (DCBF) is a new lead-field based MEG inverse-modeling technique designed for localizing highly-correlated networks from noisy MEG data. Conventional beamformer techniques are successful in localizing neuronal sources that are uncorrelated under poor signal-to-noise ratio (SNR) conditions. However, they fail to reconstruct multiple highly-correlated sources. Though previously published dual-beamformer techniques can successfully localize multiple correlated sources, they are computationally expensive and impractical, requiring *a priori* information. The DCBF is able to automatically calculate optimal amplitude-weighting and dipole orientation for reconstruction, greatly reducing the computational cost of the dual-beamformer technique. Paired with a modified Powell algorithm, the DCBF can quickly identify multiple sets of correlated sources contributing to the MEG signal. Through computer simulations, we show that the DCBF quickly and accurately reconstructs source locations and their time-courses under widely varying SNR, degrees of correlation, and source strengths. Simulations also show that the DCBF identifies multiple simultaneously active correlated networks. Additionally, DCBF performance was tested using MEG data in

humans. In an auditory task, the DCBF localized and reconstructed highly-correlated left and right auditory responses. In a median-nerve stimulation task, the DCBF identified multiple meaningful networks of activation without any *a priori* information. Altogether, our results indicate that the DCBF is an effective and valuable tool for reconstructing correlated networks of neural activity from MEG recordings.

2.2 Introduction

The *beamformer methodology* is a spatial-filtering approach wherein the MEG sensor signal is filtered by different beams based on lead-field vectors corresponding to specific source-grid points (Robinson and Vrba, 1998; Sekihara et al., 2002a; Van Drongelen et al., 1996; Van Veen et al., 1997). Each of these operations generates a pseudo-Z-statistic, which can be maximized to find the most highly-contributing source-grid dipoles. The beamformer method has low computational cost, although the orientation angle of each dipole must be optimized. The beamformer approach generally works well for MEG data with a low SNR. However, the conventional beamformer suppresses source-power estimates from source-grid dipoles that have highly correlated time-courses, as the method assumes that source time-courses from different generators are uncorrelated (Van Veen et al., 1997; Sekihara et al., 2002b). Variants of the beamformer method, including the *coherently combining signal-to-interference plus noise ratio* (CC-SINR) beamformer and the *constant modulus algorithm* (CMA) beamformer, address

reconstruction of correlated sources, but have been met with moderate success (Kim et al., 2006; Nguyen and Ding, 1997). Likewise, the *coherent source suppression model* (CCSM) and the independently developed *nulling beamformer* (NB) accurately reconstruct correlated sources but require *a priori* information of interfering source locations. Furthermore, all sources cannot be simultaneously identified since correlated sources are suppressed to reconstruct a single source of interest (Dalal et al., 2006; Hui and Leahy, 2006; Hui and Leahy, 2010; Quuran and Cheyne, 2010).

Brookes et al. developed a dual-beamformer approach to address the problem of identifying highly-correlated generators by constructing a spatial filter from a linear combination of lead-field vectors from two source dipoles (Brookes et al., 2007). Two source dipoles that generate a signal can be found by non-linearly optimizing the orientation angles of the two source dipoles, optimizing the weighting between the two sources, and searching over all combinations of source dipoles. This approach has a high computational cost, which greatly limits its application in practice. Furthermore, only the two source dipoles with most highly-correlated time-courses are found, while other correlated source networks that may exist are not identified. To make the method more useful, Brookes et al. suggest using *a priori* information to fix the position of one of the two beams; however, this solution limits the method's application to well-understood neurobehavioral networks or requires information from other functional neuroimaging techniques (e.g., fMRI).

In the present study, we propose a new formulation of the beamformer technique that addresses many previous limitations of beamformer approaches. By using a spatial filter that contains the lead-fields of two simultaneous dipole sources (i.e., rather than the linear combination of the two as for the approach by Brookes and colleagues), our vector Dual-Core Beamformer (DCBF) can directly compute and obtain optimal source orientations and weights between two highly-correlated sources. In effect, this renders non-linear optimization and non-linear searching for optimal orientations and weighting unnecessary, thereby reducing the computational time of the dual beamformer method and making it a much more useful MEG inverse-modeling technique. At the same time, the DCBF retains many desirable characteristics of the dual-beamformer approach proposed by Brookes et al. For example, our computer simulations demonstrate that DCBF successfully localizes dipole sources at very low SNR (SNR of 0.25), which is useful for many MEG recordings.

In the present approach, we use a modified Powell search to find the optimal pseudo-Z-score, which not only greatly reduces the computational time required for source localization, but also identifies other local maxima. All maxima, consisting of two sources each, are defined as pathways. With simulations, we show how such a search can find multiple pairs of correlated sources present in a single MEG data set. In a median-nerve stimulation

experiment, we present how these pathways may be meaningful and are not simply a byproduct of DCBF.

2.3 Materials and Methods

2.3.1 New Dual-Core Beamformer Approach (DCBF)

A major limitation of the dual-beamformer method proposed by Brookes and colleagues is the necessity to optimize the orientation of both beams and their relative weighting. Their approach requires non-linear optimizations which increase the computational complexity of the dual beamformer approach many-fold when compared to the single beamformer approach. In the present study, we show that the optimal orientations and weighting of both beams can be directly computed, instead of searched, by using a vector formulation of the dual beamformer approach. First, we start with lead-field vector for each dipole as an *m x 3* matrix expressed in a pre-defined coordinate basis with three axes. Alternatively, since MEG is insensitive to radially-directed currents, the lead-field vector for each dipole can be decomposed by singular value decomposition (SVD) and expressed instead as an *m x 2* matrix to reduce the inverse problem to two spatial dimensions (Huang et al., 2006). Then, we define the combined lead-field vectors from both dipoles in the dual beamformer as an *m x 4* matrix, instead of a linear combination of two lead-fields:

$$\boldsymbol{L}_d = [\boldsymbol{L}_1\ \boldsymbol{L}_2] \tag{2.1}$$

The new $\boldsymbol{L}_d$ is therefore a spatial filter with two cores rather than one. Such a description of the spatial filter allows eigenvalue analysis to analytically determine optimal orientations of each beam and optimal weighting between each beam. Similar to the pseudo-Z-statistic computation for the single vector beamformer in Section 1.7, we define the *4 x 4* matrix $\boldsymbol{K}_d$:

$$\boldsymbol{K}_d = (\boldsymbol{L}_d^T \cdot \boldsymbol{R}_b^{-1} \cdot \boldsymbol{L}_d)^{-1} \cdot (\boldsymbol{L}_d^T \cdot (\boldsymbol{R}_b^{-1} \cdot \boldsymbol{R}_n \cdot \boldsymbol{R}_b^{-1}) \cdot \boldsymbol{L}_d) \tag{2.2}$$

By diagonalizing $\boldsymbol{K}_d$ with eigenvalue decomposition and inverting the smallest eigenvalue, we obtain the best possible pseudo-Z-score for the two dipoles.

$$Z_{opt}^d = \left(min\left(eig(\boldsymbol{K}_d)\right)\right)^{-1} \tag{2.3}$$

This step is an extension of the approach used in the single beamformer in Equation 1.35 (Sekihara et al., 2004). We can also define a matrix analogous to $\boldsymbol{Q}$ for the single beamformer in Section 1.7 to estimate the source powers and orientations:

$$\boldsymbol{Q}_d = \boldsymbol{L}_d^T \cdot \boldsymbol{R}_b^{-1} \cdot \boldsymbol{L}_d \tag{2.4}$$

By diagonalizing $\boldsymbol{Q}_d$ with eigenvalue decomposition, we can obtain the optimum beamformer power, the optimum orientations, and the optimum weighting of the two source dipoles as follows (Sekihara et al., 2004):

$$P_{opt}^d = \left(min\left(eig(\boldsymbol{Q}_d)\right)\right)^{-1} \tag{2.5}$$

$$\begin{pmatrix} \boldsymbol{\eta}_1 \\ \boldsymbol{\eta}_2 \end{pmatrix} = \overline{\boldsymbol{v}}_{min} \tag{2.6}$$

$\overline{\boldsymbol{v}}_{min}$ is defined as the four-component eigenvector associated with the minimum eigenvalue of $\boldsymbol{Q}_d$. The first two elements of $\overline{\boldsymbol{v}}_{min}$ contain the optimal beam 1 weighting in the two different basis directions. The last two elements contain the optimal beam 2 weighting in its basis directions. The elements corresponding to beam 1 $(\boldsymbol{\eta}_1)$ and the elements corresponding to beam 2 $(\boldsymbol{\eta}_2)$ are scaled such that relative weighting between the beams is optimal. The cost of computation is low because the eigenvalue decompositions are performed on matrices ($\boldsymbol{K}_d$ and $\boldsymbol{Q}_d$) with low dimensions (4 by 4). Since the DCBF is a vector formulation of the previous dual beamformer method (Brookes et al., 2007), reconstructed dipole orientations and weighting should be the same for both methods. To examine the computational efficiency (speed) resulting from directly computing orientations and weights instead of performing a non-linear search, 100 direct computations and 100 Nelder-Mead non-linear simplex searches were performed and timed.

The reconstructed time-course for the source dipoles is given by:

$$\hat{\boldsymbol{s}}(t) = \overline{\boldsymbol{v}}_{\boldsymbol{min}} \cdot \left(P_{opt}^{d} \cdot \boldsymbol{R}_b^{-1} \cdot \boldsymbol{L}_d \cdot \overline{\boldsymbol{v}}_{\boldsymbol{min}}\right)^T \cdot \boldsymbol{b}(t) \tag{2.7}$$

$\hat{\boldsymbol{s}}(t)$, the source time-courses, is a *4 x t* matrix whose first two rows comprise the time-course for the first source and whose last two rows comprise the time-course for the second source. Each row contains the component of the

time-course along each axis. An assumption of signal reconstruction is that both signals are highly correlated. As a result, only one time-course is actually reconstructed. However, this time-course is weighted appropriately to generate a time-course for each component of each source.

Since the optimal weighting, orientations, and pseudo-Z-statistic are computed directly, the only parameter left to optimize is the specific combination of dipoles that leads to the maximum pseudo-Z-score. As noted before, this can be accomplished by an exhaustive brute-force search over all possible dipole combinations (Brookes et al., 2007). In this scenario, if p is the number of dipoles, one would have to compute $p(p+1)/2$ pseudo-Z-scores to find the best dipole combination. To circumvent the long computational time of a brute-force search, *a priori* information can be used to fix the location of one dipole (Brookes et al., 2007). However, this method is not ideal when knowledge of sources is not widely accepted or is unavailable.

In the present study, a modified Powell search algorithm was implemented to find the best dipole combination without performing a brute-force calculation and without requiring *a priori* information. Let $[r_1, r_2]$ be the two coordinate axes on which the search is performed. The r_1 axis corresponds to the index of the first dipole in a given source grid, while r_2 corresponds to the index of the second dipole. Let the function that we are searching over be defined as:

$$f(r_1, r_2) = Z_{opt}^{d}(r_1, r_2) \tag{2.8}$$

Suppose r_1^0 is a dipole picked randomly from a given source grid. The profile $f(r_1^0, r_2)$ is calculated and then maximized to find the corresponding r_2^{opt} value. Subsequently, the profile $f\left(r_1, r_2^{opt}\right)$ is calculated to find an optimized r_1 value. This process is repeated until stable Z_{opt}^{d}, r_1^{opt}, and r_2^{opt} are reached. Since this search may converge to a local maximum, the process may be iterated multiple times using random initializations of dipoles. In this manner, r_1^{opt} and r_2^{opt}, or the optimal dipole combination can be reached more quickly than the brute-force method. In our reconstructions, the Powell search was also implemented with a taboo list to reduce computational time by interrupting the search every time a dipole combination that had already been traversed was selected again.

The results of all Powell search iterations (pairs of correlated sources) were saved as they are local maxima of Z_{opt}^{dual}. These local maxima, or pathways of cortical activation, represent different highly-correlated networks that co-exist in the data.

2.3.2 Setup for Computer Simulations

Computer simulations were performed in order to examine the performance of both the dual-core spatial filter and the non-linear modified Powell search portions of the DCBF. The simulator was programmed to test

up to three pairs of source dipoles under differing conditions of frequency, cross-correlation, and amplitude. The base signal for each dipole was programmed to be a simple sinusoidal wave in a specific direction. In addition, the noise simulation was programmed so that the SNR of each simulation could be chosen manually by adding uncorrelated random noise. The searchable source space was simulated with a fixed-source grid based on the gray-matter boundary obtained from a healthy subject's T1-weighted MRI using Freesurfer (Dale et al., 1999; Fischl et al., 2004) and a grid spacing of 7 mm. The boundary element method (BEM) was used for the MEG forward model calculation with the BEM mesh (5 mm mesh size) being the inner-skull surface from the MRI. In each case, SVD was used to reduce the lead-field vectors to *m x 2* matrices (Huang et al, 2006). In each simulation, the search was given 1000 random re-starts. Performance was evaluated by average time to find the correct solution or equivalently, the number of searches required on average to find the solution.

To evaluate the performance of our reconstruction under differing levels of noise, simulations were performed with the following control conditions: 1 pair of sources, 30 Hz frequency, 100% intra-pair correlation, and 1:1 amplitude ratio for the two source dipoles. Reconstruction was evaluated at SNRs of 4.0, 3.0, 2.0, 1.0, 0.50, 0.33, and 0.25. In our simulations, we defined SNR in sensor domain as the total power of the signal divided by the total power of the noise that was added to the signal. To examine the effects of

source signals containing more than one frequency component, the 0.25 SNR test condition was repeated for 1 pair of 100% correlated sources with a dominant 30 Hz component and a half-amplitude 20 Hz component. The 0.25 SNR test condition was also repeated to test DCBF performance in the presence of correlated noise at 10 Hz. Correlated noise was introduced by means of a single noise source of same amplitude oscillating at a frequency of 10 Hz throughout the entire simulation.

To evaluate the performance of our reconstruction under differing correlations within the source pair, simulations were performed with the control conditions: 1 pair of sources, 30 Hz frequency, 1:1 source amplitude ratio, and SNR of 2.0. The following intra-pair correlations were simulated as the variable condition: 86.6%, 75%, and 50%. To evaluate the performance of our reconstruction under differing source amplitudes, simulations were performed with the control conditions: 1 pair of sources, 30 Hz frequency, 100% intra-pair correlation, and SNR of 2.0. The following amplitude ratios were simulated as the variable condition: 1:1, 2:1, and 3:1. To evaluate the performance of our reconstruction in a more realistic scenario and for multiple dipoles, three source-pairs were selected with frequencies of 20 Hz, 30 Hz, and 40 Hz. Each source dipole had differing amplitudes. Each pair of dipoles was programmed with slightly different intra-pair correlations. The dipoles were also uncorrelated across pairs. The SNR was set to 0.6075.

To evaluate the performance of our reconstruction in the presence of three correlated sources, three sources were given a sinusoidal signal with a frequency of 30 Hz at a SNR of 0.25. The second and third sources were phase-shifted 22.5 degrees and 45 degrees from the first source. Activation maps were generated for the pathway with highest pseudo-Z-score from the formula:

$$Z_{comb} = \frac{max(Z_1) \cdot [Z_1 - min(Z_1)]}{max(Z_1) - min(Z_1)} + \frac{max(Z_2) \cdot [Z_2 - min(Z_2)]}{max(Z_2) - min(Z_2)} \qquad (2.9)$$

Z_1contains the pair-wise pseudo-Z-scores for the first optimal dipole with all other dipole sources. Z_2 contains the pair-wise pseudo-Z-scores for the second optimal dipole with all other dipole sources. Monte Carlo simulations were used to obtain a distribution of pseudo-Z-scores produced by noise. A kernel-smoothed density-estimate was computed to produce a continuous distribution. Statistical significance of pseudo-Z-scores for all activation maps was determined by integration of the continuous distribution.

2.3.3 Setup for Auditory Steady-State MEG Response

An auditory stimulus experiment was designed to test DCBF reconstruction of correlated sources in an actual MEG measurement. The experiment consisted of 200 epochs of evoked responses to a stereo test file. The test file consisted of an 1800 ms pre-stimulus noise measurement period and a 2000 ms post-stimulus period. The stimulus was a 500 Hz pure tone

with a 40 Hz envelope modulated at 100% level. The intensity of the stimulus was balanced between left and right ears. The start and end of the stimulus were smoothed with a cosine roll-off to prevent any artifacts from the stimulus. Magnetic fields evoked by auditory stimulation were measured using an Elekta/Neuromag^{TM} whole-head MEG system (VectorView) with 204 gradiometers and 102 magnetometers in a magnetically shielded room (IMEDCO-AG, Switzerland). EOG electrodes were used to detect eye blinks and eye movements. An interval of 1900 ms post-stimulus data was recorded, using 1500 ms of pre-stimulus data for noise measurement. Data were sampled at 1000 Hz and run through MaxFilter to remove environment noise (Taulu et al., 2004; Taulu and Simola, 2006; Song et al., 2008; Song et al., 2009). 188 artifact-free MEG responses were averaged with respect to the stimulus trigger. A BEM mesh of 5-mm mesh size for the subject was generated from the inner-skull surface using a set of T1 MRI images taken on a 1.5 T GE scanner. A fixed source grid with 7-mm spacing was generated from the gray-white matter boundary of the T1 image by Freesurfer. Lead-field vectors for each dipole source were reduced to *m x 2* matrices by ignoring the weakest orientation (Huang et al., 2006), reducing all reconstructed time-courses to two components. Registration of MRI and MEG was performed using data obtained from the Isotrack system prior to subject scanning in the MEG machine. The signal (gradiometers only) was then reconstructed using the dual-core beamformer approach coupled to the non-linear modified Powell

search. Activation maps were generated in the same fashion as in Equation 2.9. Source time-courses were low-pass filtered under 50 Hz to display the auditory response. Time-frequency (TF) analysis of the source time-courses with Morelet wavelets (5 cycle width) was performed between 1 and 50 Hz to identify transient and steady-state auditory responses.

2.3.4 Setup for Right Median Nerve Stimulation MEG Response

The performance of the DCBF was further examined using human MEG responses to right median nerve stimulation. This task is widely used to study the somatosensory system and provides a useful standard for analyzing DCBF performance since the location of activated dipole sources is easily predictable. We conducted MEG recordings for this experiment on 6 healthy subjects (men, ages 20-42) as they underwent right median-nerve stimulation. All subjects signed the consent forms approved by the Institutional Review Board of the University of California at San Diego. Each subject's median nerve was stimulated using a bipolar Grass™ constant-current stimulator. The stimuli were square-wave electric pulses of 0.2 ms duration delivered at a frequency of 1 Hz. The inter-stimulus-interval (ISI) was between 800 and 1200 ms. The intensity of the stimulation was adjusted until robust thumb twitches were observed. A trigger was designed to simultaneously send a signal to the MEG for every stimulus delivery to allow averaging over evoked trials. Magnetic fields evoked by median nerve stimulation were measured using the Elekta/Neuromag™ whole-head MEG system. EOG electrodes

were used to detect eye blinks and eye movements. An interval of 500 ms post-stimulus was recorded, using 300 ms of pre-stimulus data for noise measurement. Data were sampled at 1000 Hz and run through a high-pass filter with a 0.1 Hz cut-off and through MaxFilter to remove environmental noise (Taulu et al., 2004; Taulu and Simola, 2006; Song et al., 2008; Song et al., 2009). A minimum of 150 artifact-free MEG responses (gradiometers only) per subject were averaged with respect to the stimulus trigger. BEM mesh generation, source grid generation, MRI-MEG registration, and source time-course reconstruction were carried out in the same manner as in the auditory steady-state MEG response experiment. Activation maps were generated in the same fashion as in Equation 2.9.

2.4 Results

2.4.1 Computer Simulations

2.4.1.1 Computational Time for Obtaining the Optimal Dipole Orientations and Weights

To examine the difference in computational costs between the non-linear search approach from Brookes and colleagues and our analytical approach, we performed 100 Nelder-Mead non-linear simplex searches and 100 eigenvalue decompositions to obtain the optimal dipole orientations and optimal dipole weighting for two simulated dipoles. Non-linear searching and eigenvalue decomposition both resulted in accurate reconstruction of orientations and weighting with less than 1% difference. The average times for reconstruction were $0.0142\ s$ and $1.4 \cdot 10^{-4}\ s$ for the simplex search and the eigenvalue decomposition, respectively, resulting in a speed up of 100 times using our approach. Performing the exhausted analysis for all combinations of two-dipole pairs in a 5000 dipole-grid would take approximately 50 hours using the non-linear search approach from Brookes and colleagues. In contrast, our direct computation approach based on eigenvalue decomposition would take approximately 30 minutes. As we show later in this section, the modified Powell approach further speeds up the analysis by bypassing the exhaustive analysis of all dipole combinations.

2.4.1.2 SNR

The results from the simulations designed to test performance under varying SNR are listed in Table 2.1. In each test, the dipole-pair locations reconstructed with the highest pseudo-Z-score were identical to the dipole-pair locations that were originally programmed with the signal. Thus, even under an SNR of 0.25, the reconstruction was able to localize the sources perfectly. Under all levels of SNR, the orientations were recovered faithfully $(0.27\% < \varepsilon < 2.56\%)$. Orientation error, ε, was defined as the mean of the fractional errors of the individual dipole orientation ratios. Source amplitudes were reconstructed accurately across all levels of SNR $(6.8\% < \varepsilon < 7.2\%)$. Reconstructed amplitudes were determined by finding the intensity of the Fourier transform for the reconstructed time-course at the appropriate frequency. When source dipoles contained signals of two frequencies, the accuracy of reconstructing each frequency component's amplitude was similar to the single frequency scenario $(\varepsilon_{30} = 7.24\%,\ \varepsilon_{20} = 7.70\%)$. In the presence of correlated noise, source dipole locations were reconstructed accurately and quickly, though the amplitude error $(\varepsilon = 8.5\%)$ and orientation error $(\varepsilon = 4.29\%)$ were slightly higher. Interestingly, the average number of searches and the average time taken to find the optimum dipole pair are reduced linearly as the SNR decreases, but saturate as the SNR approaches zero $(r^2_{search} = 0.9608\ ;\ r^2_{time} = 0.9599)$.

2.4.1.3 Signal Correlation

The results from the simulations designed to test performance under varying signal correlations are displayed in Table 2.2. In each case, the dipole pair reconstructed was identical to the original source dipoles. Thus, even under a correlation of only 50%, the reconstruction was able to localize the sources perfectly. The reconstructed amplitudes in each of these simulations faithfully matched the original source amplitudes ($\bar{\varepsilon} = 12.5\%$; $\sigma_{\bar{\varepsilon}} = 5.1\%$) and became linearly more accurate as the pair correlation increased ($r^2 = 0.99905$). The reconstructed orientations also faithfully matched the original source orientations and exhibited little dependence on the correlation ($\bar{\varepsilon} = 0.40\%$; $\sigma_{\bar{\varepsilon}} = 0.18\%$). Interestingly, the proper dipole pair was found more immediately, repeatedly, and quickly for non-perfectly correlated than perfectly-correlated sources. For each non-perfectly correlated simulation, decreasing the original source correlation led to a concomitant linear decrease in the pseudo-Z-score ($r^2 = 0.99998$).

2.4.1.4 Source Amplitude Ratio

The results from the simulations designed to test performance under varying amplitude ratios within a pair of dipoles are shown in Table 2.3. The reconstructed amplitude ratios in each simulation closely reflect the original source amplitude ratio ($1.97\% < \varepsilon < 4.48\%$). In the reconstruction, the orientations faithfully represent the original source orientations ($0.34\% < \varepsilon <$

1.63%). As one increases the relative amplitude ratios within each pair of dipoles from 1 to 2 to 3, the number of searches and the time required to find the dipole pair decrease linearly ($r^2_{search} = 0.908$; $r^2_{time} = 0.905$). The amplitude ratio did not affect the computed pseudo-Z-scores.

2.4.1.5 Three Pairs of Dipoles

The results for the six dipole (3 source-pair) simulation are presented in Table 2.4. All six sources were reconstructed in an average of 4.8 minutes and 143 searches. Increasing the number of correlated two-source networks in the simulation did not result in an unmanageable increase in computational time. Even with the low SNR (0.6075), differing intra-pair correlations, and differing amplitudes both inside and outside of each dipole pair, all of the dipoles were reconstructed to the proper spatial position. The three inter-pair correlations in this study were all zero. Furthermore, the twelve reconstructed amplitudes closely represented the original source amplitudes ($\bar{\varepsilon} = 11.32\%$; $\sigma_{\bar{\varepsilon}} = 5.67\%$). Reconstruction of each source's orientation was reasonably accurate ($\bar{\varepsilon} = 3.16\%$; $\sigma_{\bar{\varepsilon}} = 2.22\%$).

2.4.1.6 A Third Correlated Source

Two of the three sources in the simulation were reconstructed accurately in an average of 1.03 searches and 0.04 minutes. As expected, the amplitudes of the reconstructed sources were suppressed by 47.29% due to the third correlated source. Figure 2.1 shows the activation map of the three

reconstructed sources, which was derived by combining the dipole pseudo-Z-scores. Red values were thresholded at $P < 0.05$, and yellow values were thresholded at $P < 10^{-5}$. The combined pseudo-Z-score for all three dipoles was significant ($P < 10^{-5}$).

2.4.2 Applying DCBF to Human Auditory MEG Responses

MEG data were obtained for the 500 Hz tone auditory stimulus tests (Brookes et al., 2007). All data were subsequently processed with MaxFilter (Taulu et al., 2004; Taulu and Simola, 2006; Song et al., 2008; Song et al., 2009) and the signal was reconstructed utilizing our new DCBF approach coupled with the modified Powell search restricted to inter-hemispheric searches. To enhance the SNR of the relatively weak auditory response, 188 responses were averaged. Figure 2.2 displays the pseudo-Z-scores of the local maxima, or pathways, found by the modified Powell search algorithm. After 1000 starts, the optimum pathway had a pseudo-Z-score of 1.0791 ($P < 1.3 \cdot 10^{-5}$), indicating that two highly correlated dipoles had been found. Out of the 3 identified pathways, this pathway was also found most often, taking an average of 1.1 searches or 0.0305 minutes. Figure 2.3 displays the cortical activation map derived from plotting the combined correlations of each optimal dipole with all other dipoles in the brain. For both hemispheres, red values were thresholded at $P < 0.05$, and yellow values were thresholded at $P < 0.005$. Figure 2.3 also shows that the activity is localized to Brodmann

Areas 41 and 42 (primary and association auditory cortices) in both left and right hemispheres. Pathways with low pseudo-Z-scores localized to deep sources. Figure 2.4 displays the time-courses of the transient and steady-state auditory responses. The left to right hemisphere source amplitude ratio was 1.11. Wavelet transform time-frequency (TF) analysis was performed on the reconstructed signal to identify the transient and steady-state responses. TF analysis between 4 and 12 Hz revealed a focal region of power immediately following stimulus delivery, corresponding to the auditory transient response. TF analysis of the source signal in the 32-48 Hz band indicated the presence of power throughout the entire stimulus period centered at 40 Hz, corresponding to the auditory steady-state response (Herdman et al., 2003b; Ross et al., 2005; Simpson et al., 2005).

2.4.3 Applying DCBF to Human Median Nerve Stimulation MEG Responses

MEG data were obtained from six healthy subjects for the right median nerve stimulus test. Individual trials were averaged to enhance the SNR of the MEG evoked-response. All data were subsequently processed with MaxFilter (Taulu et al., 2004; Taulu and Simola, 2006; Song et al., 2008; Song et al., 2009), and spatial locations were reconstructed utilizing the DCBF approach. Figure 2.5 shows the multiple pathways found by DCBF sorted according to pseudo-Z-score or correlation for a single representative subject (Subject #1).

The plateaus in Figure 2.5 designate searches that yielded the same result multiple times, which are considered to be important pathways or networks of activation. Figure 2.6 shows activation maps computed with (17) for three of these selected networks along with similar networks reconstructed from other subjects. The activation maps were computed in the same manner as for the auditory-response analysis. All subjects had a common network of activation in the primary somatosensory cortex (S1, including Brodmann Areas 1, 2, and 3) and the secondary somatosensory cortex (S2) (Figure 2.6a). Three subjects showed common networks involving the primary somatosensory cortex (S1) and Brodmann Area 5 of the posterior parietal lobe (Figure 2.6b). Three subjects also had a common network of activation involving the primary motor cortex (M1) and parts of the somatosensory cortex (S1 or S2) (Figure 2.6c). Two subjects showed a previously observed network of activation involving the primary somatosensory cortex (S1) and the temporal-parietal junction, a poly-sensory area (Huang et al., 2006).

2.5 Discussion

In the present study, we implemented a novel and powerful dual-beamformer method that was paired with the modified-Powell search to create the DCBF. Our DCBF approach addressed various shortcomings of the earlier dual-beamformer method, the CCSM, and the NB. Instead of using a spatial filter or lead-field vector consisting of a linear combination of lead-field vectors from two dipoles, we chose to concatenate the lead-field vectors from the two dipoles together, which simultaneously covered two spatial locations at once. We were also able to perform eigenvalue decomposition and analysis of the low-dimensional $\boldsymbol{K}_d$ matrix to analytically find the optimal pseudo-Z-score of two dipoles directly, without having to search for their best orientations non-linearly. In addition, we performed eigenvalue decomposition of another low-dimensional $\boldsymbol{Q}_d$ matrix to analytically recover the most favorable weighting between dipoles and the best orientation of the dipoles that optimized the pseudo-Z-score (Sekihara et al., 2004) without the need for a time-consuming non-linear search process that takes approximately 100 times longer. Optimal source dipoles were found by our modified non-linear Powell search instead of through exhaustive brute-force search, which is about three times slower. The Powell search also enabled analysis without *a priori* information about any of the dipole positions. Thus, we were able to identify multiple highly-correlated neuronal networks that were associated with meaningful local maxima of pseudo-Z-scores.

We conducted a series of computer simulations to test the robustness and performance of the DCBF with regards to variations in several important parameters. We showed that decreased SNR leads to faster localization of the source dipoles during the modified Powell search. A Powell search has the best probability of finding peaks with broad bases. Thus, we believe that lower SNR leads to a broader peak in pseudo-Z-score, which allows the optimal dipole combination to be identified more readily. In fact, the reconstruction performed reliably even under conditions of 0.25 SNR for both single and dual frequency sources and for both uncorrelated and correlated band-limited noise. At every SNR tested, our reconstruction technique successfully located the source dipoles without error. For spontaneous recordings, the MEG signal can often have a very low SNR, especially since the data cannot be averaged. For evoked recordings, a higher SNR can be obtained from averaging. Our computer simulations show that the DCBF may be applied for both types of recordings, since the method operates over a wide range of SNR.

By varying source correlation, we found that the DCBF successfully identified sources even when their signals were only 50% correlated. In fact, non-purely correlated sources were localized much more quickly than 100% correlated sources because the pseudo-Z-score solution space is less sharply peaked around the global maximum for non-purely correlated sources than for fully correlated sources.

To test the performance of our direct computation of optimal dipole weighting, we performed computer simulations with source dipoles emitting signals at varying ratios of amplitudes. Interestingly, as we increased the disparity in amplitude between signals, the reconstruction was able to localize the source dipoles more quickly. Differing source amplitudes likely led to a broader peak in pseudo-Z-score, allowing the optimal dipole combination to be identified more readily. The primary purpose of the amplitude simulations, however, was to examine if the reconstructed signals still maintained the proper amplitude weighting. Reconstructed amplitude ratios were indeed quite close to the original source amplitude ratios, confirming that our approach to obtaining optimal weighting was successful.

To determine whether the DCBF could perform in real-world conditions, we designed one simulation with three pairs of non-purely correlated dipoles. All three pairs of correlated sources were localized accurately within an average of 5 minutes. Furthermore, the amplitude ratios and orientations were reconstructed with only minor error, demonstrating that the DCBF can accurately reconstruct multiple simultaneously-activated networks of correlation.

Another simulation was designed at low SNR to test the ability of the DCBF to reconstruct three correlated dipoles. Only two sources could be located with the Powell search, and their amplitudes were suppressed. The suppression occurred due to the underlying assumption that only two sources

are correlated. Thus, the effect was similar to suppression of the conventional single beamformer in the presence of a second correlated source. However, the generated activation map shows that the DCBF successfully localized all three correlated-source in a significant manner (Figure 2.1).

By applying our novel method to the analysis of bilateral auditory-stimulation data in humans, we showed that the DCBF could quickly (< 20 sec) and accurately reconstruct correlated sources in a real experiment. Analysis of the pathway most frequently found and with highest pseudo-Z-score revealed sources located in the primary auditory cortices, as expected. In addition, time-frequency analysis of the reconstructed signal showed both the expected 40 Hz steady-state response and the transient response.

To explore the idea of finding multiple networks, we also applied the DCBF approach in an analysis of right median-nerve stimulation data from six healthy subjects. A plot of the number of searches as a function of pseudo-Z-scores showed different local maxima that were found multiple times, indicating the presence of different pathways. We found that the most common pathway among subjects corresponded to activation in the primary somatosensory area (S1, including BA 1, 2, and 3) and the secondary somatosensory area (S2). Two other pathways identified in half of the subjects included S1 and a classic sensory-transduction area (Brodmann Area 5), and S1 or S2 and the dorsal aspect of the primary motor area (M1). The

activations in S1, S2, and M1 evoked by median-nerve stimuli are well-documented by MEG (see review in Huang et al., 2000, 2005).

2.5.1 Summary

The most important features of the DCBF approach arise from incorporating the lead-field vectors of two simultaneously-activated neuronal sources into a single spatial filter. With this novel beamformer, we were able to successfully compute optimal dipole weights, orientations, and pseudo-Z-scores, eliminating time-consuming searches that hindered the previous dual-beamformer approach. In addition, by utilizing a powerful Powell search with a taboo list, we were able to reconstruct optimal source dipoles quickly without the use of *a priori* information. The changes and optimizations we made decreased the total computing time from tens of hours (Brookes et al., 2007) to less than 15 minutes, making the DCBF a viable and useful MEG source localization method for correlated sources. Future directions include extending the DCBF framework to three or four beams to find tightly correlated and complex networks of activity. The DCBF can also be migrated from a time-domain analysis to a frequency domain or time-frequency (wavelet) domain analysis to reduce the effects of noise and phasing.

2.6 Acknowledgments

This work was supported in part by a research grant from the McDonnell Foundation (220020185) via the Brain Trauma Foundation (PI:

Jamshid Ghajar, site PIs: Lee and Huang), Merit Review Grants from the Department of Veterans Affairs to Huang (051455 and 060812), Lee (E4477-R), and Harrington (1IO1CX000146-01 and B501R), and from the NIH to Srinivasan (R01-MH068004) and to Shu Chien (5T32HL007089-34). We would also like to thank Jamshid Ghajar for his encouragement and support and Omer Tal for many helpful discussions. In addition, we would like to thank three anonymous reviewers' constructive suggestions that substantially strengthened the present study.

Chapter 2, in part, is a reprint of the material as it appears in NeuroImage 54, pp. 253-263, 2011. Diwakar, Mithun; Huang, Ming-Xiong; Srinivasan, Ramesh; Harrington; Deborah L.; Robb, Ashley; Angeles, Annemarie; Muzzatti, Laura; Pakdaman, Reza; Song, Tao; Theilmann, Rebecca J.; Lee, Roland R. The dissertation author was co-first author of this publication.

Table 2.1: DCBF Performance under varying SNR

SNR	Amplitude (nAm)				Reconstructed Amplitude (nAm)				Ori-entation Ratio		Recon Orientation Ratio		Ave # Search	Ave Time (min)	Pseudo-Z-score
	Dip 1		*Dip 2*		*Dip 1*		*Dip 2*		*Dip 1*	*Dip 2*	*Dip 1*	*Dip 2*			
4.0	10	20	10	20	9.4	18.7	9.2	18.5	0.5	0.5	0.501	0.498	31.3	1.502	11.3
3.0	10	20	10	20	9.4	18.7	9.2	18.5	0.5	0.5	0.501	0.498	28.6	1.411	11.2
2.0	10	20	10	20	9.4	18.8	9.2	18.4	0.5	0.5	0.502	0.497	21.7	1.015	11.1
1.0	10	20	10	20	9.5	18.9	9.1	18.3	0.5	0.5	0.503	0.495	14.3	0.716	10.9
0.50	10	20	10	20	9.7	19.3	8.9	18.1	0.5	0.5	0.505	0.491	5.4	0.257	10.3
0.33	10	20	10	20	9.9	19.5	8.7	17.8	0.5	0.5	0.507	0.487	2.3	0.102	9.9
0.25	10	20	10	20	10.1	19.8	8.5	17.6	0.5	0.5	0.509	0.483	1.4	0.059	9.4

Table 2.2: DCBF Performance under varying source correlation

Corr-elation	Amplitude (nAm)				Reconstructed Amplitude (nAm)				Orientation Ratio		Recon-structed Orientation Ratio		Ave # Search	Ave Time (min)	Pseudo-Z-score
	Dip 1		*Dip 2*		*Dip 1*		*Dip 2*		*Dip 1*	*Dip 2*	*Dip 1*	*Dip 2*			
100%	10	20	10	20	9.4	18.8	9.2	18.4	0.5	0.5	0.502	0.498	21.7	1.015	11.1
86.6%	10	20	10	20	9.1	18.2	8.8	17.8	0.5	0.5	0.501	0.497	1	0.034	11.3
75.0%	10	20	10	20	8.9	17.7	8.5	17.1	0.5	0.5	0.501	0.497	1	0.033	11.0
50.0%	10	20	10	20	8.3	16.5	7.8	15.7	0.5	0.5	0.501	0.497	1	0.035	10.5

Table 2.3: DCBF Performance under varying source amplitude ratio

Amp-litude Ratio	**Recon-structed Amplitude Ratio**	**Orientation Ratio**		**Reconstructed Orientation Ratio**		**Ave # Search**	**Ave Time (min)**	**Pseudo-Z-score**
		Dip 1	*Dip 2*	*Dip 1*	*Dip 2*			
1:1	0.98	0.5	0.5	0.502	0.497	21.7	1.015	11.1
2:1	1.93	0.5	0.5	0.505	0.497	6.1	0.274	11.2
3:1	2.87	0.5	0.5	0.508	0.498	1.5	0.065	11.2

Table 2.4: DCBF Performance with three source pairs

Source Index	**Corr-elation (%)**	**Freq-uency (Hz)**	**Amplitude (nAm)**		**Reconstructed Amplitude (nAm)**		**Orient-ation Ratio**	**Recon-structed Orientation Ratio**	**Ave # Search**	**Ave Time (min)**	**Pseudo-Z-score**
			Dir 1	*Dir 2*	*Dir 1*	*Dir 2*					
1	92.39	20	10	20	8.26	16.27	0.500	0.508	6.37	0.21	7.57
2	92.39	20	15	25	13.88	23.97	0.600	0.579	6.37	0.21	7.57
3	95.11	30	30	20	28.30	18.98	1.500	1.492	1.20	0.04	8.97
4	95.11	30	12	8	9.77	6.90	1.500	1.415	1.20	0.04	8.97
5	96.59	40	20	15	17.90	14.26	1.333	1.255	142.86	4.80	7.09
6	96.59	40	10	12	8.59	10.12	0.833	0.849	142.86	4.80	7.09

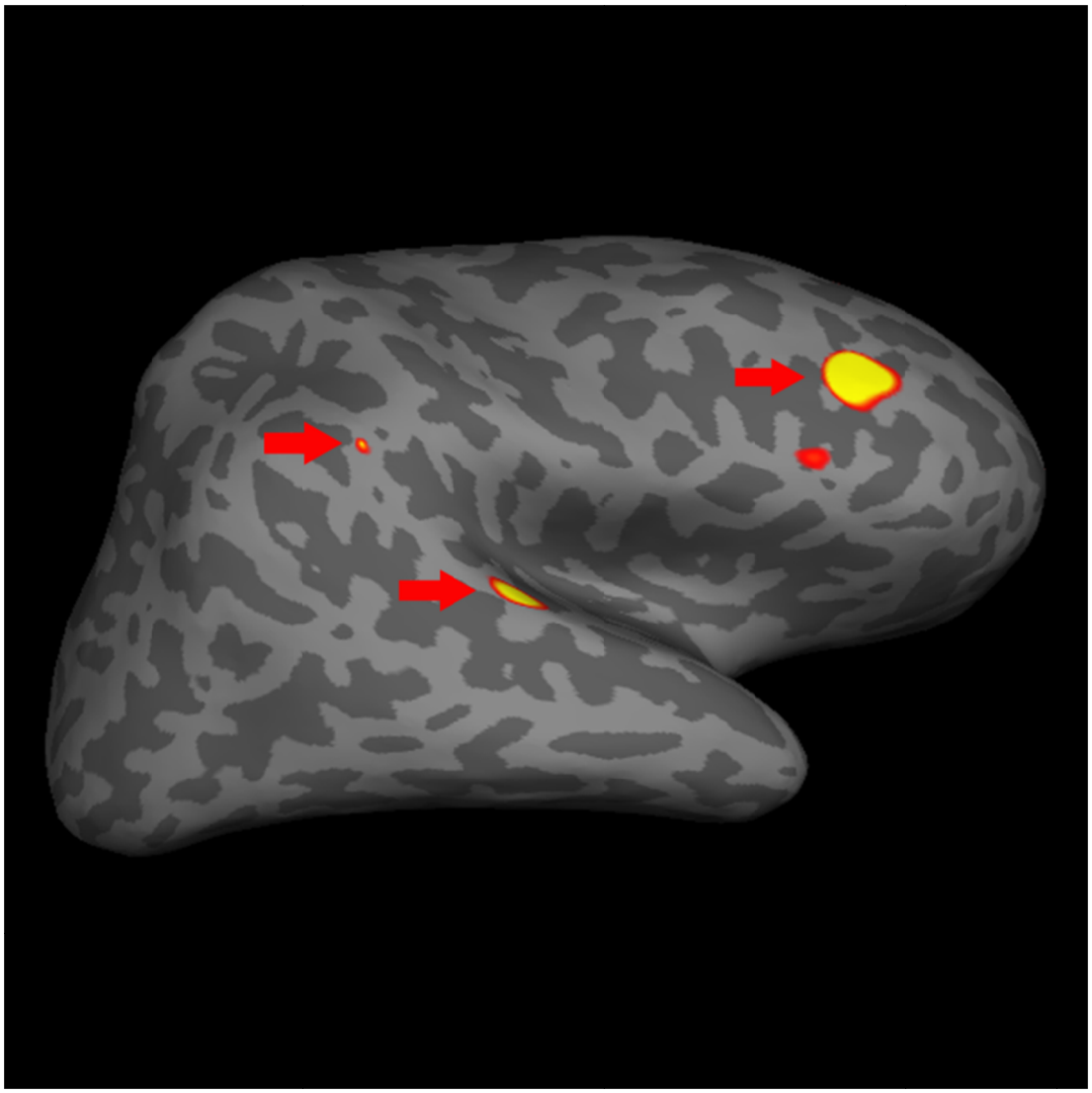

Figure 2.1: Activation Map for Three Correlated Sources. The red arrows on the activation map indicate the position of the three source dipoles. The map was thresholded such that red indicates $P < 0.05$ and yellow indicates $P < 10^{-5}$.

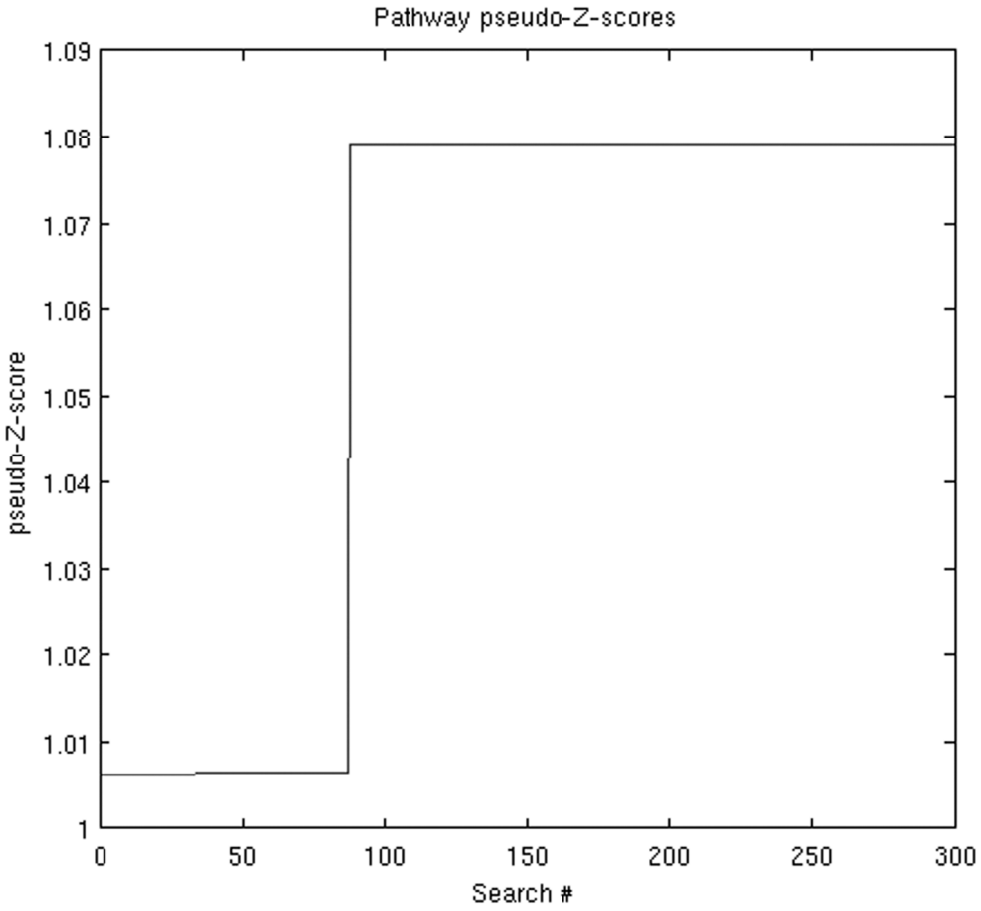

Figure 2.2: Stereo auditory stimulation in a human subject: pathways with associated pseudo-Z-scores. Plateaus in the plot denote searches that yielded the same result (local maximum) multiple times. Results that were found multiple times were considered important pathways. Only 300 out of 1000 searches are shown to emphasize the transition between pathways. The pathway with maximum correlation (pseudo-Z-score) and maximum size involved both primary auditory cortices. Its activation map is depicted in Figure 2.3.

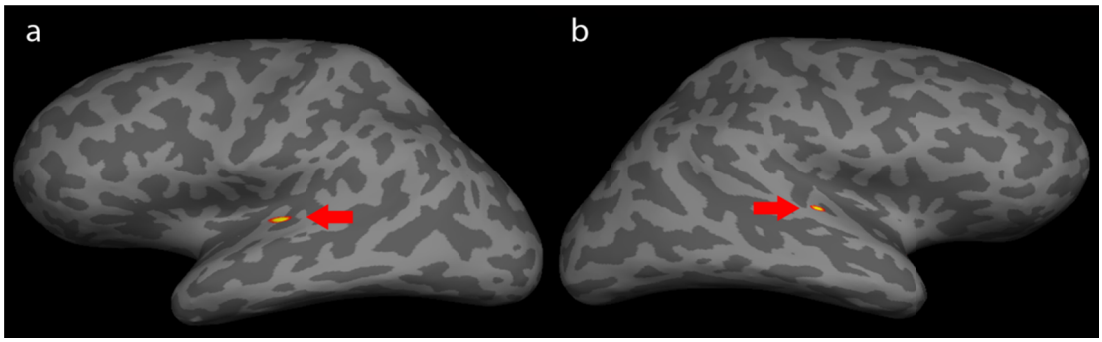

Figure 2.3: Cortical activation map during stereo auditory stimulation

a) Left hemisphere: The cortical activation map shows activation in the left primary auditory cortex.

b) Right hemisphere: The cortical activation map shows activation in the right primary auditory cortex.

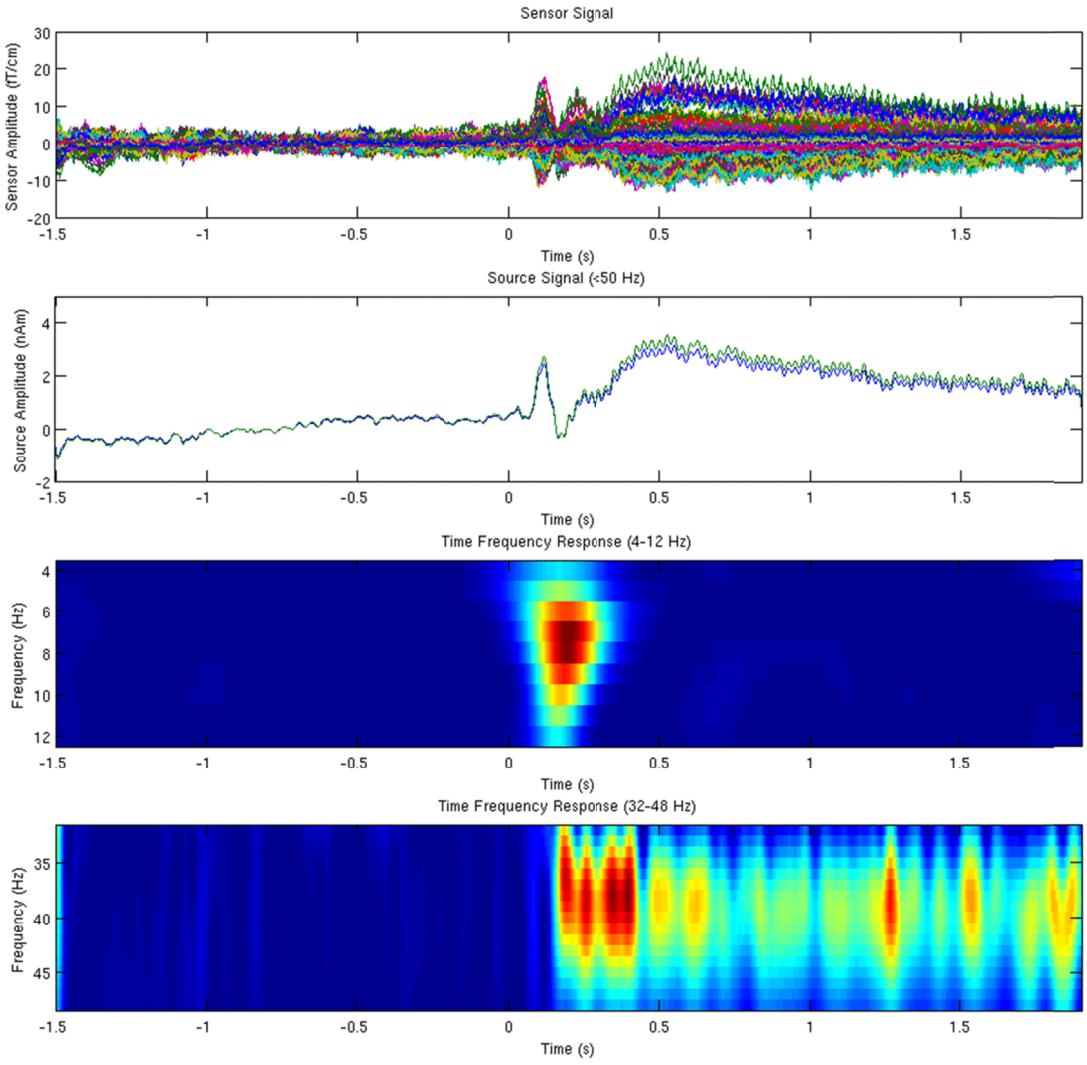

Figure 2.4: Stereo auditory-stimulation signal time-courses. The top panel shows the averaged sensor waveform for the auditory response. The second panel shows the auditory response for both right hemisphere (blue) and left hemisphere (green). The third panel shows the transient auditory-response between 4 and 12 Hz with time-frequency analysis. The fourth panel shows the steady-state auditory centered at 40 Hz with time-frequency analysis.

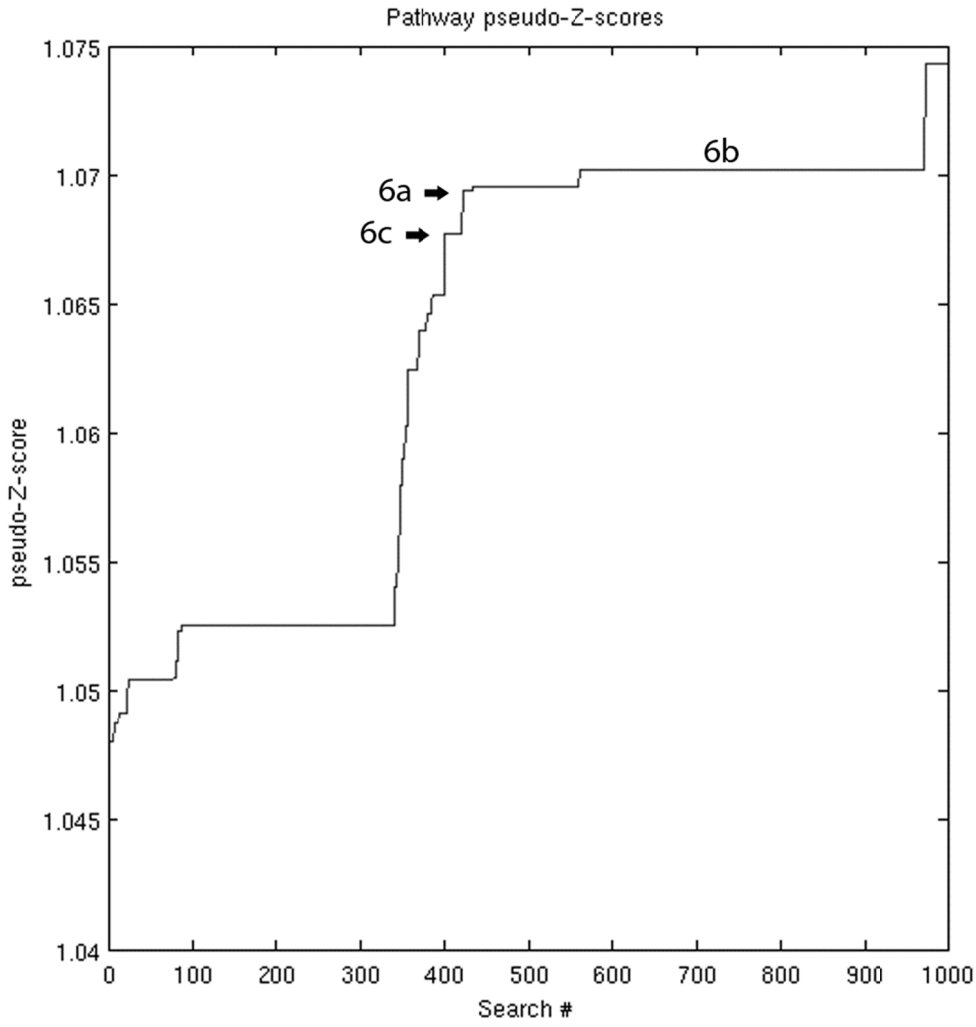

Figure 2.5: Right median-nerve stimulation for human subject #1: pathways with associated pseudo-Z-scores. Plateaus in the plot above denote searches that yielded the same result (local maximum) multiple times. Results that were found multiple times were considered important pathways. Figure 2.6 depicts the activation maps of selected pathways for subject #1 and other subjects.

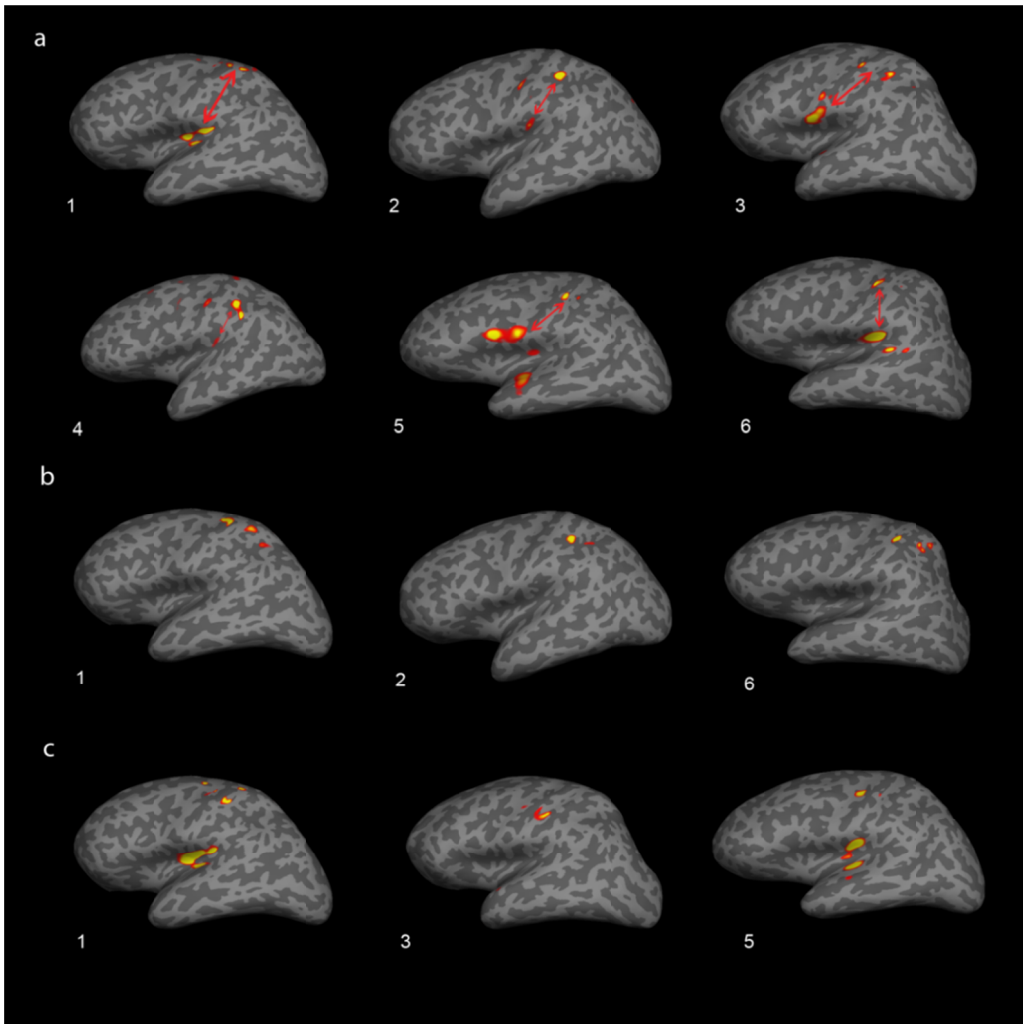

Figure 2.6: Right median-nerve stimulation activation maps for six human subjects. Pathway 6a - Activity in primary somatosensory area (S1) and secondary somatosensory area (S2) (shown with red arrows). Pathway 6b – Activity in S1 and somatosensory association cortex (Brodmann Area 5). Pathway 6c – Activity in S1 and/or S2 and the dorsal aspect of the primary motor area (M1). Red regions were thresholded at $P < 0.05$ and yellow regions were thresholded at $P < 0.001$. Subject ID numbers are shown to the bottom-left of each cortical map.

2.7 References

Aine, C., Huang, M., Stephen, J., Christner, R., 2000. Multistart algorithms for MEG empirical data analysis reliably characterize locations and time courses of multiple sources. NeuroImage 12, 159-172.

Auranen, T., Nummenmaa, A., Hamalainen, M.S., Jaaskelainen, I.P., Lampinen, J., Vehtari, A., Sams, M., 2005. Bayesian analysis of the neuromagnetic inverse problem with l(p)-norm priors. NeuroImage 26, 870-884.

Brookes, M.J., Stevenson, C.M., Barnes, G.R., Hillebrand, A., Simpson, M.I.G., Francis, S.T., Morris, P.G., 2007. Beamformer reconstruction of correlated sources using a modified source model. NeuroImage 34, 1454-1465.

Dalal, S.S., Sekihara, K., Nagarajan, S.S., 2006. Modified Beamformers for Coherent Source Region Suppression. IEEE Trans. Biomed. Eng. 53, 1357-1363.

Dale, A.M., Halgren, E., 2001. Spatiotemporal mapping of brain activity by integration of multiple imaging modalities. Curr. Opin. Neurobiol. 11, 202-208.

Dale, A.M., Fischl, B., Sereno, M.I., 1999. Cortical surface-based analysis: I. Segmentation and surface reconstruction. NeuroImage 9, 179-194.

Dale, A.M., Liu, A.K., Fischl, B.R., Buckner, R.L., Belliveau, J.W., Lewine, J.D., Halgren, E., 2000. Dynamic statistical parametric mapping: combining fMRI and MEG for high-resolution imaging of cortical activity. Neuron 26, 55-67.

Fischl, B., van der, K.A., Destrieux, C., Halgren, E., Segonne, F., Salat, D.H., Busa, E., Seidman, L.J., Goldstein, J., Kennedy, D., Caviness, V., Makris, N., Rosen, B., Dale, A.M., 2004. Automatically parcellating the human cerebral cortex. Cereb. Cortex 14, 11-22.

Hamalainen, M.S., Ilmoniemi, R.J., 1994. Interpreting magnetic fields of the brain: minimum norm estimates. Med. Biol. Eng. Comput. 32, 35-42.

Hanlon, F.M., Weisend, M.P., Huang, M., Lee, R.R., Moses, S.N., Paulson, K.M., Thoma, R.J., Miller, G.A., Canive, J.M., 2003. A non-invasive method for observing hippocampal function. NeuroReport 14, 1957-1960.

Herman, A.T., Wollbrink, A., Chau, W., Ishii, R., ross, B., Pantev, C., 2003b. Determination of activation areas in the human auditory cortex by

means of synthetic aperture magnetometry. NeuroImage 20 (2), 995-1005.

Huang, M., Aine, C., Davis, L., Butman, J., Christner, R., Weisend, M., Stephen, J., Meyer, J., Silveri, J., Herman, M., Lee, R.R., 2000. Source on Anterior and Posterior Banks of the Central Sulcus Identified from Magnetic Somatosensory Evoked Responses using Multi-start Spatio-Temporal Localization. Human Brain Mapping. 11(2), 59-76.

Huang, M., Aine, C.J., Supek, S., Best, E., Ranken, D., Flynn, E.R., 1998. Multistart downhill simplex method for spatio-temporal source localization in magnetoencephalography. Electroencephalogr. Clin. Neurophysiol. 108, 32-44.

Huang, M., Dale, A.M., Song, T., Halgren, E., Harrington, D.L., Podgorny, I., Canive, J.M., Lewis, S., Lee, R.R., 2006. Vector-based spatial-temporal minimum L1-norm solution for MEG. NeuroImage 31, 1025-1037.

Huang, M., Davis, L.E., Aine, C., Wisend, M., Harrington, D., Christner R., Stephen, J., Edgar, J.C., Herman, M., Meyer, J., Paulson, K., Martin K., Lee, R.R., 2004a. MEG response to median nerve stimulation correlates with recovery of sensory and motor function after stroke. Clin. Neurophysiol. 115, 820-833.

Huang, M.X., Aine, C., Davis, L., Butman, J., Christner, R., Weisend, M., Stephen, J., Meyer, J., Silveri, J., Herman, M., Lee, R.R., 2000. Sources on the anterior and posterior banks of the central sulcus identified from magnetic somatosensory evoked responses using multistart spatio-temporal localization. Hum. Brain Mapp. 11, 59-76.

Huang, M.X., Harrington, D.L., Paulson, K.M., Weisend, M.P., Lee, R.R., 2004b. Temporal dynamics of ipsilateral and contralateral motor activity during voluntary finger movement. Hum. Brain Mapp. 23, 26-39.

Huang, M.X., Lee, R.R., Gaa, K.M., Song, T., Harrington, D.L., Loh, C., Theilmann, R.J., Edgar, J.C., Miller, G.A., Canive, J.M., Granholm, E., 2010. Somatosensory System Deficits in Schizophrenia Revealed by MEG during a Median-Nerve Oddball Task. Brain Topography 23 (1), 82-104.

Huang, M.X., Lee, R.R., Miller, G.A., Thoma, R.J., Hanlon, F.M., Paulson, K.M., Martin, K., Harrington, D.L., Weisend, M.P., Edgar, J.C., Canive, J.M., 2005. A parietal-frontal network studied by somatosensory oddball MEG responses, and its cross-modal consistency. NeuroImage 28, 99-114.

Hui, H.B., Leahy, R.M., 2006. Linearly constrained MEG beamformers for MVAR modeling of cortical interactions. 3rd IEEE International Symposium on Biomedical Imaging: Nano to Macro, 2006, pp. 237–240.

Hui, H.B., Pantazis, D., Bressler, S.L., Leahy, R.M., 2010. Identifying true cortical interactions in MEG using the nulling beamformer. NeuroImage 49, 3161-3174.

Kim, S., Lee, C., Kang, H., 2006. Optimum beamformer in correlated source environments. J. Acoust. Soc. Am. 120 (6), 3770-3781.

Liljestrom, M., Kujala, J., Jensen, O., Salmelin, R., 2005. Neuromagnetic localization of rhythmic activity in the human brain: a comparison of three methods. NeuroImage 25, 734-745.

Marinkovic, K., Dhond, R.P., Dale, A.M., Glessner, M., Carr, V., Halgren, E., 2003. Spatiotemporal dynamics of modality-specific and supra-modal word processing. Neuron 38, 487-497.

Mosher, J.C., Baillet, S., Leahy, R.M., 1999. EEG source localization and imaging using multiple signal classification approaches. J. Clin. Neurophsiol. 16, 255-238.

Mosher, J.C., Leahy, R.M., 1998. Recursive MUSIC: a framework for EEG and MEG source localization. IEEE Trans. Biomed. Eng. 45, 1342-1354.

Mosher, J.C., Lewis, P.S., Leahy, R.M., 1992. Multiple dipole modeling and localization from spatio-temporal MEG data. IEEE Trans. Biomed. Eng. 39, 541-557.

Nguyen, T., Ding, Z., 1997. CMA beamforming for multipath correlated sources. IEEE International Conference on Acoustics, Speech, and Signal Processing 3, 2521-2524.

Osipova, D., Ahveninen, J., Jensen, O., Ylikoski, A., Pekkonen, E., 2005. Altered generation of spontaneous oscillations in Alzheimer's disease. NeuroImage 27, 835-841.

Pulvermuller, F., Shtyrov, Y., Ilmoniemi, R., 2003. Spatiotemporal dynamics of neural language processing: an MEG study using minimum-norm current estimates. NeuroImage 20, 1020-1025.

Quuran, M.A., Cheyne, D., 2010. Reconstruction of correlated brain activity with adaptive spatial filters in MEG. NeuroImage 49, 2387-2400.

Robinson, S., Vrba, J., 1998. Functional neuroimaging by synthetic aperture magnetometry. In: Yoshimoto, T., Kotani, M., Kuriki, S., Karibe, H., Nakasato, N. (Eds.), Recent Advances in Biomagnetism. Tohoku Univ. Press, Sendai, pp. 302-305.

Ross, B., Herdman, A.T., Pantev, C., 2005. Right hemispheric laterality of human 40 Hz auditory steady-state responses. Cereb. Cortex 15 (12), 2029-2039.

Sekihara, K., Nagarajan, S., Poeppel, D., Marantz, A., 2002. Performance of an MEG adaptive-beamformer technique in the presence of correlated neural activities: effects on signal intensity and time course estimates. IEEE Trans. Biomed. Eng. 49 (12), 1534-1546.

Sekihara, K., Nagarajan, S., Poeppel, D., Marantz, A., 2004. Asymptotic SNR of scalar and vector minimum-variance beamformers for neuromagnetic source reconstruction. IEEE Trans. Biomed. Eng. 51 (10), 1726-1733.

Sekihara, K., Nagarajan, S., Poeppel, D., Marantz, A., Miyashita, Y.M., 2002b. Application of an MEG eigenspace beamformer to reconstructing spatio-temporal activities of neural sources. Hum. Brain Mapp. 15, 199-215.

Shih, J.J., Weisend, M.P., Davis, J.T., Huang, M., 2000. Magnetoencephalographic characterization of sleep spindles in humans. J. Clin. Neurophysiol. 17, 224-231.

Simpson, M.I.G., Hadjipapas, A., Barnes, G.R., Furlong, P.L., Witton, C., 2005. Imaging the dynamics of the auditory steady-state evoked response. Neurosci. Lett. 16 (3), 195-197.

Song, T., Cui, L., Gaa, K., Feffer, L., Taulu, S., Lee, R.R., Huang, M.X., 2009. Signal Space Separation Algorithm and Its Application on Suppressing Artifacts Caused by Vagus Nerve Stimulation for Magnetoencephalography Recordings. J. Clin. Neurophysiol. 26 (6), 392-400.

Song, T., Gaa, K., Cui, L., Feffer, L., Lee, R.R., Huang, M.X., 2008. Evaluation of signal space separation via simulation. Med. Biol. Eng. Comput. 46, 923-932.

Stenbacka, L., Vanni, S., Uutela, K., Hari, R., 2002. Comparison of minimum current estimate and dipole modeling in the analysis of simulated activity in the human visual cortices. NeuroImage 16, 936-943.

Stephen, J.M., Aine, C.J., Christner, R.F., Ranken, D., Huang, M., Best, E., 2002. Central versus peripheral visual field stimulation results in timing

differences in dorsal stream sources as measured with MEG. Vision Res. 42, 3059-3074.

Stephen, J.M., Davis, L.E., Aine, C.J., Ranken, D., Herman, M., Hudson, D., Huang, M., Poole, J., 2003. Investigation of the normal proximal somatomotor system using magnetoencephalography. Clin. Neurophysiol. 114, 1781-1792.

Taulu, S., Kajola, M., Simola, J., 2004. Suppression of interference and artifacts by the signal space separation method. Brain Topogr. 16, 269-275.

Taulu, S., Simola, J., 2006. Spatiotemporal signal space separation method for rejecting nearby interference in MEG measurements. Phys. Med. Biol. 51, 1759-1768.

Tesche, C., 2000. Evidence for somatosensory evoked responses in human temporal lobe. NeuroReport 11, 2655-2658.

Uutela, K., Hamalainen, M., Somersalo, E., 1999. Visualization of magnetoencephalographic data using minimum current estimates. NeuroImage 10, 173-180.

Van Drongelen, W., Yuchtman, M., Van Veen, B.D., Van Huffelen, A.C., 1996. A spatial filtering technique to detect and localize multiple sources in the brain. Brain Topogr. 9 (1), 39-49.

Van Veen, B.D., Van Drognelen, W., Yuchtman, M., Suzuku, A., 1997. Localisation of brain electrical activity via linearly constrained minimum variance spatial filtering. IEEE Trans. Biomed. Eng. 44 (9).

Vanni, S., Uutela, K., 2000. Foveal attention modulates responses to peripheral stimuli. J. Neurophysiol. 83, 2443-2452.

CHAPTER 3

Accurate Reconstruction of Temporal Correlation for Neuronal Sources using the Enhanced Dual-core MEG Beamformer

3.1 Abstract

Beamformer spatial filters are commonly used to explore the active neuronal sources underlying magnetoencephalography (MEG) recordings at low signal-to-noise ratio (SNR). Conventional beamformer techniques are successful in localizing uncorrelated neuronal sources under poor SNR conditions. However, the spatial and temporal features from conventional beamformer reconstructions suffer when sources are correlated, which is a common and important property of real neuronal networks. Dual-beamformer techniques, originally developed by Brookes and colleagues to deal with this limitation, successfully localize highly-correlated sources and determine their orientations and weightings, but their performance degrades at low correlations. They also lack the capability to produce individual time-courses and therefore cannot quantify source correlation. In this chapter, we present an enhanced formulation of our earlier *dual-core beamformer* (DCBF) approach that reconstructs individual source time-courses and their correlations. Through computer simulations, we show that the enhanced DCBF (eDCBF) consistently and accurately models dual-source activity regardless of the correlation strength. Simulations also show that a multi-core

extension of eDCBF effectively handles the presence of additional correlated sources. In a human auditory task, we further demonstrate that eDCBF accurately reconstructs left and right auditory temporal responses and their correlations. Spatial resolution and source-localization strategies corresponding to different measures within the eDCBF framework are also discussed. In summary, eDCBF accurately reconstructs source spatio-temporal behavior, providing a means for characterizing complex neuronal networks and their communication.

3.2 Introduction

Our recently developed *dual-core beamformer* (DCBF) addresses many of the limitations of the *dual-source beamformer* (DSBF) developed by Brookes and colleagues (Diwakar et al., 2011). The DCBF implements the DSBF with a vector description, eliminating the need for non-linear searches of source orientations and source weighting. Furthermore, pairing the DCBF with a Powell search optimization algorithm allows quick localization of the correlated source pairs. However, our simulations demonstrated that the estimation of source amplitudes with DCBF grows inaccurate as correlation values decrease since time-course reconstruction only generates a single signal (scaled accordingly for each source). Though DCBF provides an effective way to identify source pairs, the measurement statistic (pseudo-Z-score) obtained is dependent on both source power and source correlation and does not exclusively quantify correlation between sources.

Ideally, in addition to localizing active sources, a quantitative measure of correlation is desired to obtain a more complete understanding of neuronal networks. Such a measure (e.g. power correlation) would more completely characterize highly sophisticated networks. In this chapter, we propose an *enhanced dual-core beamformer* (eDCBF), which is capable of accurately estimating the source covariance matrix from multiple sources, providing a proper measure of correlation in addition to individual source time-courses without amplitude suppression. Once sources are localized, their correlation can be found *without time-course reconstruction*, allowing the eDCBF to handle large datasets quickly and requiring little memory. If desired, the eDCBF also provides a simple way of computing correlations in frequency bands of interest. Moreover, eDCBF's improved design offers robustness to a wide range of both source correlations and SNR. Finally, the eDCBF framework may be generalized to effectively account for the presence of multiple sources.

The mathematical formulation of the eDCBF and extension to the *multi-core beamformer* (MCBF) are first presented to fully demonstrate the design of the new spatial filter. In simulations we demonstrate that the eDCBF spatial filter is robust to a wide range of correlations, SNRs, source locations, and various source temporal dynamics. Using a three-core MCBF filter, we further demonstrate how additional sources of interference can be accounted for once source localization is performed. Finally, we cross-validate our findings from

the simulations in an analysis of a human MEG recording during a stereo-auditory stimulation task, showing that the eDCBF produces meaningful correlation estimations and accurate time courses.

3.3 Methods

3.3.1 Previous Dual-core Beamformer Formulation (Diwakar et al., 2011)

The DCBF was developed assuming the presence of two sources. Let $\boldsymbol{L}_1$ and $\boldsymbol{L}_2$ define the lead-field matrices of the two sources of interest. The dual-core lead-field matrix is expressed as the *m x 4* matrix $\boldsymbol{L}_d = [\boldsymbol{L}_1 \quad \boldsymbol{L}_2]$. The DCBF weighting matrix is then defined as the *m x 1* vector $\boldsymbol{W}_d$ designed such that:

$$\hat{\boldsymbol{s}}(t) = \overline{\boldsymbol{v}}_{min}\boldsymbol{W}_d^T\boldsymbol{b}(t) \tag{3.1}$$

where $\hat{\boldsymbol{s}}(t)$ represents the *4 x 1* vector of estimated source time-courses in both the θ and ϕ directions. $\overline{\boldsymbol{v}}_{min}$ is defined as a *4 x 1* vector containing both optimal non-normalized *2 x 1* source orientations $\boldsymbol{\eta}_1$ and $\boldsymbol{\eta}_2$:

$$\overline{\boldsymbol{v}}_{min} = \begin{pmatrix}\boldsymbol{\eta}_1 \\ \boldsymbol{\eta}_2\end{pmatrix} \tag{3.2}$$

$\overline{\boldsymbol{v}}_{min}$ is obtained by computing the eigenvector associated with the weakest eigenvalue of $\boldsymbol{Q}_d = \boldsymbol{L}_d^T\boldsymbol{R}_b^{-1}\boldsymbol{L}_d$, where the dual-source power P_{opt}^d is represented by the inverse of the eigenvalue. The DCBF solution for the weighting matrix was shown to be (Diwakar and Huang et al., 2011):

$$\boldsymbol{W}_d = P_{opt}^{d} \boldsymbol{R}_b^{-1} \boldsymbol{L}_d \overline{\boldsymbol{v}}_{min} \tag{3.3}$$

The DCBF orientations from Equation 3.2 reduce $\boldsymbol{L}_d$ to a rank 1 scalar lead-field matrix leading to an *m x 1* beamformer weight (Equation 3.3), resulting in scaled copies of a single time-course to represent both sources. Furthermore, a single eigenvector of $\boldsymbol{Q}_d$ $(\overline{\boldsymbol{v}}_{min})$ can only capture either the correlated or uncorrelated part of the signal and is not sufficient to span the entire signal subspace, leading to incorrect estimates of source amplitude in the presence of correlated sources.

3.3.2 Enhanced Dual-core Beamformer Formulation

The enhanced Dual-core Beamformer (eDCBF) offers a novel solution to overcome the deficits of the previous DCBF. The eDCBF dual-core lead-field matrix is expressed identically to the original DCBF (Diwakar and Huang et al., 2011). Instead of using the DCBF *m x 1* weighting vector, the eDCBF weighting matrix is defined as the *m x 4* matrix $\boldsymbol{W}_d = [\boldsymbol{W}_1 \quad \boldsymbol{W}_2]$, where $\boldsymbol{W}_i$ are the individual weighting matrices for each source, ensuring no reduction in rank and enabling the computation of unique source time-courses and correlation. The eDCBF weighting matrix is designed such that:

$$\hat{\boldsymbol{s}}(t) = \boldsymbol{W}_d^T \boldsymbol{b}(t) \tag{3.4}$$

$\hat{\boldsymbol{s}}(t)$ is the *4 x 1* vector of unique estimated dual-source time-courses in both the θ and ϕ directions. As a measure of source strength and activity, the

4 x 4 eDCBF estimated dual-source covariance matrix $\boldsymbol{R}_{\hat{s}}$ is determined by taking the covariance of Equation 3.4:

$$\boldsymbol{R}_{\hat{s}} = \langle \hat{\boldsymbol{s}}(t)\hat{\boldsymbol{s}}(t)^T \rangle = \boldsymbol{W}_d^T \boldsymbol{R}_b \boldsymbol{W}_d \tag{3.5}$$

The constraints of the vector minimum-variance beamformer, consistently shown to produce accurate beamformer reconstruction with single sources (Sekihara et al., 2004; Spencer et al., 1992; Van Veen et al., 1997), may be used to derive the eDCBF weighting matrix $\boldsymbol{W}_d$**:**

$$\boldsymbol{W}_d = \arg\min_{\boldsymbol{W}_d} tr\{\boldsymbol{W}_d^T \boldsymbol{R}_b \boldsymbol{W}_d\} \text{ subject to } \boldsymbol{W}_d^T \boldsymbol{L}_d = \boldsymbol{I} \tag{3.6}$$

The matrix product $\boldsymbol{W}_d^T \boldsymbol{L}_d$ represents the spatial filter output from two unit-magnitude impulse currents. The linear constraint $\boldsymbol{W}_d^T \boldsymbol{L}_d = \boldsymbol{I}$ ensures that each weighting vector $\boldsymbol{W}_i$ passes signal from its respective source while not passing signal from the second source. Furthermore, the trace of the beamformer output source power $\boldsymbol{W}_d^T \boldsymbol{R}_b \boldsymbol{W}_d$ is minimized to suppress both noise and additional source contributions. However, no assumptions are made about the correlation between the two sources of interest. In fact, the correlation can take on any value from 0 for uncorrelated sources to 1 for completely synchronized sources. The solution for the minimization problem may be obtained by minimizing the Lagrangian with Lagrange multiplier $\boldsymbol{\kappa}$:

$$\mathcal{L}(\boldsymbol{W}_d, \boldsymbol{\kappa}) = tr\{\boldsymbol{W}_d^T \boldsymbol{R}_b \boldsymbol{W}_d + (\boldsymbol{W}_d^T \boldsymbol{L}_d - \boldsymbol{I})\boldsymbol{\kappa}\} \tag{3.7}$$

The derivative of the Lagrangian may be computed using the matrix derivative identities $\frac{\partial}{\partial \boldsymbol{X}} tr\{\boldsymbol{X}^T \boldsymbol{A}\} = \boldsymbol{A}$ and $\frac{\partial}{\partial \boldsymbol{X}} tr\{\boldsymbol{X}^T \boldsymbol{A}\boldsymbol{X}\} = \boldsymbol{A}\boldsymbol{X} + \boldsymbol{A}^T\boldsymbol{X}$:

$$\frac{\partial \mathcal{L}(\boldsymbol{W}_d, \boldsymbol{\kappa})}{\partial \boldsymbol{W}_d} = 2\boldsymbol{R}_b\boldsymbol{W}_d + \boldsymbol{L}_d\boldsymbol{\kappa} = \boldsymbol{0} \tag{3.8}$$

$$\boldsymbol{W}_d = -\frac{\boldsymbol{R}_b^{-1}\boldsymbol{L}_d\boldsymbol{\kappa}}{2} \tag{3.9}$$

Substituting the unit-gain constraint $\boldsymbol{W}_d^T\boldsymbol{L}_d = \boldsymbol{I}$ into Equation 3.9 yields:

$$\boldsymbol{\kappa} = -2(\boldsymbol{L}_d^T\boldsymbol{R}_b^{-1}\boldsymbol{L}_d)^{-1} \tag{3.10}$$

$$\boldsymbol{W}_d = \boldsymbol{R}_b^{-1}\boldsymbol{L}_d(\boldsymbol{L}_d^T\boldsymbol{R}_b^{-1}\boldsymbol{L}_d)^{-1} \tag{3.11}$$

The eDCBF estimated dual-source covariance matrix $\boldsymbol{R}_{\hat{s}}$, which is equal to the inverse of the DCBF $\boldsymbol{Q}_{dual}$, may be obtained by substituting the derived eDCBF beamformer weight (Equation 3.11) into Equation 3.5:

$$\boldsymbol{R}_{\hat{s}} = \boldsymbol{W}_d^T\boldsymbol{R}_b\boldsymbol{W}_d = (\boldsymbol{L}_d^T\boldsymbol{R}_b^{-1}\boldsymbol{L}_d)^{-1} \tag{3.12}$$

The eDCBF time-courses are obtained by substituting the derived eDCBF beamformer weight from Equation 3.11 into Equation 3.4:

$$\hat{\boldsymbol{s}}(t) = \boldsymbol{W}_d^T\boldsymbol{b}(t) = (\boldsymbol{L}_d^T\boldsymbol{R}_b^{-1}\boldsymbol{L}_d)^{-1}\boldsymbol{L}_d^T\boldsymbol{R}_b^{-1}\boldsymbol{b}(t) = \boldsymbol{R}_{\hat{s}}\boldsymbol{L}_d^T\boldsymbol{R}_b^{-1}\boldsymbol{b}(t) \tag{3.13}$$

The eDCBF uses the full dual-source covariance matrix ($\boldsymbol{R}_{\hat{s}}$ or $\boldsymbol{Q}_d^{-1}$) instead of a single eigenvector when determining the weighting matrix, preventing undesired amplitude suppression and allowing reconstruction of

unique time-courses. Thus, the eDCBF makes it possible to define and compute source correlation.

3.3.3 eDCBF Estimated Correlation Reconstruction

The eDCBF estimated vector covariance matrix $\boldsymbol{R}_{\hat{s}}$ can be expressed as:

$$\boldsymbol{R}_{\hat{s}} = \begin{bmatrix} \langle \hat{s}_1(t)\hat{s}_1(t)\rangle \overline{\boldsymbol{\eta}}_1 \overline{\boldsymbol{\eta}}_1^T & \langle \hat{s}_1(t)\hat{s}_2(t)\rangle \overline{\boldsymbol{\eta}}_1 \overline{\boldsymbol{\eta}}_2^T \\ \langle \hat{s}_2(t)\hat{s}_1(t)\rangle \overline{\boldsymbol{\eta}}_2 \overline{\boldsymbol{\eta}}_1^T & \langle \hat{s}_2(t)\hat{s}_2(t)\rangle \overline{\boldsymbol{\eta}}_2 \overline{\boldsymbol{\eta}}_2^T \end{bmatrix} \tag{3.14}$$

where $\hat{s}_i(t)$ are the estimated scalar source time-courses and $\overline{\boldsymbol{\eta}}_i$ are the *2 x 1* normalized orientations for the two sources. The two diagonal *2 x 2* sub-matrices of $\boldsymbol{R}_{\hat{s}}$ are of the same form as SBF vector covariance matrices (Sekihara et al., 2004). Thus, the eigenvectors corresponding to the maximum eigenvalues (signal-related) of these sub-matrices contain the source orientations, while the eigenvectors corresponding to the minimum eigenvalues (noise-related) contain the noise orientations. The *4 x 2* source orientation matrix $\boldsymbol{\psi}$ is used to reduce the *4 x 4* vector source covariance matrix to the *2 x 2* estimated dual-source scalar covariance matrix $\widetilde{\boldsymbol{R}}_{\hat{s}}$:

$$\boldsymbol{\psi} = \begin{pmatrix} \overline{\boldsymbol{\eta}}_1 & 0 \\ 0 & \overline{\boldsymbol{\eta}}_2 \end{pmatrix} \tag{3.15}$$

$$\widetilde{\boldsymbol{R}}_{\hat{s}} = \boldsymbol{\psi}^T \boldsymbol{R}_{\hat{s}} \boldsymbol{\psi} \tag{3.16}$$

The orientation matrix also allows scalar source time-course recovery:

$$\tilde{\boldsymbol{s}}(t) = \boldsymbol{\psi}^T \boldsymbol{W}_d^T \boldsymbol{b}(t) \tag{3.17}$$

The estimated dual-source power correlation $\hat{\chi}_{12}$ may be computed from:

$$\hat{\chi}_{12} = \frac{\widetilde{\boldsymbol{R}}_{\hat{s}}(1,2)^2}{\widetilde{\boldsymbol{R}}_{\hat{s}}(1,1)\widetilde{\boldsymbol{R}}_{\hat{s}}(2,2)} \tag{3.18}$$

Amplitude correlation $\hat{\chi}_{12}^{a}$ can be computed as the square root of Equation 3.18.

3.3.4 eDCBF Transformed Correlation Reconstruction

Often, it is desirable to examine the source activity in a certain frequency band or envelope of the source signals. The eDCBF weighting matrix $\boldsymbol{W}_d$ can be derived from either the transformed or original sensor recordings. Use of the original recordings allows determination of source orientations and $\boldsymbol{W}_d$ based on the complete source power spectrum, which is more representative of true source activity. Furthermore, the eDCBF provides a straightforward way to compute correlations and time courses when $\boldsymbol{W}_d$ has been derived from the original signal. $\hat{\boldsymbol{s}}_{\xi}(t)$, the transformed time courses of $\hat{\boldsymbol{s}}(t)$, are defined by transforming Equation 3.13 in the time-domain:

$$\hat{\boldsymbol{s}}_{\xi}(t) = \boldsymbol{\xi}[\hat{\boldsymbol{s}}(t)] = \boldsymbol{W}_d^T \boldsymbol{\xi}[\boldsymbol{b}(t)] = \boldsymbol{W}_d^T \boldsymbol{b}_{\xi}(t) \tag{3.19}$$

where $\boldsymbol{b}_{\xi}(t)$ are the transformed sensor time-courses and $\boldsymbol{\xi}$ is the operator of the transformation. The transformed source covariance matrix $\boldsymbol{R}_{\hat{s}}^{\xi}$ may be

computed with the transformed sensor covariance matrix $\boldsymbol{R}_b^{\xi} = \langle \boldsymbol{b}_{\xi}(t)\boldsymbol{b}_{\xi}(t)^T \rangle$ without computation of source time-courses:

$$\boldsymbol{R}_{\hat{s}}^{\xi} = \langle \hat{\boldsymbol{s}}_f(t)\hat{\boldsymbol{s}}_f(t)^T \rangle = \boldsymbol{W}_d^T \boldsymbol{R}_b^{\xi} \boldsymbol{W}_d \tag{3.20}$$

The estimated correlation may be computed from the transformed source covariance matrix in the same fashion as Equations 3.16 and 3.18. Furthermore, Equations 3.19 and 3.20 hold for any linear transformations in the time domain.

3.3.5 eDCBF Regularized Correlation Reconstruction

Use of the regularized beamformer has greatly improved the quality of beamformer signal time-course reconstruction (Robinson and Vrba, 1998; Van Veen et al., 1997; Hillebrand et al., 2005). The eDCBF beamformer weight can be reformulated to obtain the regularized beamformer weight $\boldsymbol{W}_d^r$

$$\boldsymbol{W}_d^r = (\boldsymbol{R}_b + \gamma \boldsymbol{I})^{-1} \boldsymbol{L}_d (\boldsymbol{L}_d^T (\boldsymbol{R}_b + \gamma \boldsymbol{I})^{-1} \boldsymbol{L}_d)^{-1} \tag{3.21}$$

where γ is the regularization parameter that increases the full-width half-maximum of the beamformer point-spread function while reducing the amount of uncorrelated noise. Source time-courses may be reconstructed as:

$$\hat{\boldsymbol{s}}_r(t) = (\boldsymbol{W}_d^r)^T \boldsymbol{b}(t) \tag{3.22}$$

Source correlation may be computed from the regularized estimated source covariance matrix $\boldsymbol{R}_{\hat{s}}^{r}$ without computation of time courses using Equations 3.16 and 3.18.

$$\boldsymbol{R}_{\hat{s}}^{r} = \langle \hat{\boldsymbol{s}}_r(t)\hat{\boldsymbol{s}}_r(t)^T \rangle = (\boldsymbol{W}_d^r)^T \boldsymbol{R}_b \boldsymbol{W}_d^r \tag{3.23}$$

Correlation and time courses in specific frequency bands may be computed by using the regularized beamformer weight $\boldsymbol{W}_d^r$ in conjunction with Equations 3.19 and 3.20.

3.3.6 eDCBF Noise-corrected Correlation Reconstruction

The estimated dual-source covariance matrix can be heavily biased by the presence of noise, making true prediction of correlation difficult. Further investigation reveals that this bias can be corrected using the sensor noise covariance $\boldsymbol{R}_n$**.** The expression for $\boldsymbol{R}_b$ from Equation 1.15 may be equivalently written as $\boldsymbol{R}_b = \tilde{\boldsymbol{L}}\tilde{\boldsymbol{R}}_s^p\tilde{\boldsymbol{L}}^T + \boldsymbol{R}_n$, where the scalar composite lead-field matrix is given by $\tilde{\boldsymbol{L}} = [\boldsymbol{l}_1 \quad \boldsymbol{l}_2 \quad \cdots \quad \boldsymbol{l}_p]$ and $\tilde{\boldsymbol{R}}_s^p$ is the *p x p* scalar source covariance matrix**.** The *m x 1* vectors $\boldsymbol{l}_i$ that comprise $\tilde{\boldsymbol{L}}$ are the scalar lead-fields for each source along its true orientation $\bar{\boldsymbol{\eta}}_i$ where $\boldsymbol{l}_i = \boldsymbol{L}_i\bar{\boldsymbol{\eta}}_i$. By substituting this expression for $\boldsymbol{R}_b$ into Equation 3.5, it is evident that the estimated source covariance matrix $\boldsymbol{R}_{\hat{s}}$ is composed of a noise-free component (first term on the right-hand-most side of Equation 3.24) and a noise-related component (second term on the right-hand-most side of Equation 3.24):

$$\boldsymbol{R}_{\hat{s}} = \langle \hat{\boldsymbol{s}}(t)\hat{\boldsymbol{s}}(t)^T \rangle = \boldsymbol{W}_d^T \boldsymbol{R}_b \boldsymbol{W}_d = \boldsymbol{W}_d^T \tilde{\boldsymbol{L}} \tilde{\boldsymbol{R}}_s^p \tilde{\boldsymbol{L}}^T \boldsymbol{W}_d + \boldsymbol{W}_d^T \boldsymbol{R}_n \boldsymbol{W}_d \tag{3.24}$$

The process of minimization and application of linear constraints result in weight vectors that satisfy $\boldsymbol{W}_d^T \boldsymbol{l}_i = \boldsymbol{0}$ for $i: 3 \rightarrow p$ by assuming that the corresponding sources are uncorrelated with each other as well as the two sources of interest (Sekihara et al., 2002). The noise-free component then reduces to the *4 x 4* true dual-source vector covariance matrix $\boldsymbol{R}_s$:

$$\boldsymbol{W}_d^T \tilde{\boldsymbol{L}} \tilde{\boldsymbol{R}}_s^p \tilde{\boldsymbol{L}}^T \boldsymbol{W}_d = \boldsymbol{R}_s \tag{3.25}$$

Equation 3.25 also remains valid when only two sources are present. When additional partially correlated sources exist, the multi-core extension presented in the next section must be used. Equation 3.24 then simplifies to:

$$\boldsymbol{R}_{\hat{s}} = \boldsymbol{R}_s + \boldsymbol{W}_d^T \boldsymbol{R}_n \boldsymbol{W}_d \tag{3.26}$$

Substituting the derived beamformer weight Equation 3.11 into Equation 3.26 and solving for $\boldsymbol{R}_s$ yields:

$$\boldsymbol{R}_s = (\boldsymbol{I} - \boldsymbol{R}_{\hat{s}} \boldsymbol{L}_d^T \boldsymbol{R}_b^{-1} \boldsymbol{R}_n \boldsymbol{R}_b^{-1} \boldsymbol{L}_d) \boldsymbol{R}_{\hat{s}} \tag{3.27}$$

To obtain the noise-corrected correlation, an unbiased estimate of the noise covariance $\boldsymbol{R}_n$ is essential. The true dual-source vector covariance matrix can then be reduced using the derived orientations to the *2 x 2* true dual-source scalar covariance matrix $\tilde{\boldsymbol{R}}_s$ to compute the noise-corrected correlation value χ_{12}:

$$\widetilde{\boldsymbol{R}}_s = \boldsymbol{\psi}^T \boldsymbol{R}_s \boldsymbol{\psi} \tag{3.28}$$

$$\chi_{12} = \frac{\widetilde{\boldsymbol{R}}_s(1,2)^2}{\widetilde{\boldsymbol{R}}_s(1,1)\widetilde{\boldsymbol{R}}_s(2,2)} \tag{3.29}$$

Using the definition of the matrix $\boldsymbol{K} = \boldsymbol{W}_d^T \boldsymbol{R}_n \boldsymbol{W}_d (\boldsymbol{W}_d^T \boldsymbol{R}_b \boldsymbol{W}_d)^{-1} = \boldsymbol{R}_{\hat{s}} \boldsymbol{L}_d^T \boldsymbol{R}_b^{-1} \boldsymbol{R}_n \boldsymbol{R}_b^{-1} \boldsymbol{L}_d$ from the original DCBF (Diwakar and Huang et al., 2011), Equation 3.27 can be written as:

$$\boldsymbol{R}_s = (\boldsymbol{I} - \boldsymbol{K}) \boldsymbol{R}_{\hat{s}} \tag{3.30}$$

Thus, the relationship between the true dual-source vector covariance and the estimated dual-source vector covariance is dependent on the $\boldsymbol{K}$ matrix, which is inversely proportional to the source space SNR. As shown previously, the K-related dual-source pseudo-Z-score (Z^K) may be obtained by inverting the minimum eigenvalue of the $\boldsymbol{K}$ matrix (Robinson and Vrba, 1998; Vrba and Robinson, 2001; Sekihara et al., 2004; Diwakar et al., 2011):

$$Z^K = Z_{opt}^d = \min\big(eig(\boldsymbol{K})\big)^{-1} \tag{3.31}$$

This pseudo-Z-score can be used as a measure of relative source activity. Alternatively, the power pseudo-Z-score may be computed by dividing the dual source power by the noise power (Van Veen et al., 1997):

$$Z^P = \frac{tr\{\boldsymbol{R}_{\hat{s}}\}}{tr\{(\boldsymbol{L}_d^T \boldsymbol{R}_n^{-1} \boldsymbol{L}_d)^{-1}\}} \tag{3.32}$$

The differences in the spatial profile of Z^K and Z^P will be investigated in the Results.

3.3.7 Extension to Multi-core Beamformer (MCBF)

We previously demonstrated that using DCBF to model two sources is sufficient to reveal complex neuronal networks with many sources due to only partial suppression of the pseudo-Z-score (Diwakar and Huang et al., 2011). However, as shown by Equation 3.25, the eDCBF can only account for two correlated sources in the presence of other uncorrelated sources. When multiple correlated sources exist, the correlation coefficient and time-course reconstruction are affected severely. Therefore, the model needs to be expanded to handle such environments.

A *multi-core beamformer* (MCBF) can be developed to account for additional sources. The technique can be described by a straightforward extension of the eDCBF. Starting from Equation 1.15, the multi-core lead-field vector is defined as the *m x 2c* matrix $\boldsymbol{L}_m = [\boldsymbol{L}_1 \quad \boldsymbol{L}_2 \quad \cdots \quad \boldsymbol{L}_c]$, where *c* is the desired number of sources to be modeled. The corresponding multi-core weighting vector is then defined as the *m x 2c* matrix $\boldsymbol{W}_m = [\boldsymbol{W}_1 \quad \boldsymbol{W}_2 \quad \cdots \quad \boldsymbol{W}_c]$. The solution to the multi-core weighting vector, $\boldsymbol{W}_m$, is derived in an equivalent manner to Equations 3.6 through 3.11:

$$\boldsymbol{W}_m = \boldsymbol{R}_b^{-1}\boldsymbol{L}_m(\boldsymbol{L}_m^T\boldsymbol{R}_b^{-1}\boldsymbol{L}_m)^{-1} \tag{3.33}$$

The derivations presented from Equations 3.12 to 3.29 can be then applied to the multi-core beamformer to obtain the *2c x 2c* estimated multi-core vector covariance matrix $\boldsymbol{R}_{\hat{s}}$, the *2c x 2c* true multi-core vector covariance matrix $\boldsymbol{R}_{s}$, the *c x c* estimated multi-core scalar covariance matrix $\widetilde{\boldsymbol{R}}_{\hat{s}}$, and the *c x c* true multi-core scalar covariance matrix $\widetilde{\boldsymbol{R}}_{s}$. The orientation vector $\boldsymbol{\psi}$ is defined as:

$$\boldsymbol{\psi} = \begin{pmatrix} \overline{\boldsymbol{\eta}}_1 & 0 & \cdots & 0 \\ 0 & \overline{\boldsymbol{\eta}}_2 & \cdots & 0 \\ \vdots & \vdots & \ddots & \vdots \\ 0 & 0 & \cdots & \overline{\boldsymbol{\eta}}_c \end{pmatrix} \tag{3.34}$$

The estimated pair-wise correlation $\hat{\chi}_{ij}$ and the noise-corrected pair-wise power correlation χ_{ij} between the i^{th} and j^{th} sources are given by:

$$\hat{\chi}_{ij} = \frac{\widetilde{\boldsymbol{R}}_{\hat{s}}(i,j)^2}{\widetilde{\boldsymbol{R}}_{\hat{s}}(i,i)\widetilde{\boldsymbol{R}}_{\hat{s}}(j,j)} \tag{3.35}$$

$$\chi_{ij} = \frac{\widetilde{\boldsymbol{R}}_{s}(i,j)^2}{\widetilde{\boldsymbol{R}}_{s}(i,i)\widetilde{\boldsymbol{R}}_{s}(j,j)} \tag{3.36}$$

Amplitude correlation can be computed as the square root of Equations 3.35 and 3.36. The formulation of the MCBF is similar to that of the NB and CSSM except that instead of deriving the beamformer weight for only one source of interest at a time, the MCBF applies additional constraints to simultaneously find weights for all modeled sources (Dalal et al., 2006; Hui and Leahy, 2006; Hui and Leahy, 2010; Quuran and Cheyne, 2010). This

feature allows correlation reconstruction of multiple interfering sources at the same time. The MCBF requires three degrees of freedom for spatial location and two degrees of freedom for orientation per core. Theoretically, if all signals from *m* sensors are linearly independent and signal-related (achieved at infinite SNR), the MCBF can model a maximum of m/5 sources. However, at the typical SNR of real measurements recorded on a modern MEG system, the number of signal-related independent spatial modes is approximately 40-50, allowing the MCBF to model a maximum of 8-10 sources. The MCBF is most appropriately used to determine source activity for a given set of sources that already have been accurately localized by methods utilizing a metric such as the DCBF pseudo-Z-score (Diwakar and Huang et al., 2011).

3.3.8 General Setup for Simulations

To measure the performance of the eDCBF spatial filter for both correlation and temporal reconstruction, a series of computer simulations were conducted with a simulator designed to allow variation of the sources present (number, location, orientation) and their corresponding waveforms (frequency, amplitude, lag, duration, SNR), thereby providing vast flexibility for simulation execution.

The source space was simulated with a grid covering the cortical gray matter with homogenous 5 mm spacing in the x, y, and z directions. The cortical boundaries were obtained from a healthy subject's T1-weighted

anatomical MRI. The sensor configuration was based on the Elekta/Neuromag^{TM} whole-head MEG system (VectorView), in which 306 sensors are arranged on a helmet-shaped surface (204 gradiometers and 102 magnetometers). The source-sensor configuration is shown in Figure 3.1 (inner-skull surface represented by gray mesh).

To compute the forward model, the boundary element method (BEM) was employed where the inner-skull surface (from MRI) served as the BEM mesh (size 5mm). SNR levels were adjusted by adding uncorrelated random Gaussian noise to the sensor waveforms, where the SNR was defined as the ratio of the Frobenius norm of the signal vector to that of the noise vector calculated over the interval with signal. Using the simulator, eDCBF correlation and time-course reconstruction were inspected over varying source coherence, SNRs, and temporal dynamics. Additional simulations were designed to test the eDCBF at various source separations as well as to investigate correlation estimation for the three-core MCBF.

3.3.9 Setup for SNR, Correlation, and Time-course Simulations

Two source dipoles were placed in the left and right hemisphere auditory cortices (Figure 3.1). Their signals were composed of a 6-second inactive period followed by 6 seconds of a sinusoidal wave with amplitude of 5 nAm and frequency of 30 Hz (sampling rate 1000 Hz). The phase shift of the second source was varied from 0° to 90° in steps of 10° to test a wide range of

correlations. Reconstruction of the estimated correlation and the noise-corrected correlation was carried out at SNRs of 4, 2, 1, 0.5, 0.25, and 0.167. Estimation of source amplitudes was carried out by FFT examination of extended length (50x) source time-course reconstructions over all phase lags and SNRs. To test time-course recovery of a more complicated signal, a linear chirp was utilized, wherein the frequency was varied from 5 to 10 Hz (and back) over a period of 5 seconds and the amplitude was modulated by a 0.1 Hz sinusoid. Noise-corrected correlation was computed for all SNRs and for source time-lags of 0.05, 0.1, 0.4 and 1 second. Source time-courses and RMS amplitudes were calculated at all time-lags and at an SNR of 4. Finally, Monte Carlo methods were employed to properly quantify the results' probability distribution (1000 simulations unless otherwise noted).

3.3.10 Setup for Location Simulations

To test eDCBF reconstruction at varying source locations, the sinusoidal simulation from the previous section was performed for two additional sets of sources. Noise-corrected correlation values were computed for distantly-placed sources in the left and right hemisphere primary motor cortices with a separation of 70 mm and for closely-placed sources in the left and right posterior cingulate cortex (PCC) with a separation of 5 mm (Figure 3.1). A set of 1000 randomly chosen source pairs was also tested for noise-corrected correlation accuracy at a fixed SNR of 4.

3.3.11 Setup for Three-core MCBF Simulation

An additional simulation was designed to test MCBF performance for a core size of three. Sources were placed in the PCC and the left and right primary motor cortices. The right motor cortex source's phase lag ranged from 45° to 90° (in steps of 5°) whereas the PCC source's phase lag decreased from 45° to 0° (in steps of 5°), creating a variety of correlation conditions. The simulation was executed 1000 times to compute the noise-corrected correlation for the full SNR and correlation ranges.

3.3.12 Setup for Human MEG Auditory Study

A stereo auditory test stimulus was designed to compare eDCBF correlation and time-course reconstruction in actual MEG measurements (200 epochs of evoked responses) to reconstruction using two-dipole fit, a method known to adequately represent neuronal activity in the auditory cortices (Mosher et al., 1992; Mosher and Leahy 1998; Mosher et al., 1999; Huang et al., 1998). The test sound file consisted of 1800 ms of pre-stimulus silence followed by a 2000 ms stereo stimulus period. The stimulus consisted of a 500-Hz pure tone with a 40-Hz envelope modulated at 100% level. The modulation envelopes between the left and right channels were designed to be fully correlated. The intensities of the left and right channels were balanced for equal sensitivity for the left and right ears. The start and end of the stimulus epochs were smoothed with a cosine roll-off to prevent any artifacts.

Magnetic fields evoked by auditory stimulation were measured using an Elekta/Neuromag^{TM} whole-head MEG system (VectorView) with 204 gradiometers and 102 magnetometers in a magnetically shielded room (IMEDCO-AG, Switzerland). EOG electrodes were used to detect eye blinks and eye movements.

Intervals of 1400 ms of post-stimulus data and 200 ms of pre-stimulus data were used for analysis (gradiometers only). Data were sampled at 1000 Hz and processed by MaxFilter to remove environment noise (Taulu et al., 2004; Taulu and Simola, 2006; Song et al., 2008; Song et al., 2009). Artifact-free MEG responses (n=181) were averaged with respect to the stimulus trigger. A BEM mesh of 5-mm size for the subject was generated from the inner-skull surface using a set of T1-weighted MRI images taken on a 1.5 T MRI scanner. Registration of MRI and MEG was performed using data obtained from the Polhemus Isotrak system prior to MEG scanning.

Reconstructions of MEG auditory recordings with the eDCBF, SBF, and dipole-fit modeling were compared to assess the accuracy and validity of the eDCBF reconstruction. SVD was used to separate the original sensor measurements into signal and noise components. The top eight singular modes were chosen as a conservative estimate of the noise-free signal based on manual inspection of the elbow-shaped region of the singular value spectrum. The remaining singular modes were considered to contain only the noise-related signal. The noise components were removed and replaced with

white noise of the same power, resulting in an estimated SNR of 3.7 and allowing construction of a noise covariance matrix. A regularization parameter equal to 4% of the largest eigenvalue of $\boldsymbol{R}_b$ was used for reconstruction with both the eDCBF and the vector SBF (Van Veen et al., 1997; Sekihara et al., 2002; Sekihara et al., 2004).

Dual-source localization was performed with a Nelder-Mead downhill simplex search for the maximum power pseudo-Z-score. The eDCBF regularized beamformer weight $\boldsymbol{W}_d^r$ was computed and used with Equations 3.22, 3.19, and 3.17 to generate unfiltered and low-pass filtered (< 50 Hz) regularized time-courses for each source. Inter-hemispheric correlation values were computed from filtered time-courses, from the source covariance matrix presented in Equation 3.20, and from the noise-corrected source covariance matrix. Vector-based SBF was also used to reconstruct unfiltered and filtered regularized time-courses for the source locations identified by the eDCBF. Inter-hemispheric correlations were computed with the reconstructed filtered regularized SBF time-courses for comparison.

Localization was also performed using a multi-start downhill simplex dipole-fit algorithm with a spherical head model (Huang et al., 1998). The fitted locations were further refined with a BEM forward model. The dipole-fit source time-course reconstruction was obtained by multiplying the pseudo-inverse of the gain matrix for the fitted dipoles and the sensor measurements. Inter-hemispheric correlations were computed with unfiltered and low-pass

filtered dipole-fit source time-courses (< 50 Hz). Correlations were also computed between filtered regularized reconstructions (eDCBF and SBF) and filtered time-courses obtained from dipole fit as a measure of time-course similarity.

3.4 Results

3.4.1 Analysis of eDCBF Across Entire Correlation Range

To test the performance of eDCBF across the entire range of possible correlations, a phase lag was introduced to the sinusoid of the second source. The simulation was performed with an SNR of 4, minimizing noise effects so that the eDCBF's sensitivity to correlation was emphasized. Source reconstruction was completed using estimated correlation reconstruction. Table 3.1 shows that eDCBF estimates of the sources' time-course correlations are highly accurate ($\varepsilon < 0.003, \sigma \leq 0.0013$, where ε is the error, and σ is the standard deviation across Monte Carlo iterations) regardless of the actual value of the correlation. In addition, the low standard deviation demonstrates eDCBF's exceptional stability. Accuracy of source localization was not examined here, as it was already confirmed with the original DCBF (Diwakar and Huang et al., 2011).

3.4.2 Examination of eDCBF Performance Across SNR Range

Real-world noise commonly dominates the underlying signal, frequently posing a problem for beamformers. Therefore, we characterized eDCBF performance across a range of SNR values. The following simulation allowed comparison of the estimated and noise-corrected correlation reconstruction from Equations 3.18 and 3.29. We observed that even though the estimated correlation works well initially, as SNR drops below 1, the accuracy of eDCBF estimated correlations fell to unacceptable levels. By a SNR level of 0.167, the filter became practically ineffective and was unable to appropriately resolve the underlying signal ($\bar{\varepsilon} < 0.32$), where $\bar{\varepsilon}$ is the averaged correlation error over all phase shifts for a given SNR. From the noise time-courses (added to sensor waveforms to create the desired SNR), an unbiased estimate of the noise covariance matrix was used to examine the noise-corrected correlation. The correction allowed the beamformer to perform successfully at the entire range of SNR and correlation values ($\bar{\varepsilon} < 0.0008, \bar{\sigma} < 0.011$), where $\bar{\sigma}$ is the averaged Monte Carlo standard deviation across all phase shifts in a given SNR (Figure 3.2), rendering eDCBF an extremely robust and flexible beamformer filter given a reasonably accurate estimation of the noise covariance.

3.4.3 Validation of eDCBF Performance Regardless of Source Location

The sensitivity of the eDCBF filter to the location of the two sources was investigated by examining three cases: a pair of distantly-spaced dipoles, a pair of closely spaced dipoles, and a pair of randomly placed dipoles. For distant dipoles, we observed that the correlation reconstruction worked precisely throughout the entire SNR and correlation ranges $(\bar{\varepsilon} < 0.0005, \bar{\sigma} < 0.009)$. When dipoles were closely placed (PCC dipoles spaced only 5 mm apart), a hindrance for beamformer operation at low SNR, the eDCBF still performed effectively. At SNRs at or above 0.5, the eDCBF was reasonably accurate $(\bar{\varepsilon} < 0.005, \bar{\sigma} < 0.036)$, while at SNRs of 0.25 or lower it slightly overestimated the correlation value $(\bar{\varepsilon} < 0.027, \bar{\sigma} < 0.11)$ due to bias in the noise covariance estimate at very low SNRs (Figure 3.3). Finally, the eDCBF filter still performed accurately when dipole pairs were chosen randomly $(\varepsilon < 0.0002, \sigma < 0.003)$.

3.4.4 Time-course Reconstruction – Sinusoid/Chirp Source Waveforms

For most of the simulations, a sinusoid wave was used to construct the source signal. To investigate the precision of the reconstructed waveform, we examined the accuracy of the reconstructed amplitude as the SNR and phase lag were varied, which is another concern associated with previous dual beamformers. Figure 3.4 shows a set of reconstructed waveforms (for the entire range of phase shifts) at SNR of 4 computed from Equation 3.17. As

shown in Table 3.2, eDCBF reconstructed the amplitude with the same success regardless of SNR or correlation value, underestimating by more than 1% only in a single case. The small bias in amplitude estimation occurs due to a rank deficient sensor covariance matrix before the addition of noise. Amplitudes estimated from the eDCBF were far more accurate than those from the previous DCBF, which were suppressed by an average of 12.5% (Diwakar and Huang et al., 2011).

Since neuronal signals typically contain complex features, a more sophisticated waveform in the form of a linear chirp was also considered. To simulate various correlations, a series of time lags were introduced to the chirp present in the second source. Figure 3.5 shows an example of the reconstructed waveform for a one-second time-lag at a SNR of 4 for the sensor waveforms. To quantitatively asses the reconstruction, an RMS amplitude measure was employed. When comparing the original waveform's amplitude with the reconstructed waveform (for the example above), it was accurate to 99.9%. The accuracy of the correlation computation was also tested (1000 Monte Carlo simulations). Figure 3.6 shows that the eDCBF successfully estimates the correlation for any combination of SNR and time lag $(\bar{\varepsilon} < 0.0004, \bar{\sigma} < 0.007)$.

3.4.5 Three-source Simulation with MCBF

The last simulation examined the performance of the MCBF filter when reconstructing three simultaneously-active correlated sources. Currently, no beamformer method is able to properly address this issue. MCBF performance in reconstructing the source correlation values for all three dipole combinations can be seen in Figure 3.7. For any given condition, MCBF properly reconstructed all correlation values $(\bar{\varepsilon} < 0.005, \bar{\sigma} < 0.04)$.

3.4.6 Human Auditory Reconstruction Results

The two-dipole-fit reconstruction of the evoked MEG auditory response to the 500-Hz pure tone with a 40-Hz envelope (Figure 3.8) showed bilateral activation of both the left and right auditory cortices. The left hemisphere neuronal source (blue) showed a large transient response followed by a steady-state response with a weak 40-Hz component. The right hemisphere neuronal source (green) revealed a slightly smaller transient response with strong 40-Hz steady-state oscillations from 500 ms to 1400 ms.

During eDCBF reconstruction of the auditory response, maximizing the power pseudo-Z-score (34) appropriately localized sources to the left and right auditory cortices (Figure 3.9). Though the K-related pseudo-Z-score provides a valid method of localization at low SNRs as shown previously (Diwakar and Huang et al., 2011), its spatial distribution at high SNR is sharply peaked, rendering it unsuitable for grid spacing of a few millimeters. However, the

power pseudo-Z-score provides a suitable measure of detection for high SNR recordings (Figure 3.10). Localization of the auditory response found by dipole-fit and the eDCBF differed by less than 2.5 mm for each hemisphere (Figure 3.9).

The eDCBF regularized recovery of source time-courses (Figure 3.11 – left panels) showed individual signals for the left (blue) and right (green) hemisphere neuronal sources. Furthermore, examination of both right and left source signals showed well-defined transient and steady-state responses that closely resembled the time courses obtained from dipole-fit as indicated by high correlations ($\chi_L^a = 0.9630$; $\chi_R^a = 0.9614$). In contrast, SBF regularized time-courses (Figure 11 – right panels) correlated poorly with those obtained from dipole-fit ($\chi_L^a = 0.5018$; $\chi_R^a = 0.4946$). In fact, even features such as the larger, left-sided transient response and the stronger, right-sided 40-Hz steady-state response were preserved with the eDCBF. The errors in the SBF reconstruction were due to inaccurate determination of source orientations and the false assumption that sources are uncorrelated.

Correlations for dipole-fit time-courses showed strong coherence between the left and right auditory cortices ($\chi^a = 0.9535$, $\chi_{filt}^a = 0.9567$). The eDCBF noise-corrected correlation ($\chi_{reg}^a = 0.9349$) and the filtered eDCBF correlation ($\hat{\chi}_{reg,filt}^a = 0.9385$) agreed with these values ($\Delta\chi^a < 3\%$). However, the SBF-predicted correlation ($\hat{\chi}_{reg,filt}^a = 0.6119$) was quite poor

($\Delta\chi^a \approx 35\%$). Correlations computed from eDCBF time-courses and from the appropriate source covariance matrices were identical.

3.5 Discussion

The present study provides an improved implementation of our previously introduced DCBF, which was unable to accurately estimate source amplitudes or produce unique time-courses and correlations to characterize source activity (Diwakar and Huang et al., 2011). The eDCBF provides a novel approach designed to reconstruct the source power covariance matrix $\boldsymbol{R}_{\hat{s}}$ between multiple sources. With this matrix, individual time-courses and correlations for sources can be determined in low SNR conditions, overcoming the deficits of the DCBF.

Computationally, multiple source beamformers (e.g. DSBF, DCBF, eDCBF) require some searching for the optimum source configuration unlike traditional beamformers. Single beamformers may therefore appear more attractive as quick scanning methods but are less accurate due to the strict assumption of non-correlated sources (Robinson and Vrba, 1998; Sekihara et al., 2002; Van Drongelen et al., 1996; Van Veen et al., 1997). Furthermore, unlike beamformer spatial filters that are designed to work in a correlated environment (e.g. NB, CSSM, and AGMN-RUG), the eDCBF requires only a single computation of the weight matrix for accurate correlation determination

(Dalal et al., 2006; Hui and Leahy, 2006; Hui and Leahy, 2010; Quuran and Cheyne, 2010; Kumihashi and Sekihara, 2010).

For complex signals, the mathematical formulation of eDCBF flexibly enables examination of correlations in envelopes and frequency bands of interest without too much additional computational load, thereby permitting a more detailed investigation of neuronal communication. Moreover, the eDCBF correlation analysis can be naturally extended to the MCBF spatial filter to account for the presence of multiple correlated sources.

A variety of simulations were conducted to examine the performance of the eDCBF by quantifying the robustness of computed correlations across a range of SNRs (4 to 0.167), source locations, time lags, and waveform shape for two sources. The eDCBF reconstructed correlations with a high degree of accuracy even at a source spacing of only 5 mm. The results also showed that the eDCBF could handle both fully correlated and uncorrelated neuronal sources. Source time-course reconstructions resulted in accurate and individual time-courses regardless of the degree of correlation between sources. Furthermore, the amplitudes of time courses were accurately reproduced irrespective of the correlation between sources, which is a notable shortcoming of previous dual-beamformer approaches (Brookes et al., 2007; Diwakar and Huang et al., 2011). The spatial width of the eDCBF localization peaks using different measures (Z^K and Z^P) under different SNR conditions

was also investigated. We observed that Z^K provides a suitable width for low SNR data while Z^P is preferable for high SNRs.

As a proof of principle, our investigation of the MCBF spatial filter showed accurate correlation reconstruction across a wide variety of source correlations and SNRs in the presence of three correlated sources. In reality, MEG signals can have many active sources. As such, future developments should include an optimization algorithm to determine the proper MCBF core-number to use for reconstruction, which would prevent inaccurate estimation of source activities due to under-modeling. For example, DCBF localization and pseudo-Z-score statistical thresholding can be used to determine MCBF core-number. Furthermore, typical SNR levels for real recordings must be considered, which limits the MCBF core-size to 8-10 sources in practice.

We also applied the eDCBF spatial filter to human MEG measurements from a stereo auditory tone paradigm to cross-validate reconstruction performance from our simulations. Localization with the power pseudo-Z-score showed activity in both auditory cortices. The SBF and eDCBF reconstructions were compared to a two-dipole-fit reconstruction. The eDCBF time-courses for both right and left hemisphere auditory cortices closely resembled dipole-fit time-courses, maintaining both transient and steady-state components of the signal. In contrast, reconstruction with SBF showed malformed and inaccurate time courses. Source localization with eDCBF was used for SBF reconstruction due to the SBF's inability to properly localize

correlated neuronal sources (Brookes et al., 2007). Inter-hemispheric correlations computed from eDCBF and dipole-fit estimated time-courses were very close; however, the SBF predicted correlation was underestimated, confirming that the eDCBF offers a more robust reconstruction than the SBF in correlated source environments. Furthermore, strong correlation between eDCBF time-courses and dipole-fit results showed that the two methods yield very similar waveforms.

In summary, the present results indicate that the eDCBF spatial filter provides a viable method for exploring complex neuronal networks and their communication, promoting the use of MEG to investigate brain activity.

3.6 Acknowledgments

This work was supported in part by a research grant from the McDonnell Foundation via the Brain Trauma Foundation (PI: J. Ghajar, site PIs: R. Lee and M. Huang); by Department of Veteran Affairs grants to M. Huang (051455 and 060812), R. Lee (E4477-R), and D. Harrington (1IO1CX000146-01 and B501R); by the Office of Naval Research to D. Harrington and T. Liu (N00141010072); and by National Institutes of Health grants to T. Liu (2R01-NS051661), R. Srinivasan (R01-MH068004), and S. Chien (5-T32 HL-7089-35). The authors also thank Jia Guo for helpful suggestions and discussion. In addition, the authors would like to thank the

reviewers for helpful and constructive suggestions that substantially strengthened this work.

Chapter 3, in part, is a reprint of the material as it appears in NeuroImage 56, pp. 1918-1928, 2011. Diwakar, Mithun; Tal, Omer; Liu, Thomas T.; Harrington, Deborah L.; Srinivasan, Ramesh; Muzzatti, Laura; Song, Tao; Theilmann, Rebecca J.; Lee, Roland R.; Huang, Ming-Xiong. The dissertation author was co-first author of this publication.

Table 3.1: Estimated correlation reconstruction for auditory dipoles (SNR=4). Correlation averages and standard deviations determined using 1000 Monte Carlo simulations.

θ Shift	χ (Actual)	χ (Estimated)	σ
0°	1.000	0.997	3.83E-05
10°	0.970	0.967	1.96E-04
20°	0.883	0.881	4.44E-04
30°	0.750	0.748	7.96E-04
40°	0.587	0.585	1.03E-03
50°	0.413	0.412	1.22E-03
60°	0.250	0.250	1.21E-03
70°	0.117	0.117	9.85E-04
80°	0.030	0.030	5.47E-04
90°	0.000	0.000	1.07E-04

Table 3.2: Amplitude values for left auditory cortex dipole (results equivalent for right dipole). Amplitude values determined using 100 Monte Carlo simulations.

θ Shift	χ (Actual)	SNR				
		4	2	1	0.5	0.25
		Amplitude				
0°	1.000	4.99	4.99	4.99	4.99	4.99
10°	0.970	4.99	5.00	4.99	4.99	4.99
20°	0.883	4.99	4.99	5.00	4.99	4.99
30°	0.750	4.99	5.00	5.00	4.99	4.99
40°	0.587	4.99	4.99	4.99	4.99	4.99
50°	0.413	4.99	4.99	5.00	4.99	4.99
60°	0.250	4.99	4.99	5.00	4.99	4.98
70°	0.117	4.99	5.00	4.99	4.99	4.98
80°	0.030	4.99	4.99	4.99	4.99	4.97
90°	0.000	4.99	4.99	4.99	4.99	4.93

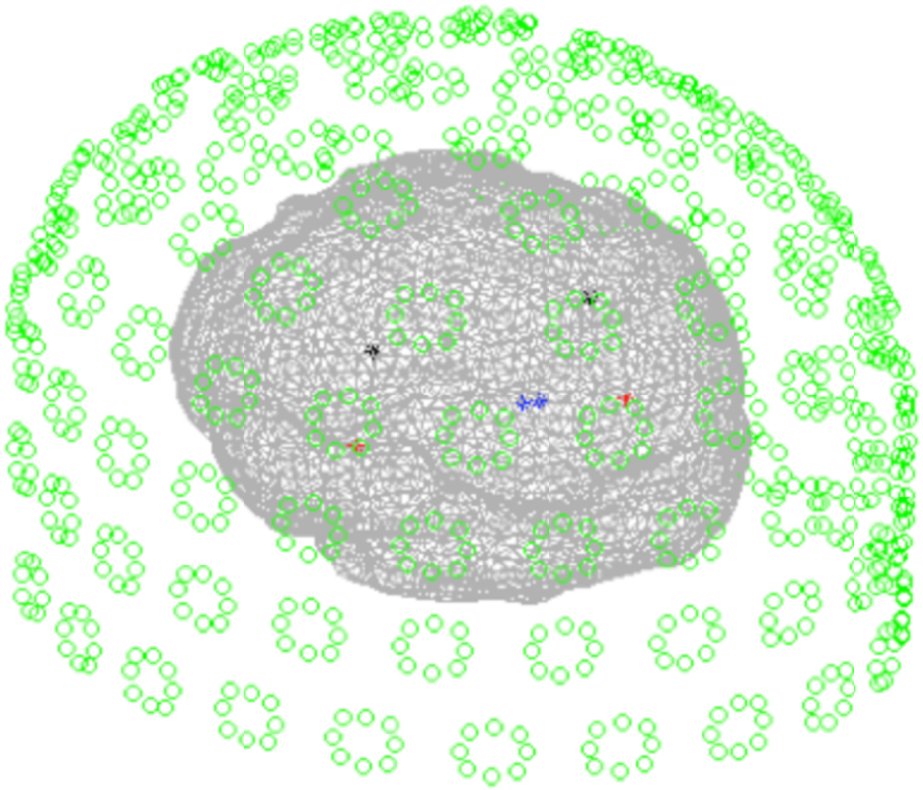

Figure 3.1: Source and Sensor Model. Green – MEG sensor groups. Blue – Posterior Cingulate Cortex dipoles. Black – Motor Cortex dipoles. Red – Auditory Cortex dipoles.

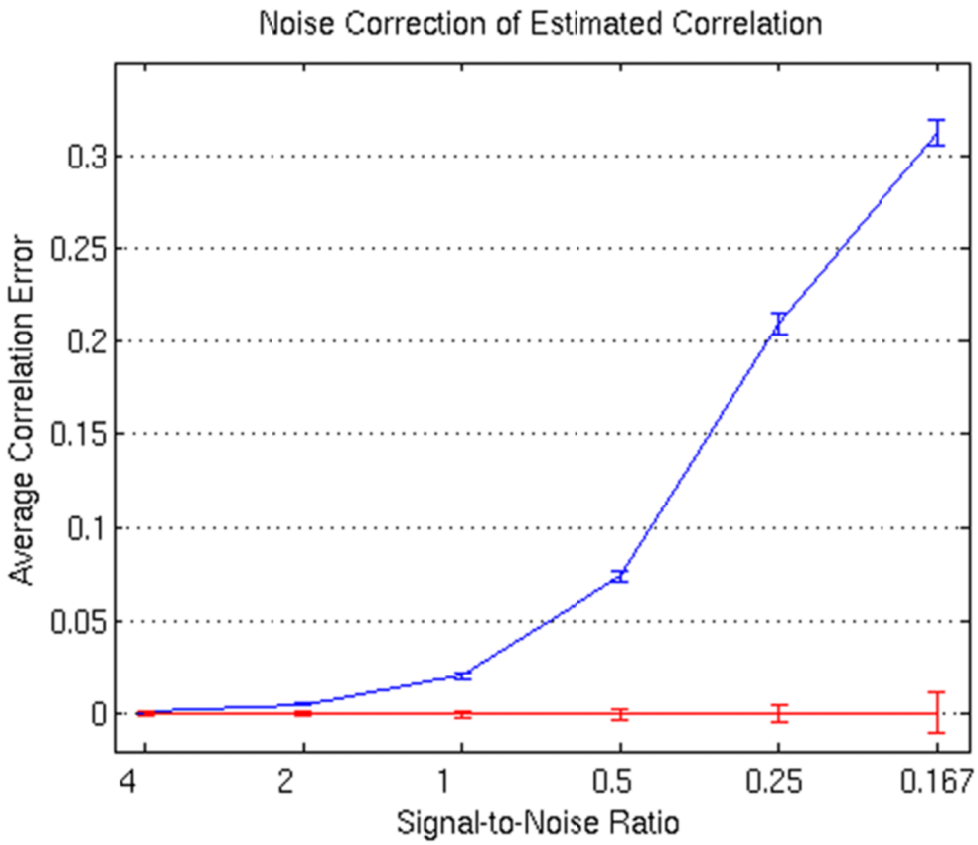

Figure 3.2: Estimated (blue) and Noise-corrected (red) correlation reconstruction errors and standard deviations (error bars) for auditory dipoles. Correlation values determined using 1000 Monte Carlo simulations.

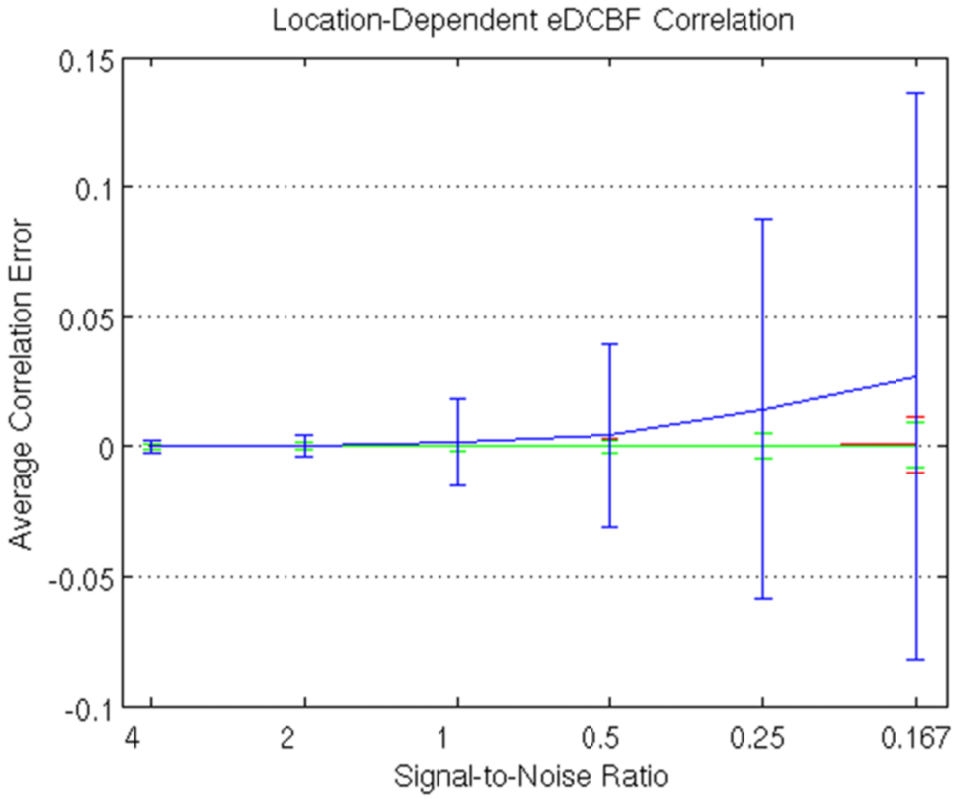

Figure 3.3: Noise-corrected correlation reconstruction errors and standard deviations (error bars) for auditory cortex (red), motor cortex (green), and posterior cingulate cortex (blue) dipoles. Correlation values determined using 1000 Monte Carlo simulations.

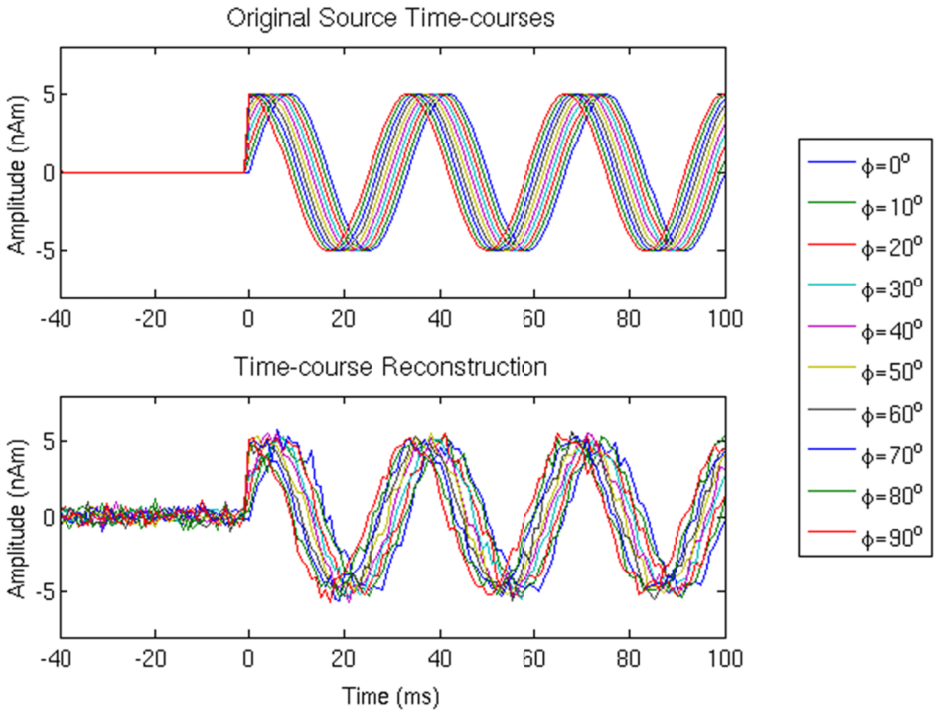

Figure 3.4: Sinusoidal Time-course Reconstruction at phase shifts ranging from 0 to 90 degrees. Top panel – simulated source waveforms. Bottom panel – eDCBF time-courses.

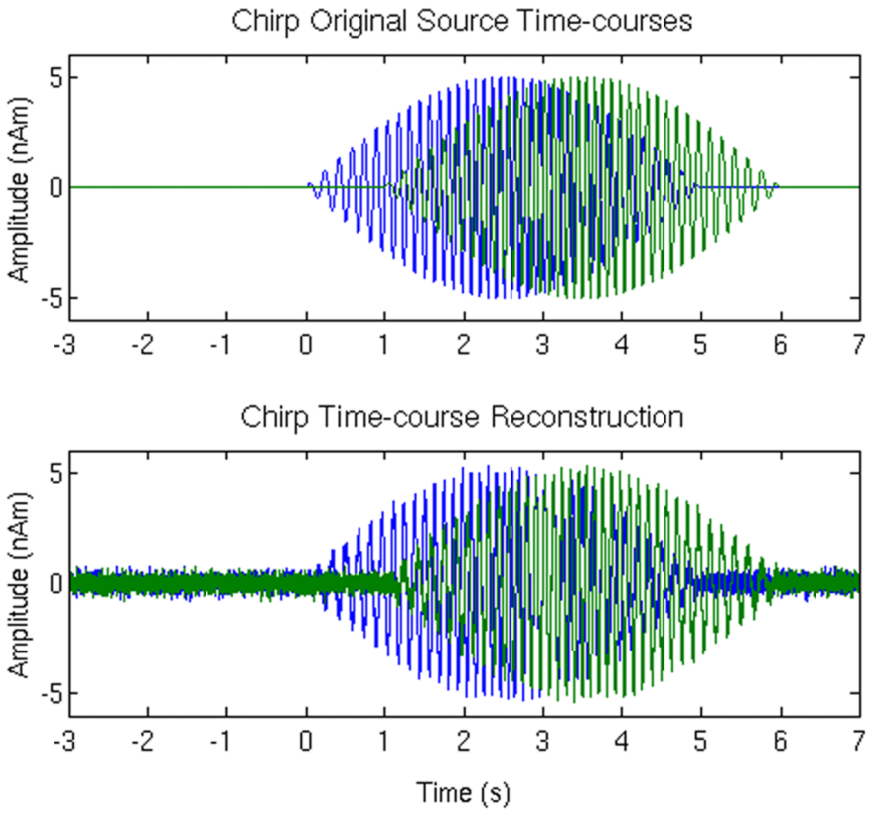

Figure 3.5: Chirp Time-course Reconstruction at 1 second time lag. Top panel – original source waveforms. Bottom panel – eDCBF time-courses. Blue – left auditory cortex. Green – right auditory cortex.

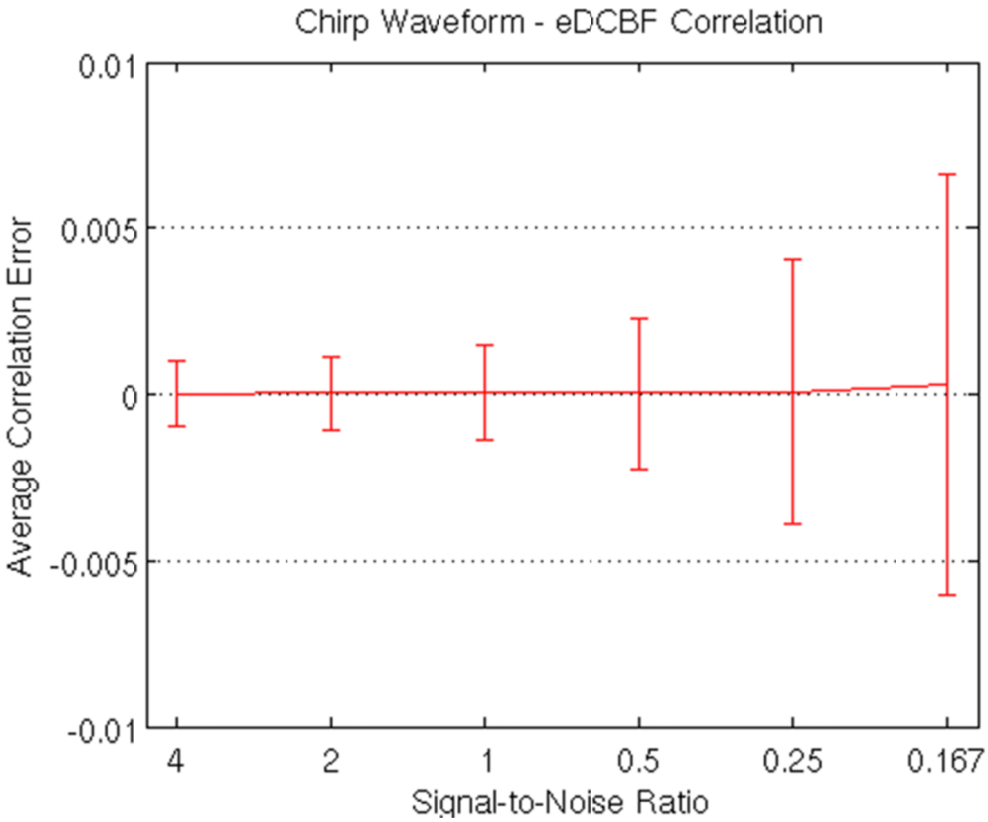

Figure 3.6: Noise-corrected correlation reconstruction errors and standard deviations (error bars) for chirp waveforms at different time-lags. Correlation values determined using 1000 Monte Carlo simulations.

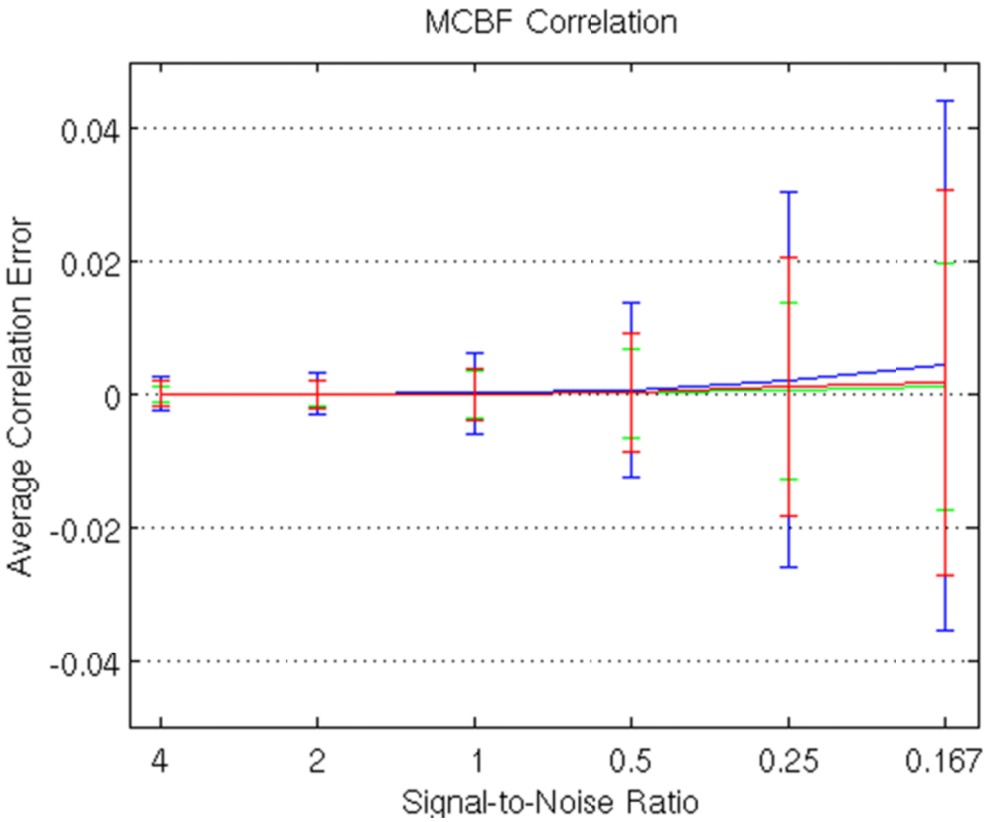

Figure 3.7: Pair-wise three-core MCBF noise-corrected correlation reconstruction errors and standard deviations (error bars). Blue – left motor cortex and posterior cingulate cortex. Green – left motor cortex and right motor cortex. Red – right motor cortex and posterior cingulate cortex. Correlation values determined using 1000 Monte Carlo simulations.

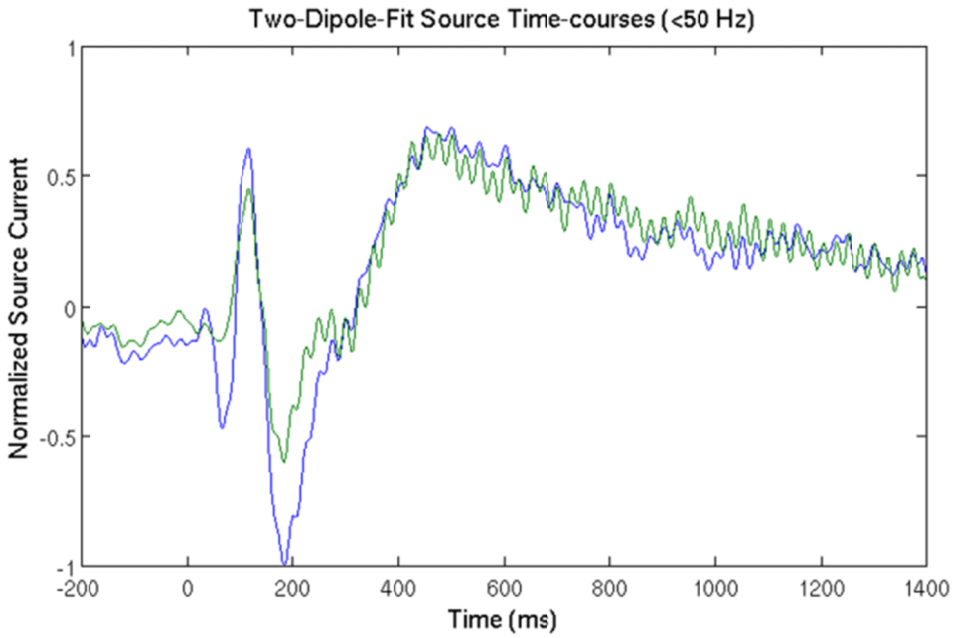

Figure 3.8: Normalized dipole-fit source time-course reconstruction. Reconstruction of time courses shows a transient and steady-state response in both left (blue) and right (green) auditory cortices. The left transient response is higher in amplitude, while the right 40-Hz steady-state oscillations are more pronounced.

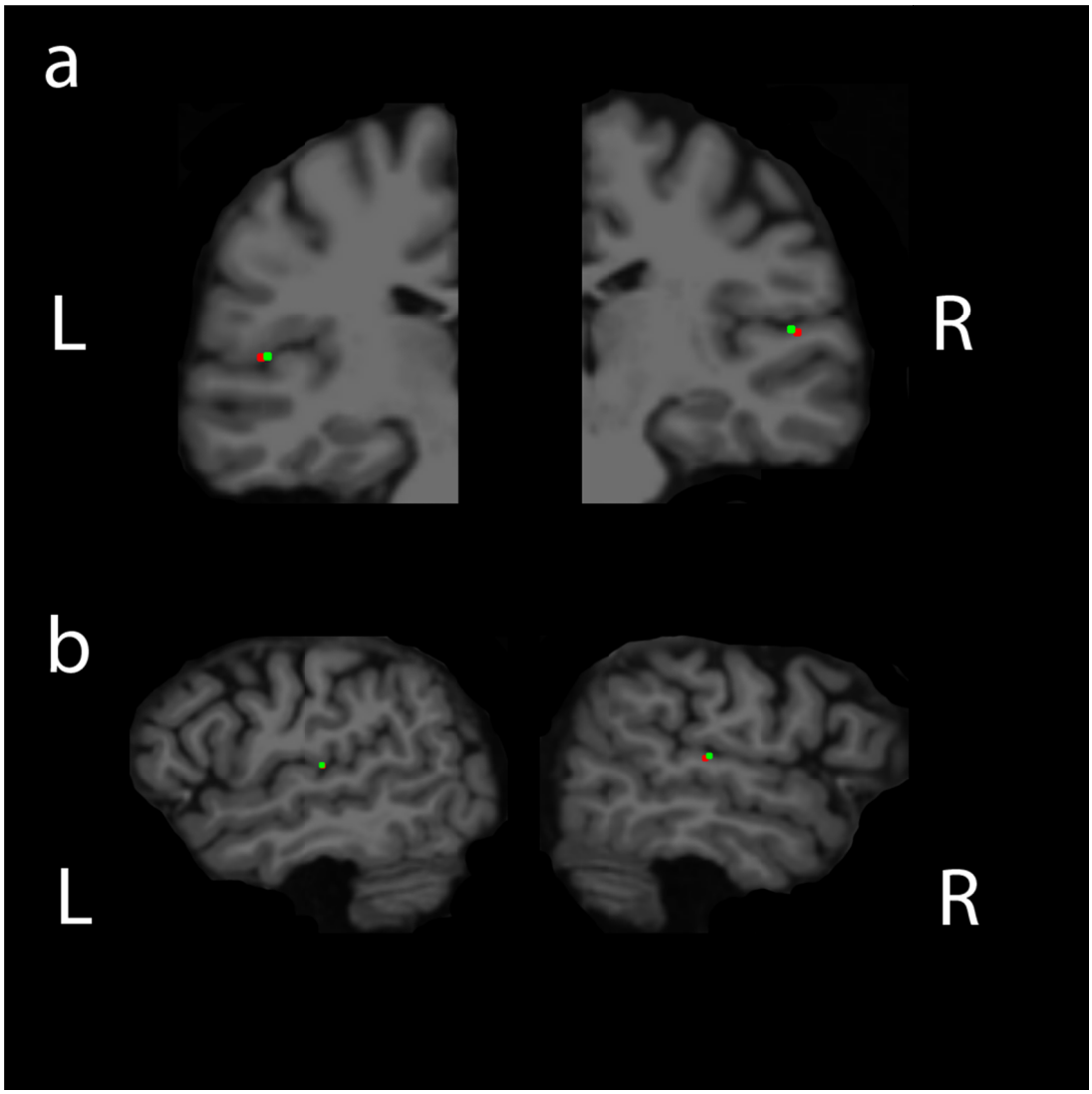

Figure 3.9: a) Coronal view of left and right auditory response localization. b) Sagittal view of left and right auditory response localization. Green – eDCBF localization. Red – dipole-fit localization.

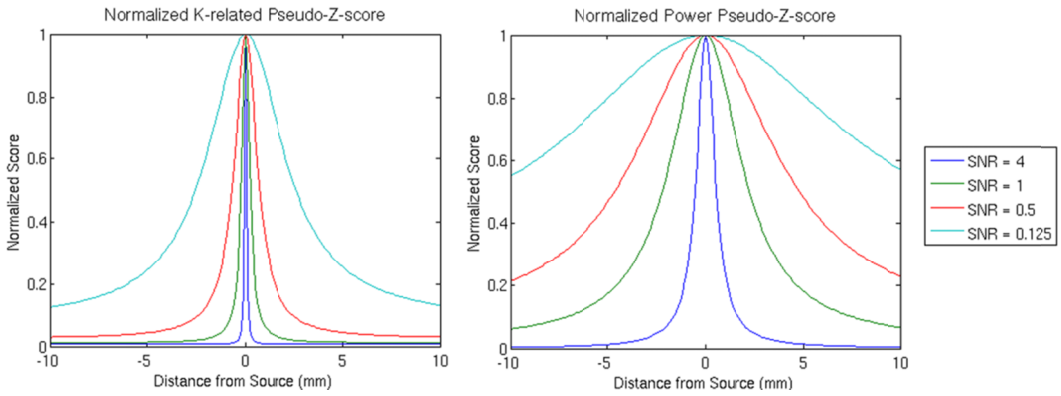

Figure 3.10: SNR dependence of pseudo-Z-scores. Left Panel – The K-related pseudo-Z-score peaks sharply at high SNR but provides a reasonable profile for localization at lower SNR. Right Panel - The power pseudo-Z-score has much broader peaks, providing an appropriate tool for localization in evoked recordings.

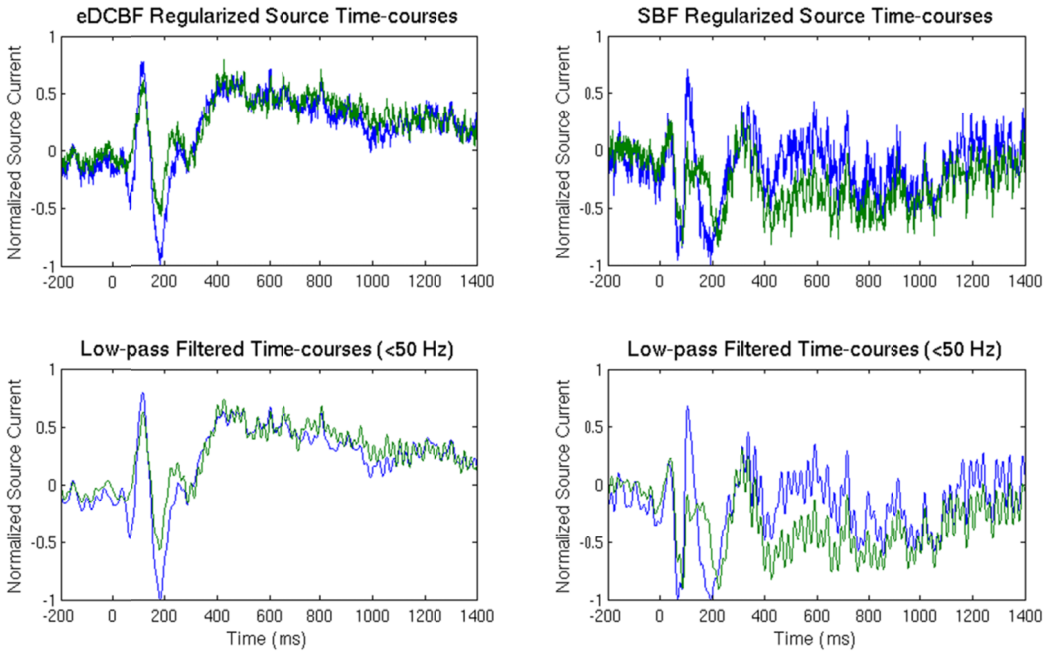

Figure 3.11: Normalized eDCBF and SBF source time-course reconstruction. eDCBF reconstruction of time courses shows a transient and steady-state response in both left (blue) and right (green) auditory cortices. The left transient response was higher in amplitude while the right steady-state response was more visible. SBF reconstruction of time courses shows distortion and features that are difficult to identify.

3.7 References

Brookes, M.J., Stevenson, C.M., Barnes, G.R., Hillebrand, A., Simpson, M.I.G., Francis, S.T., Morris, P.G., 2007. Beamformer reconstruction of correlated sources using a modified source model. NeuroImage 34, 1454-1465.

Dalal, S.S., Sekihara, K., Nagarajan, S.S., 2006.Modified Beamformers for Coherent Source Region Suppression. IEEE Trans. Biomed. Eng. 53, 1357-1363.

Dale, A.M., Fischl, B., Sereno, M.I., 1999. Cortical surface-based analysis: I. Segmentation and surface reconstruction. NeuroImage 9, 179-194.

Diwakar, M., Huang, M.X., Srinivasan, R., Harrington, D.L., Robb, A., Angeles, A., Muzzatti, L., Pakdaman, R., Song., T., Theilmann, R.J., Lee, R.R., 2011. Dual-Core Beamformer for obtaining highly correlated neuronal networks in MEG. NeuroImage 54, 253-263.

Fischl, B., van der, K.A., Destrieux, C., Halgren, E., Segonne, F., Salat,D.H., Busa, E., Seidman, L.J., Goldstein, J., Kennedy, D., Caviness, V.,Makris, N., Rosen, B., Dale, A.M., 2004. Automatically parcellating the human cerebral cortex. Cereb. Cortex 14, 11-22.

Hamalainen, M.S., Ilmoniemi, R.J., 1994. Interpreting magnetic fields of the brain: minimum norm estimates. Med. Biol. Eng. Comput. 32, 35-42.

Hillebrand, A., Singh, K.D., Holliday, I.E., Furlong, P.L., Barnes, G.R., 2005. A new approach to neuroimaging with Magnetoencephalography. Hum. Brain Mapp. 25, 199-211.

Huang, M., Aine, C.J., Supek, S., Best, E., Ranken, D., Flynn, E.R., 1998. Multistart downhill simplex method for spatio-temporal source localization in magnetoencephalography. Electroencephalogr. Clin. Neurophysiol. 108, 32-44.

Huang, M., Dale, A.M., Song, T., Halgren, E., Harrington, D.L., Podgorny, I., Canive, J.M., Lewis, S., Lee, R.R., 2006. Vector-based spatial-temporal minimum L1-norm solution for MEG. NeuroImage 31, 1025-1037.

Hui, H.B., Leahy, R.M., 2006. Linearly constrained MEG beamformers for MVAR modeling of cortical interactions. 3rd IEEE International Symposium on Biomedical Imaging: Nano to Macro, 2006, pp. 237–240.

Hui, H.B., Pantazis, D., Bressler, S.L., Leahy, R.M., 2010. Identifying true cortical interactions in MEG using the nulling beamformer. NeuroImage 49, 3161-3174.

Kumihashi, I., Sekihara, K., 2010. Array-gain constraint minimum-norm spatial filter with recursively updated gram matrix for biomagnetic source imaging. IEEE Trans. Biomed. Eng. 57, 1358-1365.

Mosher, J.C., Baillet, S., Leahy, R.M., 1999. EEG source localization and imaging using multiple signal classification approaches. J. Clin. Neurophsiol. 16, 255-238.

Mosher, J.C., Leahy, R.M., 1998. Recursive MUSIC: a framework for EEG and MEG source localization. IEEE Trans. Biomed. Eng. 45, 1342-1354.

Mosher, J.C., Lewis, P.S., Leahy, R.M., 1992. Multiple dipole modeling and localization from spatio-temporal MEG data. IEEE Trans. Biomed. Eng. 39, 541-557.

Quuran, M.A., Cheyne, D., 2010. Reconstruction of correlated brain activity with adaptive spatial filters in MEG. NeuroImage 49, 2387-2400.

Robinson, S., Vrba, J., 1998.Functional neuroimaging by synthetic aperture magnetometry. In: Yoshimoto, T., Kotani, M., Kuriki, S., Karibe, H., Nakasato, N. (Eds.), Recent Advances in Biomagnetism. Tohoku Univ. Press, Sendai, pp. 302-305.

Sekihara, K., Nagarajan, S., Poeppel, D., Marantz, A., 2002. Performance of an MEG adaptive-beamformer technique in the presence of correlated neural activities: effects on signal intensity and time course estimates. IEEE Trans. Biomed. Eng. 49 (12), 1534-1546.

Sekihara, K., Nagarajan, S., Poeppel, D., Marantz, A., 2004. Asymptotic SNR of scalar and vector minimum-variance beamformers for neuromagnetic source reconstruction. IEEE Trans. Biomed.Eng. 51 (10), 1726-1733.

Song, T., Cui, L., Gaa, K., Feffer, L., Taulu, S., Lee, R.R., Huang, M.X., 2009. Signal Space Separation Algorithm and Its Application on Suppressing Artifacts Caused by Vagus Nerve Stimulation for Magnetoencephalography Recordings. J. Clin. Neurophysiol. 26 (6), 392-400.

Song, T., Gaa, K., Cui, L., Feffer, L., Lee, R.R., Huang, M.X., 2008.Evaluation of signal space separation via simulation. Med. Biol. Eng. Comput. 46, 923-932.

Spencer, M.E., Leahy, R.M., Mosher, J.C., Lewis, P.S., 1992. Adaptive filters for monitoring localized brain activity from surface potential time series. Conf. Record for 26th Annu.Asilomer Conf. Signals, Systems, and Computers.156-161.

Taulu, S., Kajola, M., Simola, J., 2004. Suppression of interference and artifacts by the signal space separation method. Brain Topogr. 16, 269-275.

Taulu, S., Simola, J., 2006.Spatiotemporal signal space separation method for rejecting nearby interference in MEG measurements. Phys. Med. Biol. 51, 1759-1768.

Van Drongelen, W., Yuchtman, M., Van Veen, B.D., Van Huffelen, A.C., 1996. A spatial filtering technique to detect and localize multiple sources in the brain. Brain Topogr. 9 (1), 39-49.

Van Veen, B.D., Van Drognelen, W., Yuchtman, M., Suzuku, A., 1997. Localisation of brain electrical activity via linearly constrained minimum variance spatial filtering. IEEE Trans. Biomed. Eng. 44 (9).

Vrba, J., Robinson, S.E., 2001. Signal processing in magnetoencephalography. Methods 25 (2), 249-271.

CHAPTER 4

An Algorithm for Neuronal Source Localization using the Multi-core Beamformer in MEG Recordings

4.1 Abstract

In this chapter, we introduce a method that incorporates the multi-core beamformer (MCBF) to perform successful source activity reconstruction for biomagnetic measurements recorded by magnetoencephalography (MEG). Beamformers have been widely used for determining source activity in MEG applications but have limitations. Notably, conventional single beamformers (SBF) have difficulty detecting neuronal sources with correlated time-courses, causing correlation-dependent time-course distortion and amplitude suppression. The MCBF, while able to handle multiple correlated sources and overcoming many limitations of the conventional dual-source beamformer, is more challenging to use than the SBF as it requires searching for optimum solutions and, as formulated, only determines activity for locations specified by the cores. In our method, we introduce a way of efficiently and reliably searching the source space for the optimum MCBF solution without *a priori* information, thereby preventing the distortion common with conventional beamformers while arriving at a solution in a reasonable time-frame. Furthermore, we show that time-course estimates can be found for the entire source space, a feature lacking in prior multi-source beamformer formulations.

We have validated and demonstrated the success of our approach through application to simulated data as well as to evoked median-nerve stimulation MEG data.

4.2 Introduction

Due to the underdetermined nature of the lead-field type of inverse problem, different techniques have been proposed as a means of generating viable solutions. However, none can address all characteristics of complex brain activity in a practical manner for all cases. In this chapter, we put forward a novel source localization technique, which employs the abilities of the multi-core beamformer (MCBF) to overcome the inherent limitations of previous single and multi-source adaptive spatial filters (beamformers).

The most frequently used beamformer to obtain a solution to the inverse problem is the single beamformer filter (SBF). The minimum-variance constraint used by the SBF incorporates the sensor covariance matrix, allowing it to attain very high spatial resolution for uncorrelated source reconstructions (Robinson and Vrba, 1998; Sekihara et al., 2002; Van Drongelen et al., 1996; Van Veen et al., 1997). However, this beamformer fails to resolve coherent sources, leading to the suppression of source amplitudes and distorted time-courses (Sekihara and Nagarajan, 2008). In addition, although the SBF is capable of generating time-courses and power estimates on a voxel-by-voxel basis, neural activity generally involves synchronous

communication between multiple sources (Singer, 1999), rendering the SBF inadequate for analyzing high-level brain activity.

To address these shortcomings, the enhanced dual-core beamformer (eDCBF) was developed, allowing accurate determination of unique source time-courses (i.e. allowing coherence analysis) and source amplitudes (Diwakar et al., 2011b). Reconstructions of auditory evoked recordings with the eDCBF showed its capability to produce high-fidelity solutions with real data. To deal with data containing more than two coherent sources, an extension of the eDCBF, dubbed the multi-core beamformer (MCBF), was introduced. Though the MCBF offers many advantages over other beamformers, source localization is difficult, requiring multi-dimensional searches. Furthermore, time-courses are only generated for the sources included in the spatial filter and not for other locations in the brain, preventing whole-brain connectivity studies.

In this chapter, we introduce a novel MCBF localization search algorithm that finds feasible solutions in the timescale of minutes with no *a priori* information required. The algorithm exploits under-modeled solutions to gradually increase the MCBF core size until the correct number of sources is modeled. The search algorithm operates by using a newly developed pseudo-Z-score statistic that describes total source-by-source signal-to-noise ratio (SNR). We further demonstrate that over-modeled and under-modeled solutions can be detected so that the optimum MCBF core number can be

determined. By exploring the parallels between the MCBF and the nulling beamformer, we also demonstrate MCBF's ability to generate volumetric source time-courses and whole-brain power maps that can be used for investigation of brain coherence. MCBF reconstructions as well as the proposed source localization algorithm were tested with complex six-dipole simulations and with real neuromagnetic measurements recorded during a median-nerve stimulation task, showcasing MCBF's ability to accurately determine source activity for highly complex neuronal networks.

4.3 Materials and Methods

In this section, we first review MCBF mathematics, after which we develop the new metric and methodology used to obtain the optimum source solution as well as describe the generation of volumetric activity maps. Finally, we describe the simulated and median-nerve stimulation experiments used to test our proposed search algorithm and quality of maps created.

4.3.1 Multi-core Beamformer

To develop a suitable multi-dimensional search statistic and search algorithm, we begin by exploring the mathematical description of the MCBF. The multi-core lead-field vector is defined as the *m x 2c* matrix $\boldsymbol{L}_m = [\boldsymbol{L}_1 \quad \boldsymbol{L}_2 \quad \cdots \quad \boldsymbol{L}_c]$, where *c* is the desired number of sources to be modeled. The corresponding multi-core weighting vector is defined as the *m x 2c* matrix $\boldsymbol{W}_m = [\boldsymbol{W}_1 \quad \boldsymbol{W}_2 \quad \cdots \quad \boldsymbol{W}_c]$, designed such that:

$$\hat{\boldsymbol{s}}(t) = \boldsymbol{W}_m^T \boldsymbol{b}(t) \tag{4.1}$$

where $\hat{\boldsymbol{s}}(t)$ represents the estimated source time-courses. The solution to the multi-core weighting vector, $\boldsymbol{W}_m$, is obtained by computing the minimum variance solution (Diwakar et al., 2011b):

$$\boldsymbol{W}_m = \boldsymbol{R}_b^{-1} \boldsymbol{L}_m (\boldsymbol{L}_m^T \boldsymbol{R}_b^{-1} \boldsymbol{L}_m)^{-1} \tag{4.2}$$

To prevent erroneous weighting near the center of the head, array-gain constraints may be applied by normalizing each column of $\boldsymbol{L}_m$ (Kumihashi and Sekihara, 2010; Sekihara and Nagarajan, 2008). The MCBF estimated vector covariance matrix $\boldsymbol{R}_{\hat{s}}$ is then given by:

$$\boldsymbol{R}_{\hat{s}} = \boldsymbol{W}_m^T \boldsymbol{R}_b \boldsymbol{W}_m = (\boldsymbol{L}_m^T \boldsymbol{R}_b^{-1} \boldsymbol{L}_m)^{-1} \tag{4.3}$$

The MCBF estimated source vector covariance matrix $\boldsymbol{R}_{\hat{s}}$ can be expressed as:

$$\boldsymbol{R}_{\hat{s}} = \begin{pmatrix} \langle \hat{s}_1(t)\hat{s}_1(t) \rangle \overline{\boldsymbol{\eta}}_1 \overline{\boldsymbol{\eta}}_1^T & \langle \hat{s}_1(t)\hat{s}_2(t) \rangle \overline{\boldsymbol{\eta}}_1 \overline{\boldsymbol{\eta}}_2^T & \cdots & \langle \hat{s}_1(t)\hat{s}_c(t) \rangle \overline{\boldsymbol{\eta}}_1 \overline{\boldsymbol{\eta}}_c^T \\ \langle \hat{s}_2(t)\hat{s}_1(t) \rangle \overline{\boldsymbol{\eta}}_2 \overline{\boldsymbol{\eta}}_1^T & \langle \hat{s}_2(t)\hat{s}_2(t) \rangle \overline{\boldsymbol{\eta}}_2 \overline{\boldsymbol{\eta}}_2^T & \cdots & \langle \hat{s}_2(t)\hat{s}_c(t) \rangle \overline{\boldsymbol{\eta}}_2 \overline{\boldsymbol{\eta}}_c^T \\ \vdots & \vdots & \ddots & \vdots \\ \langle \hat{s}_c(t)\hat{s}_1(t) \rangle \overline{\boldsymbol{\eta}}_c \overline{\boldsymbol{\eta}}_1^T & \langle \hat{s}_c(t)\hat{s}_2(t) \rangle \overline{\boldsymbol{\eta}}_c \overline{\boldsymbol{\eta}}_2^T & \cdots & \langle \hat{s}_c(t)\hat{s}_c(t) \rangle \overline{\boldsymbol{\eta}}_c \overline{\boldsymbol{\eta}}_c^T \end{pmatrix} \tag{4.4}$$

where $\hat{s}_i(t)$ are the estimated scalar source time-courses and $\overline{\boldsymbol{\eta}}_i$ are the *2 x 1* estimated normalized orientations. The diagonal *2 x 2* sub-matrices of $\boldsymbol{R}_{\hat{s}}$ are of the same form as SBF vector covariance matrices (Sekihara et al., 2004). Thus, source power estimates can be obtained by simply computing the trace

of the respective diagonal submatrix (Diwakar et al., 2011b). An equivalent covariance matrix for source noise $\boldsymbol{R}_{\hat{n}}$ can be expressed as:

$$\boldsymbol{R}_{\hat{n}} = \boldsymbol{W}_m^T \boldsymbol{R}_n \boldsymbol{W}_m$$

$$= \begin{pmatrix} \langle \hat{n}_1(t)\hat{n}_1(t)\rangle \bar{\boldsymbol{\zeta}}_1 \bar{\boldsymbol{\zeta}}_1^T & \langle \hat{n}_1(t)\hat{n}_2(t)\rangle \bar{\boldsymbol{\zeta}}_1 \bar{\boldsymbol{\zeta}}_2^T & \cdots & \langle \hat{n}_1(t)\hat{n}_c(t)\rangle \bar{\boldsymbol{\zeta}}_1 \bar{\boldsymbol{\zeta}}_c^T \\ \langle \hat{n}_2(t)\hat{n}_1(t)\rangle \bar{\boldsymbol{\zeta}}_2 \bar{\boldsymbol{\zeta}}_1^T & \langle \hat{n}_2(t)\hat{n}_2(t)\rangle \bar{\boldsymbol{\zeta}}_2 \bar{\boldsymbol{\zeta}}_2^T & \cdots & \langle \hat{n}_2(t)\hat{n}_c(t)\rangle \bar{\boldsymbol{\zeta}}_2 \bar{\boldsymbol{\zeta}}_c^T \\ \vdots & \vdots & \ddots & \vdots \\ \langle \hat{n}_c(t)\hat{n}_1(t)\rangle \bar{\boldsymbol{\zeta}}_c \bar{\boldsymbol{\zeta}}_1^T & \langle \hat{n}_c(t)\hat{n}_2(t)\rangle \bar{\boldsymbol{\zeta}}_c \bar{\boldsymbol{\zeta}}_2^T & \cdots & \langle \hat{n}_c(t)\hat{n}_c(t)\rangle \bar{\boldsymbol{\zeta}}_c \bar{\boldsymbol{\zeta}}_c^T \end{pmatrix} \quad (4.5)$$

where $\hat{n}_i(t)$ are the estimated scalar source noise time-courses and $\bar{\boldsymbol{\zeta}}_i$ are the *2 x 1* estimated normalized noise orientations. In a similar manner, source noise estimates can be computed as the trace of each submatrix of $\boldsymbol{R}_{\hat{n}}$. The signal-to-noise ratio of each source can then be determined by:

$$Z_i = \frac{tr(\langle \hat{s}_i(t)\hat{s}_i(t)\rangle \bar{\boldsymbol{\eta}}_i \bar{\boldsymbol{\eta}}_i^T) - tr(\langle \hat{n}_i(t)\hat{n}_i(t)\rangle \bar{\boldsymbol{\zeta}}_i \bar{\boldsymbol{\zeta}}_i^T)}{tr(\langle \hat{n}_i(t)\hat{n}_i(t)\rangle \bar{\boldsymbol{\zeta}}_i \bar{\boldsymbol{\zeta}}_i^T)}$$

$$= \frac{tr(\langle \hat{s}_i(t)\hat{s}_i(t)\rangle \bar{\boldsymbol{\eta}}_i \bar{\boldsymbol{\eta}}_i^T)}{tr(\langle \hat{n}_i(t)\hat{n}_i(t)\rangle \bar{\boldsymbol{\zeta}}_i \bar{\boldsymbol{\zeta}}_i^T)} - 1 \quad (4.6)$$

In practice, the submatrices of $\boldsymbol{R}_{\hat{s}}$ and $\boldsymbol{R}_{\hat{n}}$ are sufficient to compute individual source pseudo-Z-scores, and it is not necessary to determine individual source powers and orientations. Such a pseudo-Z-score has been shown to be robust to variations in the lead-fields, providing a useful statistic to model source activity (Sekihara et al., 2002; Sekihara et al., 2004; Van Veen et al., 1997). Therefore, we use the pseudo-Z-score to guide MCBF localization, assuming that the optimum solution is attained when the sum of all individual pseudo-Z-scores (Z_t) is maximized.

$$Z_t = \sum Z_i \tag{4.7}$$

4.3.2 Algorithm for Maximizing Z_t

The sum of Z-scores (Z_t) is a function of all core locations. A typical source grid that is used for inverse MEG solution computation contains approximately 7000-9000 sources. While performing exhaustive enumeration of all possible values of Z_t would yield the optimum MCBF solution, this becomes computationally impractical as the MCBF core increases in size. Therefore, a non-linear search algorithm was developed capable of finding an adequate solution within a reasonable timeframe (Figure 4.1). As a starting point for modeling the core, the algorithm employs the two-source MCBF solution. This solution is obtained by performing Powell searches with randomly selected dipole pairs to find the pair with the highest Z_t, similar to the DCBF approach previously documented (Diwakar et al., 2011a), with search distance limited to a 3 cm radius. Next, the two main stages of the search algorithm, (1) core development and (2) core refinement, are performed until Z_t stabilizes. Core development is accomplished by adding a new source, satisfying a minimum SNR ($Z_i > 0.05$) and chosen from the global dipole grid, to the existing core that maximizes the total pseudo-Z-scores of all cores (Z_t). During core refinement, each source in the core is locally adjusted within a radius of 3 cm such that Z_t is maximized. The cores are sequentially adjusted (in order of highest to lowest single source pseudo-Z-score (Z_i)) in each

iteration of the core refinement stage. Core refinement is completed once no more adjustments are made, i.e. a stable core configuration is found.

Core development halts when Z_t remains stable or reaches a plateau (i.e. $|Z_t - Z_{old}| < \varepsilon$ repeatedly, where ε is 1% of Z_{old}). If a stable plateau is not achieved, a maximum core size should be used as a stopping criterion. Given that typical MEG recordings contain 40-50 independent modes and each core is described by a rank 2 lead-field matrix (i.e. DoF =2), the MCBF can support approximately 20-25 cores per covariance matrix before matrix inversion becomes unstable. A lower maximum core size may be used to decrease computational cost. However, one should ensure that the maximum core size is not set too low, so that enough data points may be collected to sufficiently account for all sources present.

4.3.3 Generation of Volumetric Activity Maps

Mathematically, the cores present in the MCBF core-set act in the same fashion as nulling constraints imposed using the nulling beamformer (Dalal et al., 2006; Diwakar et al., 2011b; Hui and Leahy, 2006; Hui and Leahy, 2010; Quuran and Cheyne, 2010), except they are determined without the use of prior information. For each given source (core) a respective volumetric power map (pseudo-Z-score per grid point) and time-course map (time-course per grid point) can be computed. This is done by using all the remaining cores in the weight vector solution with an additional “free” core (beamformer pointing

location) that scans through every grid point to calculate the corresponding pseudo-Z-score and time-course. Map construction is mathematically identical to applying *c - 1* nulling constraints with the NB. Repeating this process for each core results in a total of *c* source power and *c* source time-course maps (i.e. applying single NB *c* times with *c - 1* constraints). The individual source power maps may then be combined to form a collective power map by taking, for each grid point, the largest pseudo-Z-score across all individual maps. In a similar manner, a collective time-course map can be generated; the time-course is chosen for each grid point from the time-course map corresponding to the core whose power map resulted in the largest pseudo-Z-score at that grid point.

This method of combining individual maps ensures that the collective power and time-course maps reflect the combination of nulling constraints yielding the highest source-space SNR at each grid point. Furthermore, individual power maps have little spatial overlap of source-containing regions, ensuring that collective time-courses in a local patch of activity all arise from the same set of nulling constraints. In order to provide a quantitative measure for thresholding power and time-course maps, a continuous estimation of the distribution of pseudo-Z-scores across the source grid can be constructed with kernel-smoothing density estimation of the collective power map pseudo-Z-scores. P-values for pseudo-Z-scores are then obtained by integration of this continuous distribution.

4.3.4 General Setup for Simulations

The source space was simulated with a grid covering the cortical gray matter with 7 mm spacing. The cortical boundaries were obtained from a healthy subject's T1-weighted anatomical MRI and subsequent Freesurfer segmentation (Dale et al., 1999; Fischl et al., 2004). The sensor configuration was based on the Elekta/Neuromag^{TM} whole-head MEG system (VectorView), in which 306 sensors are arranged on a helmet-shaped surface (204 gradiometers and 102 magnetometers).

To compute the forward model, the boundary element method (BEM) was employed where the inner-skull surface (from MRI) was used to generate a BEM mesh (size 5mm) (Huang et al., 2007; Mosher et al., 1999). SNR levels were adjusted by adding uncorrelated random Gaussian noise to the sensor waveforms, where the SNR was defined as the ratio of the Frobenius norm of the signal vector to that of the noise vector calculated over the interval with signal.

4.3.5 Six Dipole Simulation (3 highly-correlated networks)

To test the ability of the MCBF localization algorithm to correctly identify sources in a highly correlated environment, three distinct pairs of correlated sources were simulated. The pairs were placed in the left and right hemisphere auditory, motor, and posterior parietal cortices (Figure 4.2).

Each pair of signals was composed of a 6-second inactive period followed by 6 seconds of a sinusoidal wave. The auditory cortex pair was simulated with amplitude of 8 nAm and frequency of 25 Hz (sampling rate 1000 Hz); the motor cortex pair was simulated with amplitude of 10 nAm and frequency of 35 Hz; and the posterior parietal cortex pair was simulated with amplitude of 9 nAm and frequency of 45 Hz. The phase shift of the second source in each pair was set at 10° to produce a correlation of 0.97 within pairs (during the active portion of the waveforms), creating in total three independent highly-correlated inter-hemispheric networks. The simulated sensor waveform was computed using the BEM forward model. Random Gaussian noise was added to set the sensor space SNR at 4. An estimate of $\boldsymbol{R}_b$ from gradiometers only was computed from the six-second active period, while an estimate of $\boldsymbol{R}_n$ was obtained from the inactive period. Localization was performed with the MCBF search algorithm. Time-courses were low-pass filtered at 100 Hz with a 10 Hz transition width to remove high-frequency noise. Fourier transform amplitude values for reconstructed time-courses and simulated time-courses were also compared as a measure of reconstructed source strength reliability (Diwakar et al., 2011b). MCBF time-courses and power maps were compared against a SBF reconstruction of the same data set.

4.3.6 Six Dipole Simulation (2 partially-correlated networks)

MCBF localization was tested further in a highly intricate environment: correlated sources were more closely spaced; more sources were placed within each correlated network; and varying degrees of correlation were simulated within networks. We constructed two source networks, each composed of three partially correlated intra-hemispheric sources. The six dipoles were placed in the same locations as in the previous simulation (Figure 4.2). Each signal was composed of a 6-second inactive period followed by 6 seconds of a sinusoidal wave. To create two partially correlated intra-hemispheric networks while ensuring no inter-hemispheric correlation, the left hemisphere sources were given a frequency of 30 Hz and the right hemisphere sources were set at 40 Hz. The auditory cortex sources were simulated with amplitude of 8 nAm and 0° phase shift, while the motor cortex sources were set at amplitude 10 nAm and 15° phase shift (0.97 correlation to auditory dipoles), and the parietal sources had amplitude 9 nAm and 75° phase shift (0.26 correlation to auditory dipoles and 0.50 to motor dipoles). Forward modeling, localization, time-course estimation, and amplitude comparison were carried out identically to the three-network simulation. MCBF time-courses and power maps were compared against a SBF reconstruction of the same data set.

4.3.7 Median-Nerve Stimulation Task

The performance of the MCBF localization algorithm with real data was examined using human MEG responses to right median nerve stimulation. This widely-used approach to studying the somatosensory system provides a useful standard for analyzing MCBF performance since the location of activity has been well documented (Huang et al., 2005, 2006). Furthermore, median-nerve stimulation produces a complex network of closely-spaced and correlated source activation, thereby providing a challenging scenario for MCBF source localization.

MEG recordings were obtained from a single healthy male subject. The subject's median nerve was stimulated using a bipolar Grass™ constant-current stimulator. The stimuli were square-wave electric pulses of 0.2 ms duration delivered at a frequency of 1 Hz. The inter-stimulus-interval (ISI) was between 800 and 1200 ms. The intensity of the stimulation was adjusted until robust thumb twitches were observed. A trigger was designed to simultaneously send a signal to the MEG for every stimulus delivery to allow averaging over evoked trials. Magnetic fields evoked by median nerve stimulation were measured using the Elekta/Neuromag™ whole-head MEG system. Electrooculogram (EOG) electrodes were used to detect eye blinks and eye movements. An interval of 500 ms post-stimulus was recorded, using 300 ms of pre-stimulus data for noise measurement. An interval of 30 ms centered on the stimulus was discarded due to the presence of stimulus-

related artifacts. Data were sampled at 1000 Hz and run through a high-pass filter with a 0.1 Hz cut-off and through MaxFilter to remove environmental noise (Song et al., 2008; Song et al., 2009; Taulu and Simola, 2006; Taulu et al., 2004). We averaged 512 artifact-free MEG responses with respect to the stimulus trigger.

A BEM mesh of 5-mm size for the subject was generated from the inner-skull surface using volumetric T1-weighted MRI images acquired on a 1.5 T MRI scanner. To co-register MEG with MRI, we used data obtained from the Polhemus Isotrak system prior to MEG scanning. A cortical source grid of 7 mm spacing was defined using the cortical boundaries from FreeSurfer segmentation of the anatomical MRI (Dale et al., 1999; Fischl et al., 2004).

The sensor covariance matrix, $\boldsymbol{R}_b$, was constructed using the post-stimulus interval and a diagonal estimate of $\boldsymbol{R}_n$ was computed using the pre-stimulus interval (gradiometers only). Manual examination of the L-shaped region of the eigenvalue spectrum of $\boldsymbol{R}_b$ indicated that the top 10 eigenvalues could be used as a conservative estimate of the signal-related subspace (Figure 4.3). A regularization parameter equal to the eleventh largest eigenvalue of $\boldsymbol{R}_b$ was used for localization and time-course estimation with the MCBF (Sekihara et al., 2002; Sekihara et al., 2004; Van Veen et al., 1997). The regularization parameter was approximately equal to 1% of the largest

eigenvalue of $\boldsymbol{R}_b$, lying just above the noise-related eigenvalues (Figure 4.3). The MCBF localization algorithm was run until a stable plateau of Z_t was determined. A maximum collective source power map was computed to display the localization results and source time-courses were generated. MCBF time-courses and power maps were compared against a SBF reconstruction of the same data set.

4.4 Results

4.4.1 Six Dipole Simulation (3 correlated networks)

The MCBF source localization algorithm performed in an efficient manner, computing the solution for 10 cores in a little over a minute on a dual quad-core Xeon (X5550 @ 2.66GHz) Linux workstation. Furthermore, the source localization algorithm determined the correct locations of all six simulated sources. Figure 4.4 shows a plot of Z_t at each core-size. It is evident from this figure that Z_t plateaus once the correct number of sources has been modeled. Over-modeling also did not cause any errors in simulated source reconstruction; over-modeled cores were found in random locations with $Z_i \approx 0$ (i.e. noise cores). The collective source power maps in Figure 4.5a show localized activities in the left and right auditory, motor, and posterior parietal cortices that peak precisely at the simulated locations (Figure 4.2). Figure 4.6 shows a comparison of the simulated time-courses with the reconstructed time-courses. Time-course amplitude estimate errors were less

than 5% for all sources, further confirming that reasonable estimates of the source time-courses can be obtained by MCBF even in the presence of multiple pairs of highly-correlated sources.

SBF reconstruction of the source power map (Figure 4.5b) showed successful localization of activity only in the left and right posterior parietal and motor cortices. Auditory sources were not localized. Furthermore, a clear set of false sources was localized between the MC and AC dipoles in the left right hemispheres. The SBF predicted time-courses (Figure 4.6) were highly distorted with suppressed amplitude as compared to both the simulated signals and the MCBF reconstruction.

4.4.2 Six Dipole Simulation (2 correlated networks)

Once again, the MCBF source localization algorithm performed efficiently computing the solution to 10 cores in slightly over a minute. Furthermore, the source localization algorithm determined the correct locations of all six simulated sources. As in the previous simulation, Z_t plateaued once the correct number of sources had been modeled (Figure 4.7). The collective source map (Figure 4.8a) showed successful localization of the six dipoles to the left and right auditory, motor, and posterior parietal cortices in good agreement with the simulated locations. Figure 4.9 shows a comparison of the simulated time-courses with the reconstructed time-courses. The MCBF reconstruction of the six time-courses closely resembles

the true simulated signals. Time-course amplitude errors were less than 5% for all sources, indicating that MCBF performs well in a partially-correlated source environment.

SBF reconstruction of the source power map (Figure 4.8b) showed successful localization of activity only in the left and right posterior parietal cortices. Auditory and motor sources were not localized. Furthermore, a clear set of false sources was localized between the MC and AC dipoles in both left and right hemispheres. The SBF predicted time-courses (Figure 4.9) were highly distorted with suppressed amplitude as compared to both the simulated signals and the MCBF reconstruction.

4.4.3 Median-Nerve Stimulation Task

The MCBF source localization algorithm computed the solution to a core size of 18 within 10 minutes. Figure 4.10 shows that Z_t continued to increase up to a core size of 14, when it clearly began to plateau. The 14-core solution (highest value of Z_t) was chosen to compute time-courses and activity. Examination of collective power maps computed from the MCBF solutions higher than 14 cores showed no significant changes.

MEG and other functional imaging studies have established that sensory stimulation typically activates the thalamus (Huang et al., 2006; Kandel et al., 2000), BA 1, 2, and 3b of the primary somatosensory cortex (S-I) (Forss and Jousmaki, 1998; Forss et al., 1994; Hari and Forss, 1999; Hari et

al., 1993; Huang et al., 2000, 2004, 2005, 2006; Jousmaki and Forss, 1998; Kandel et al., 2000; Kawamura et al., 1996; Mauguiere et al., 1997a,b; Wood et al., 1985), BA 5 of the parietal lobe (Boakye et al., 2000; Forss et al., 1994; Huang et al., 2006; Jones et al., 1978; Jones et al., 1979; Kandel et al., 2000; McGlone et al., 2002; Waberski et al., 2002), and BA 23 and 40 of the secondary somatosensory cortex (S-II) (Forss and Jousmaki, 1998; Fujiwara et al., 2002; Hari and Forss, 1999; Hari et al., 1993; Huang et al., 2005, 2006; Kandel et al., 2000; Simoes et al., 2003). The collective power map produced by the MCBF localization (Figure 4.11a) shows activation in these regions as well as in others, including the insular cortex (IC), in the parietal-occipital junction, and the cingulate gyrus. SBF reconstruction of the same data set (Figure 4.11b) showed only activity in areas BA 1, 2, and 3b of the primary somatosensory cortex (S-I) and the parietal-occipital junction while missing expected neuronal sources in BA 5 of the posterior parietal lobe and in the secondary somatosensory cortex.

MCBF time-course reconstruction was examined as well (Figure 4.12). The S-I activation (BA 3b) showed a strong transient response 20 ms following stimulation. The S-II activation showed a much smaller transient response with a large delayed response peaking at about 90 ms. The latencies of these peak activations as well as the general wave-shape agree with previous neurological studies (Boakye et al., 2000; Forss and Jousmaki, 1998; Hari and Forss, 1999; Huang et al., 2006). Furthermore, the strong similarity between

recorded and predicted sensor waveforms indicates that the MCBF solution reasonably explains the underlying source configuration. SBF time-course reconstruction (Figure 4.13), on the other hand, showed only transient activity for both the S-I and S-II activations. Slower components of the response visible in the MCBF reconstruction (50 – 175 ms) were lost in the noisier waveforms. Furthermore, comparison of the predicted and actual sensor waveforms as generated by the SBF indicates that the SBF predicted source activity is insufficient to explain the underlying neuronal source distribution, especially between 50 and 175 ms post-stimulus.

4.5 Discussion

Our computer simulations and analyses of real data demonstrated that the MCBF is capable of reconstructing source locations and correlated activities with minimal distortion and suppression, resolving complex networks using the proposed localization algorithm. We showed its capacity to handle a multi-dimensional search problem with ease. The MCBF search algorithm required no *a priori* information and reduced processing time to the order of minutes (instead of hours or even days when applying a brute-force approach), as well as accurately reconstructed source activity maps and time-courses.

To test the limits of MCBF as well as the search algorithm, challenging simulations were designed. Instead of the three sources typically used in

beamformer simulations, we employed six sources to examine both inter-hemispheric and intra-hemispheric networks that contained varying degrees of correlation. Sources were resolved accurately to the correct grid points within minutes, with their respective time courses closely mirroring the simulated signals (< 5% error). These findings confirmed the MCBF's promising capacity to recover underlying network activity accurately and quickly with minimal distortion. The simulation results also demonstrated the algorithm's robustness to the possibility of over-modeling. Not only was the occurrence easily detectable by means of a visually observable plateau in Z_t, but the simulated source configuration itself remained stable despite the additional cores. Furthermore, SBF reconstructions of the same simulations showed that the conventional beamformer, unlike the MCBF, is unable to properly localize and predict time-courses of correlated neuronal activity.

The algorithm was further tested with a real MEG recording to confirm its localization performance in complex scenarios. Evoked recordings of right-hand median-nerve stimulation provided a challenging environment containing many correlated sources within close proximity to each other. The MCBF algorithm once again performed well, providing an easily detectable Z_t plateau that was used for obtaining a final solution. The locations as well as the time-courses of the resolved sources agreed with previous observations of median-nerve activity (Huang et al., 2006; Kandel et al., 2000). Source activities appeared to be linear combinations of the sensor waveforms (Figure 4.12), an

important physical characteristic of the MEG system, confirming that a meaningful solution was derived. Moreover, forward modeling of the reconstructed source activity showed close agreement to the recorded sensor waveforms. SBF reconstruction, on the other hand, was unable to attain the same degree of detail in localization or dynamics of source activity. In fact, the SBF predicted sensor waveforms poorly resembled recorded sensor waveforms unlike the MCBF. Finally, the MCBF reconstruction was performed without the use of any prior knowledge, demonstrating its advantage over the NB and CSSM when handling correlated source activities (Dalal et al., 2006; Hui and Leahy, 2006; Hui and Leahy, 2010; Quuran and Cheyne, 2010).

Our results further suggest that the application of MCBF in functional connectivity analyses holds promise as it offers the ability to compute volumetric time-course and power maps, which is a novel property unavailable in previously developed multi-source beamformers that could only determine time-courses at the core locations (Brookes et al., 2007; Diwakar et al., 2011a; Diwakar et al., 2011b). Similar to the nulling beamformer, volumetric activity maps can be computed and combined for each set of constraints present in the MCBF core. Volumetric time-courses can be used in various analyses such as computation of coherence maps for resting state network data (Brookes et al., 2011; Mantini et al., 2011; de Pasquale et al., 2010). Since each nulling constraint reduces time-course distortion and the MCBF optimizes the selection of these constraints, MCBF derived time-courses

better replicate true source activity, improving the ability of beamformers to investigate neural communication.

In conclusion, we have developed a search algorithm for source localization with MCBF, an advanced spatial filter capable of handling intricate networks of correlated sources. The algorithm quickly finds stable and accurate solutions for the MCBF in both simulated and real experiments. Though some beamformer variations (e.g. NB and CSSM) can resolve correlated sources, the MCBF is the first beamformer capable of handling complex datasets without any *a priori* information. The MCBF also produces volumetric source activity estimates that can be used to study neural connectivity. In our current approach, MCBF utilizes a dipole-activation model that is appropriate for focal sources such as those found in evoked MEG recordings. In the future, we plan to further develop MCBF to allow use of a patch activation model that is suitable for distributed sources such as those found in spontaneous MEG recordings. This will create a beamformer more fit for the investigation of resting-state activity, a topic at the forefront of current neuroimaging studies (Brookes et al., 2011; Mantini et al., 2011; de Pasquale et al., 2010).

4.6 Acknowledgments

This work was supported in part by McDonnell Foundation via the Brain Trauma Foundation (PI: J. Ghajar, site PIs: R.R. Lee and M.X. Huang); Merit

Review Grants from the Department of Veterans Affairs two for M.X. Huang, one for R.R. Lee, and one for D.L. Harrington (#1IO1CX000146-01 and #B501R); the National Football League (M.X. Huang and R.R. Lee); the National Institutes of Health grants to T. Liu (2R01-NS051661), to R. Srinivasan (R01-MH068004), and to S. Chien (5-T32 HL-7089-35); and the Office of Naval Research to D.L. Harrington and T. Liu (N00141010072). The authors would like to thank Aileen Ung for her assistance in preparing the figures.

Chapter 4, in part, has been submitted for publication of the material as it may appear in NeuroImage, 2011. Tal, Omer; Diwakar, Mithun; Liu, Thomas T.; Harrington, Deborah L.; Lee, Roland R.; Muzzatti, Laura; Theilmann, Rebecca J.; Srinivasan, Ramesh; Huang, Ming-Xiong. The dissertation author was co-first author of this material.

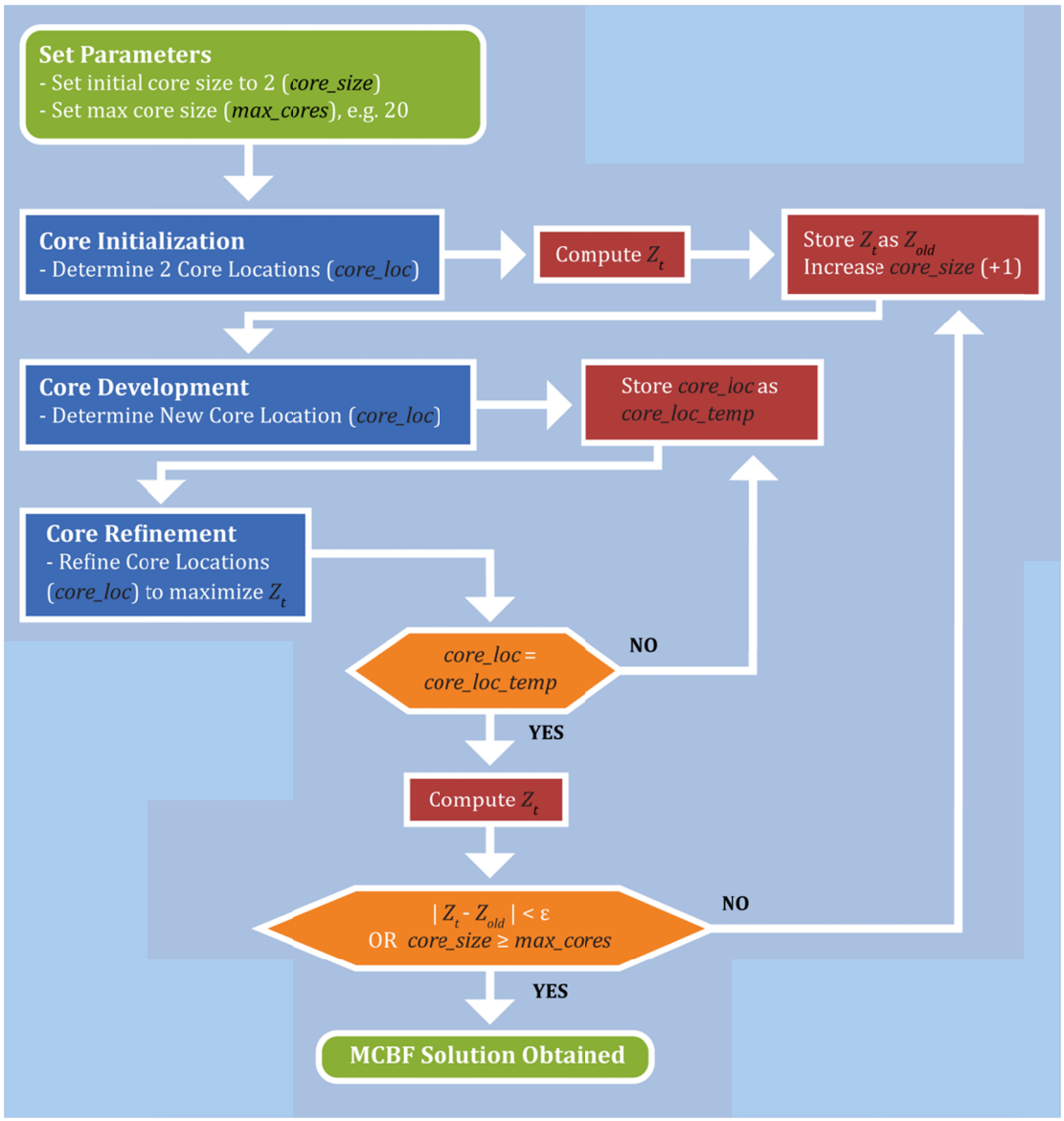

Figure 4.1: MCBF search algorithm flowchart. Variables are denoted in black font. Squares = actions. Hexagons = decisions.

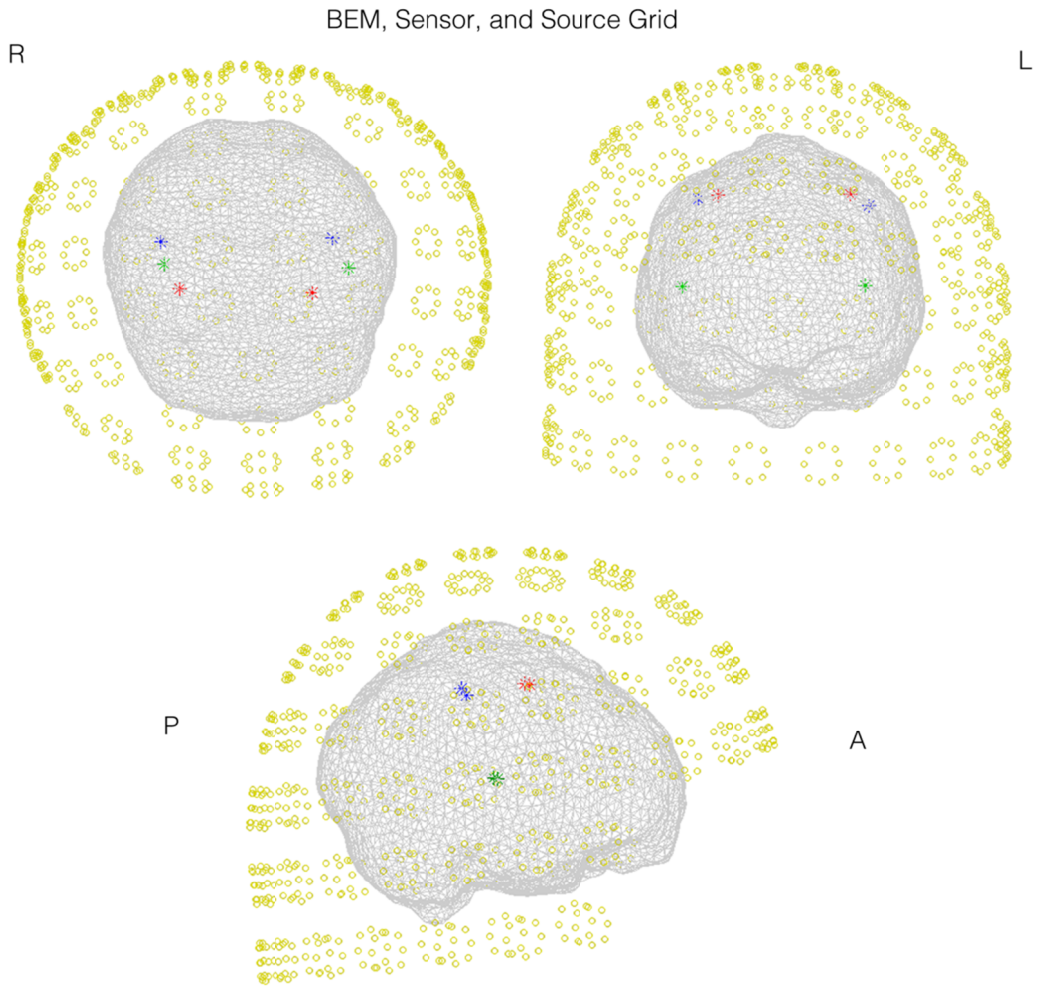

Figure 4.2: Source placement. Axial (top left), coronal (top right), and sagittal (bottom) views of the simulated source placement, BEM mesh, and sensor integration points. Red = Motor cortex dipoles; Green = Auditory cortex dipoles; Blue = Posterior parietal cortex dipoles.

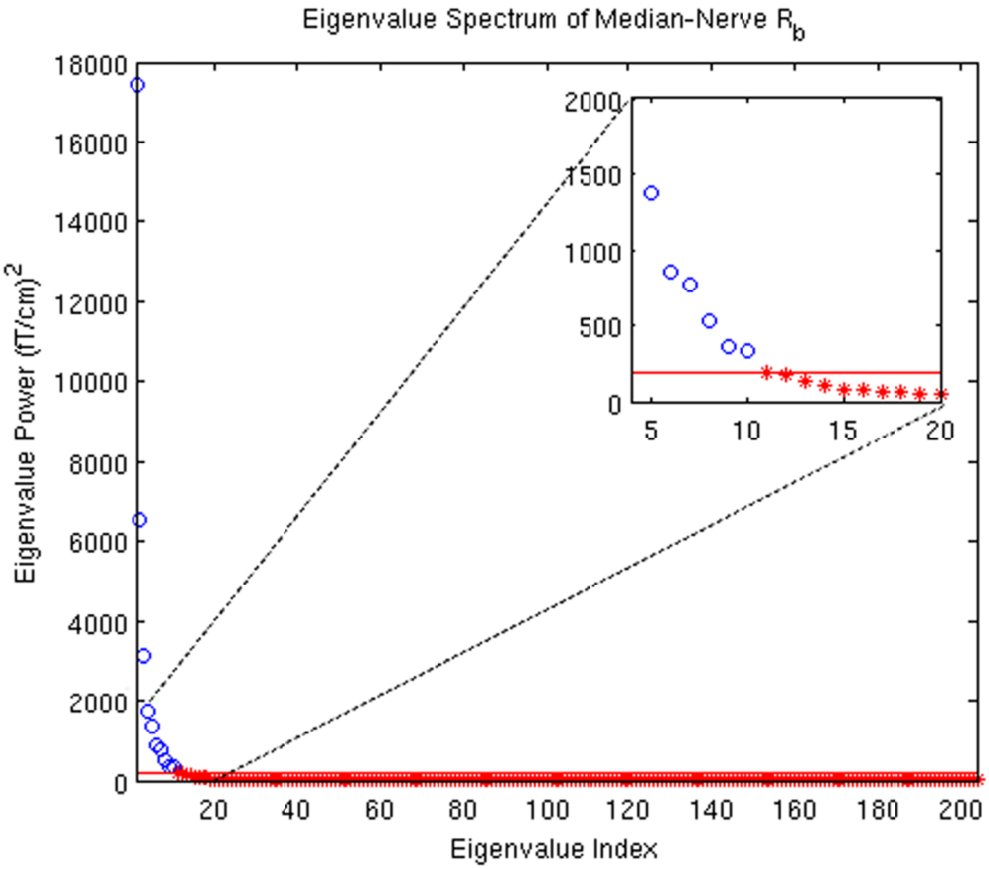

Figure 4.3: Eigenvalue spectrum of median-nerve sensor covariance. Blue eigenvalues = signal-related; red eigenvalues = noise-related; red line = regularization parameter.

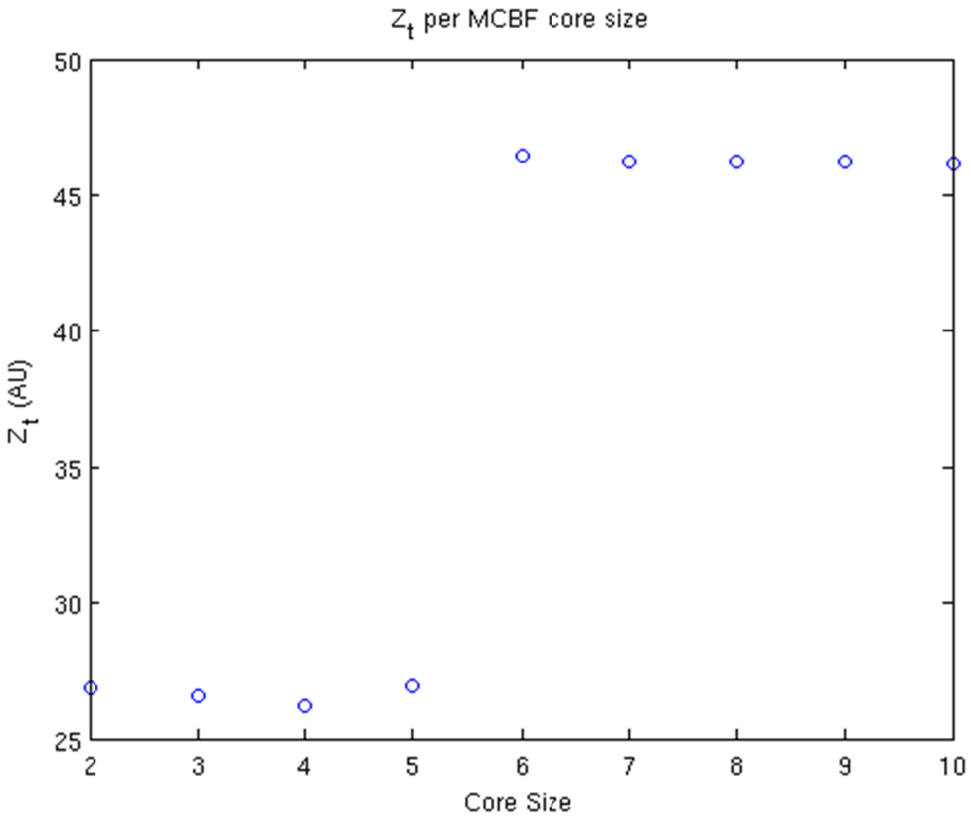

Figure 4.4: Total pseudo-Z-score per MCBF core-size for the three correlated network simulation. A stable plateau is achieved at the correct model order of six cores.

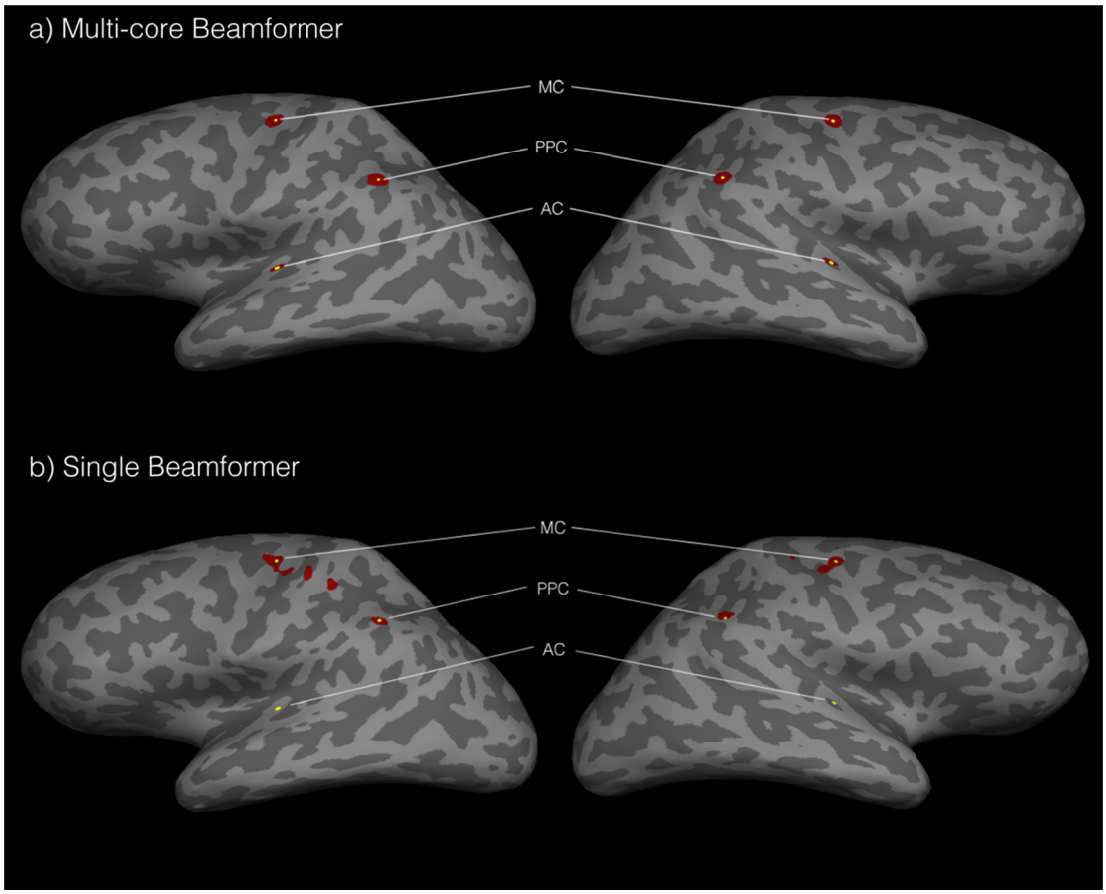

Figure 4.5: MCBF and SBF source activity maps for the left and right hemisphere from the three network simulation. MCBF maps were computed by taking the maximum pseudo-Z-score of the individual source maps at each grid point. The threshold for pseudo-Z scores in regions color-coded red is $p < 0.008$. Yellow markers denote the original simulated locations. MC = motor cortex; AC = auditory cortex; PPC = posterior parietal cortex.

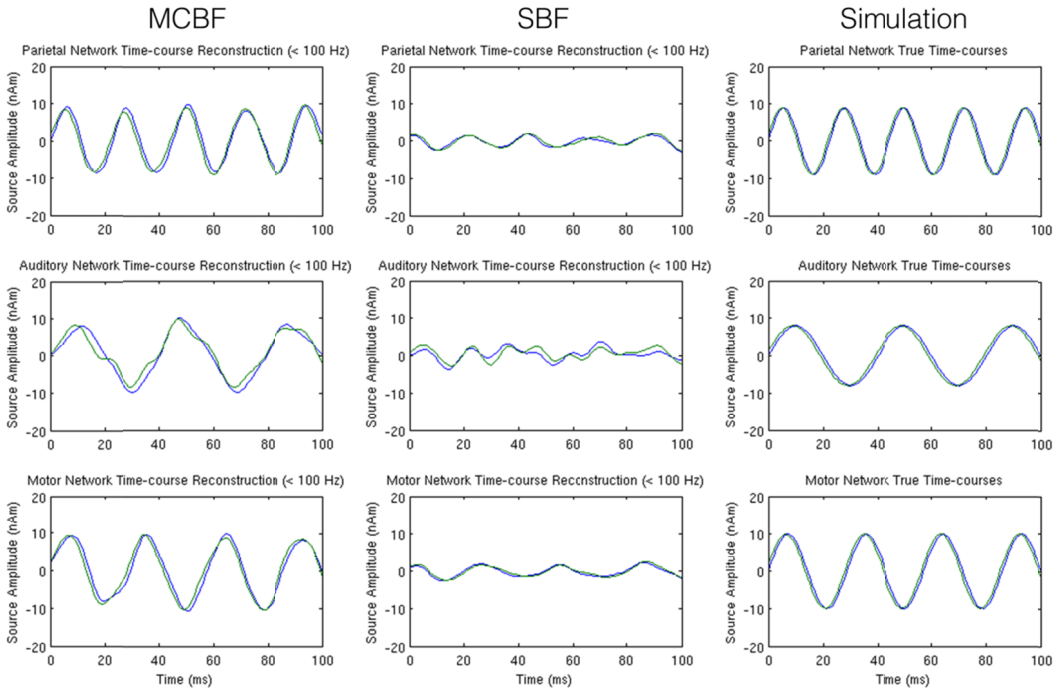

Figure 4.6: Reconstructed time-courses for the three network simulation. Left panels display the MCBF reconstructed waveforms. Center panels display the SBF reconstructed waveforms. Right panels display the true simulated waveforms. Blue = left hemisphere; Green = right hemisphere.

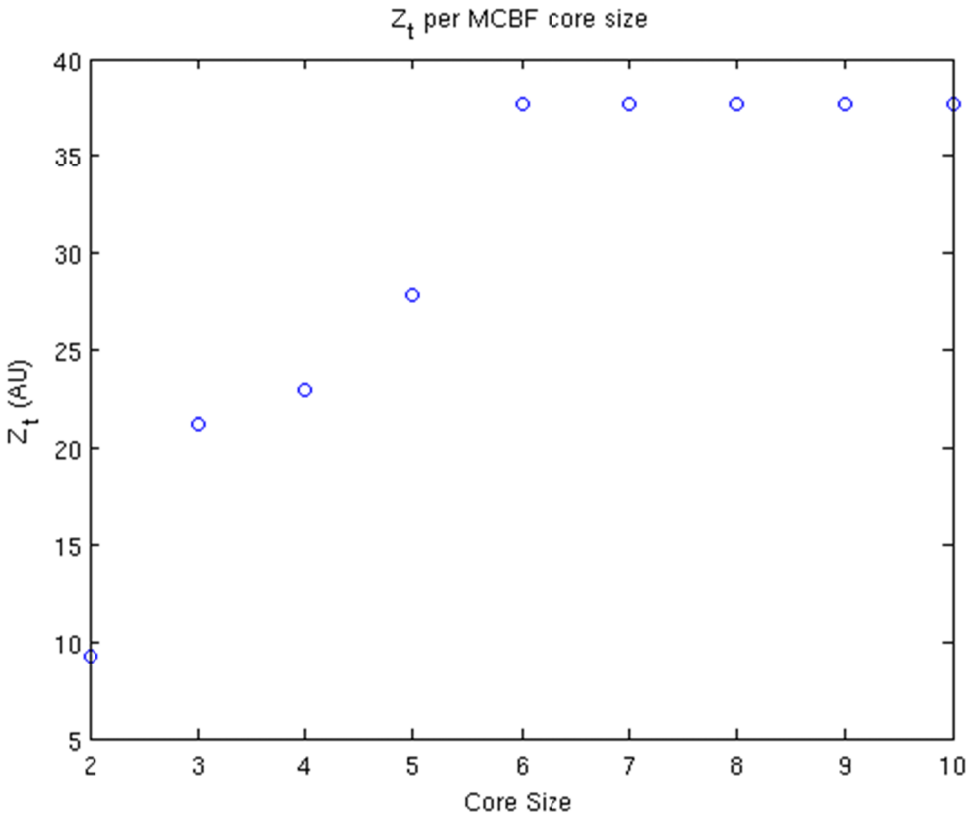

Figure 4.7: Plot of Z_t at each core-size for the two network simulation. A stable plateau is found at the correct model order of six cores.

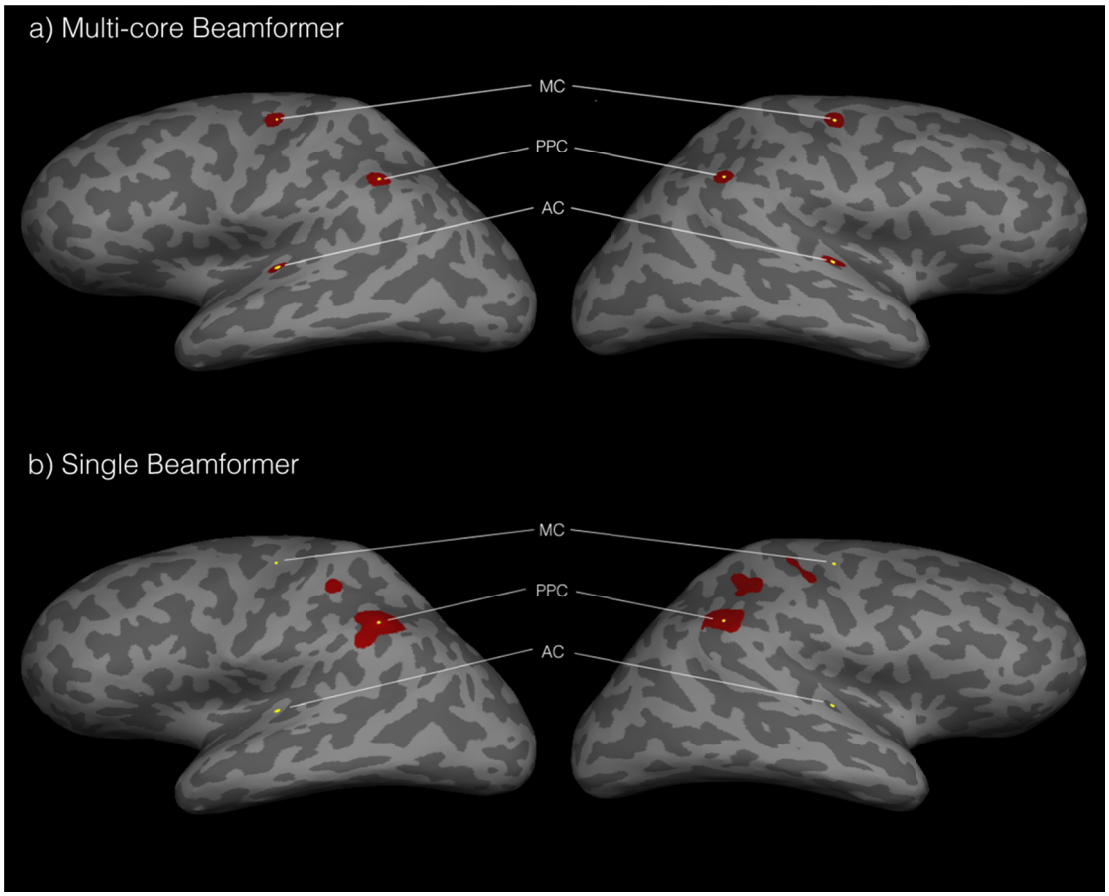

Figure 4.8: MCBF and SBF source activity maps for the left and right hemispheres from the two network simulation. MCBF maps were computed by taking the maximum pseudo-Z-score of the individual source maps at each grid point. The threshold for pseudo-Z scores in regions color-coded red is $p < 0.008$. Yellow markers denote the original simulated locations. MC = motor cortex; AC = auditory cortex; PPC = posterior parietal cortex.

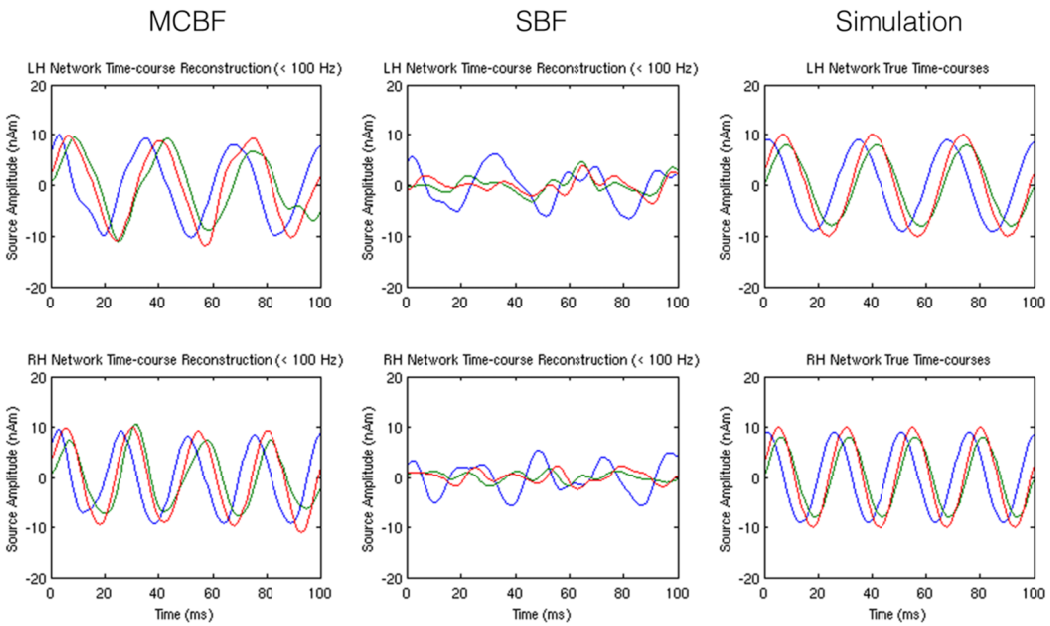

Figure 4.9: Reconstructed time-courses for the two network simulation. Left panels display the MCBF estimated waveforms. Center panels display the SBF reconstructed waveforms. Right panels display the simulated waveforms. Green = auditory cortex dipoles; Red = motor cortex dipoles; Blue = posterior parietal cortex dipoles.

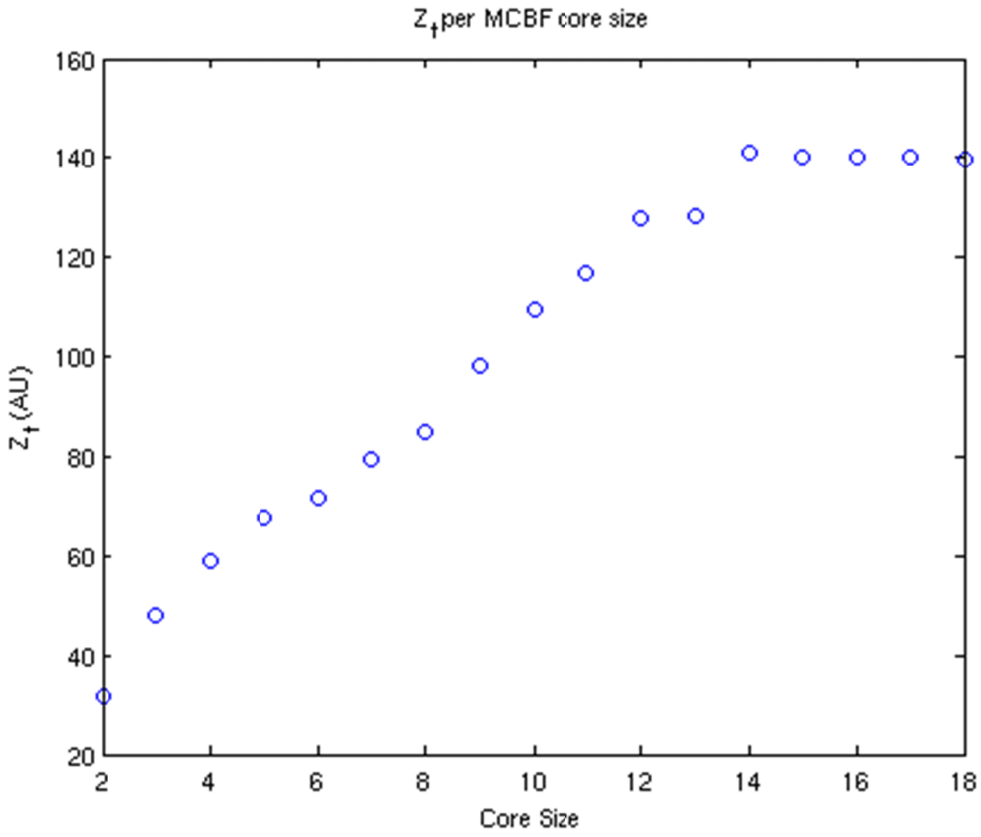

Figure 4.10: Median-nerve total pseudo-Z-scores per MCBF core size. A stable plateau was achieved at 14 cores.

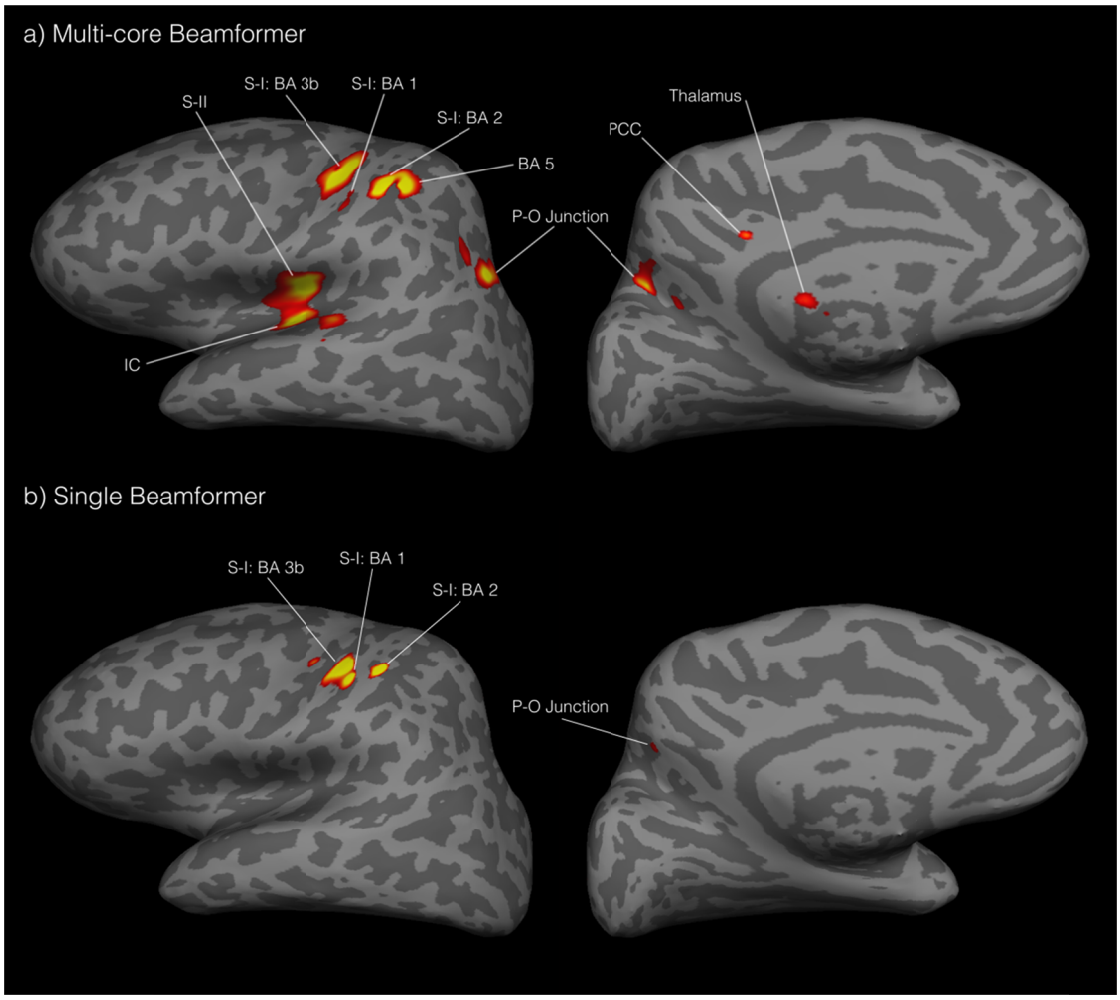

Figure 4.11: Median-nerve MCBF and SBF source activity maps. The threshold for regions color-coded red and yellow is $p < 0.02$ and $p < 0.005$, respectively. IC = insular cortex; S-I = primary sensory cortex; S-II = secondary sensory cortex; BA = Brodmann area; P-O = parietal-occipital; PCC = posterior cingulate cortex.

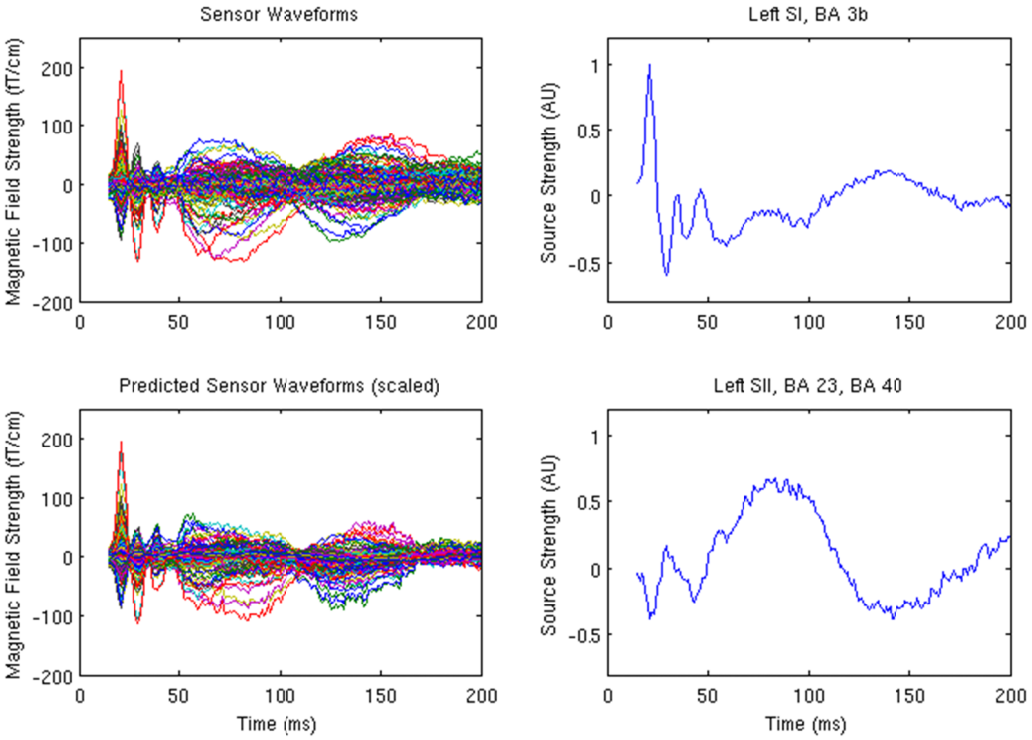

Figure 4.12: MCBF reconstructed median-nerve time-courses. Right panels display the S-I (BA 3b) and S-II area time-courses. Left panels display the recorded and predicted sensor gradiometer waveforms computed from the time-courses of the regions shown in Figure 4.11a.

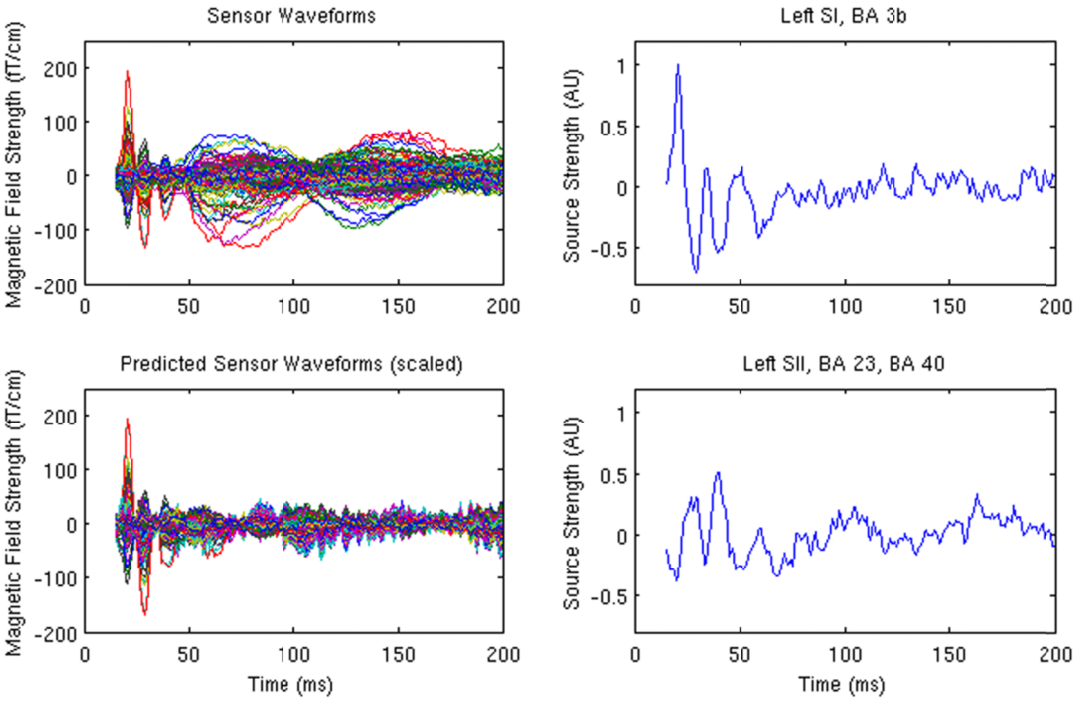

Figure 4.13: SBF reconstructed median-nerve time-courses. Right panels display the S-I (BA 3b) and S-II area time-courses. Left panels display the recorded and predicted sensor gradiometer waveforms computed from the time-courses of the regions shown in Figure 4.11b.

4.7 References

Boakye, M., Huckins, S.C., Szeverenyi, N.M., Taskey, B.I., Hodge, C.J. Jr., 2000. Functional magnetic resonance imaging of somatosensory cortex activity produced by electrical stimulation of the median nerve or tactile stimulation of the index finger. J. Neurosurg. 93, 774–783.

Brookes, M.J., Hale, J.R., Zumer, J.M., Stevenson, C.M., Francis, S.T., Barnes, G.R., Owen, J.P., Morris, P.G., Nagarajan, S.S., 2011. Measuring functional connectivity using MEG: methodology and comparison with fcMRI. NeuroImage 56, 1082-1104.

Brookes, M.J., Stevenson, C.M., Barnes, G.R., Hillebrand, A., Simpson, M.I.G., Francis, S.T., Morris, P.G., 2007. Beamformer reconstruction of correlated sources using a modified source model. NeuroImage 34, 1454-1465.

Dalal, S.S., Sekihara, K., Nagarajan, S.S., 2006.Modified Beamformers for Coherent Source Region Suppression. IEEE Trans. Biomed. Eng. 53, 1357-1363.

Dale, A.M., Fischl, B., Sereno, M.I., 1999. Cortical surface-based analysis: I. Segmentation and surface reconstruction. NeuroImage 9, 179-194.

Diwakar, M., Huang, M.X., Srinivasan, R., Harrington, D.L., Robb, A., Angeles, A., Muzzatti, L., Pakdaman, R., Song., T., Theilmann, R.J., Lee, R.R., 2011a. Dual-Core Beamformer for obtaining highly correlated neuronal networks in MEG. NeuroImage 54, 253-263.

Diwakar, M., Tal, O., Liu, T.T, Harrington, D.L., Srinivasan, R., Muzzatti, L., Song, T., Theilmann, R.J., Lee, R.R., Huang, M.X., 2011b. Accurate Reconstruction of Temporal Correlation for Neuronal Sources using the Enhanced Dual-core MEG Beamformer. NeuroImage 56, 1918-1928.

Forss, N., Jousmaki, V., 1998. Sensorimotor integration in human primary and secondary somatosensory cortices. Brain Res. 781, 259–267.

Forss, N., Hari, R., Salmelin, R., Ahonen, A., Hamalainen, M., Kajola, M., Knuutila, J., Simola, J., 1994. Activation of the human posterior parietal cortex by median nerve stimulation. Exp. Brain Res. 99, 309–315.

Fujiwara, N., Imai, M., Nagamine, T., Mima, T., Oga, T., Takeshita, K., Toma, K., Shibasaki, H., 2002. Second somatosensory area (SII) plays a significant role in selective somatosensory attention. Brain Res. Cogn.

Brain Res. 14, 389–397.

Hamalainen, M.S., Ilmoniemi, R.J., 1994. Interpreting magnetic fields of the brain: minimum norm estimates. Med. Biol. Eng. Comput. 32, 35-42.

Hari, R., Forss, N., 1999. Magnetoencephalography in the study of human somatosensory cortical processing. Philos. Trans. R. Soc. Lond., B Biol. Sci. 354, 1145–1154.

Hari, R., Karhu, J., Hamalainen, M., Knuutila, J., Salonen, O., Sams, M., Vilkman, V., 1993. Functional organization of the human first and second somatosensory cortices: a neuromagnetic study. Eur. J. Neurosci. 5, 724–734.

Huang, M.X., Aine, C., Davis, L., Butman, J., Christner, R., Weisend, M., Stephen, J., Meyer, J., Silveri, J., Herman, M., Lee, R.R., 2000. Sources on the anterior and posterior banks of the central sulcus identified from magnetic somatosensory evoked responses using multistart spatio- temporal localization. Hum. Brain Mapp. 11, 59–76.

Huang, M., Davis, L.E., Aine, C., Weisend, M., Harrington, D., Christner, R., Stephen, J., Edgar, J.C., Herman, M., Meyer, J., Paulson, K., Martin, K., Lee, R.R., 2004a. MEG response to median nerve stimulation correlates with recovery of sensory and motor function after stroke. Clin. Neurophysiol. 115, 820–833.

Huang, M.X., Lee, R.R., Miller, G.A., Thoma, R.J., Hanlon, F.M., Paulson, K.M., Martin, K., Harrington, D.L., Weisend, M.P., Edgar, J.C., Canive, J.M., 2005. A parietal–frontal network studied by somatosensory oddball MEG responses, and its cross-modal consistency. NeuroImage 28, 99–114.

Huang, M., Dale, A.M., Song, T., Halgren, E., Harrington, D.L., Podgorny, I., Canive, J.M., Lewis, S., Lee, R.R., 2006. Vector-based spatial-temporal minimum L1-norm solution for MEG. NeuroImage 31, 1025-1037.

Huang, M.X., Song, T., Hagler, D.J., Podgorny, I., Jousmaki, V., Cui, L., Gaa, K., Harrington, D.L., Dale, A.M., Lee, R.R., Elman, J., Halgren, E., 2007. A novel integrated MEG and EEG analysis method for dipolar sources. NeuroImage 37, 731-748.

Hui, H.B., Leahy, R.M., 2006. Linearly constrained MEG beamformers for MVAR modeling of cortical interactions. 3rd IEEE International

Symposium on Biomedical Imaging: Nano to Macro, 2006, pp. 237–240.

Hui, H.B., Pantazis, D., Bressler, S.L., Leahy, R.M., 2010. Identifying true cortical interactions in MEG using the nulling beamformer. NeuroImage 49, 3161-3174.

Jones, E.G., Coulter, J.D., Hendry, S.H., 1978. Intracortical connectivity of architectonic fields in the somatic sensory, motor and parietal cortex of monkeys. J. Comp. Neurol. 181, 291–347.

Jones, E.G., Wise, S.P., Coulter, J.D., 1979. Differential thalamic relationships of sensory-motor and parietal cortical fields in monkeys. J. Comp. Neurol. 183, 833–881.

Jousmaki, V., Forss, N., 1998. Effects of stimulus intensity on signals from human somatosensory cortices. NeuroReport 9, 3427–3431.

Kandel, E.R., Schwartz, J.H., Jessell, T.M., 2000. Principles of Neural Science. McGraw Hill, New York.

Kawamura, T., Nakasato, N., Seki, K., Kanno, A., Fujita, S., Fujiwara, S., Yoshimoto, T., 1996. Neuromagnetic evidence of pre- and post-central cortical sources of somatosensory evoked responses. Electroencephalogr. Clin. Neurophysiol. 100, 44–50.

Kumihashi, I., Sekihara, K., 2010. Array-gain constraint minimum-norm spatial filter with recursively updated gram matrix for biomagnetic source imaging. IEEE Trans. Biomed. Eng. 57, 1358-1365.

Mantini, D., Della Penna, S., Marzetti, L., de Pasquale, F., Pizzella, V., Corbetta, M., Romani, G.L., 2011. A signal-processing pipeline for magnetoencephalography resting-state networks. Brain Connectivity 1, 49-59.

Mauguiere, F., Merlet, I., Forss, N., Vanni, S., Jousmaki, V., Adeleine, P., Hari, R., 1997a. Activation of a distributed somatosensory cortical network in the human brain. A dipole modeling study of magnetic fields evoked by median nerve stimulation: Part I. Location and activation timing of SEF sources. Electroencephalogr. Clin. Neurophysiol. 104, 281–289.

Mauguiere, F., Merlet, I., Forss, N., Vanni, S., Jousmaki, V., Adeleine, P., Hari, R., 1997b. Activation of a distributed somatosensory cortical network in the human brain: a dipole modeling study of magnetic fields evoked by

median nerve stimulation: Part II. Effects of stimulus rate, attention and stimulus detection. Electroencephalogr. Clin. Neurophysiol. 104, 290–295.

McGlone, F., Kelly, E.F., Trulsson, M., Francis, S.T., Westling, G., Bowtell, R., 2002. Functional neuroimaging studies of human somatosensory cortex. Behav. Brain Res. 135, 147–158.

Mosher, J.C., Leahy, R.M., Lewis, P.S., 1999. EEG and MEG: forward solutions for inverse methods. IEEE Trans. Biomed. Eng. 46, 245-259.

de Pasquale, F., Della Penna, S., Snyder, A.Z., Lewis, C., Mantini, D., Marzetti, L., Belardinelli, P., Ciancetta, L., Pizzella, V., Romani, G.L., Corbetta, M., 2010. Temporal dynamics of spontaneous MEG activity in brain networks. Proc. Natl. Acad. Sci. U. S. A. 107, 6040-6045.

Quuran, M.A., Cheyne, D., 2010. Reconstruction of correlated brain activity with adaptive spatial filters in MEG. NeuroImage 49, 2387-2400.

Robinson, S., Vrba, J., 1998. Functional neuroimaging by synthetic aperture magnetometry. In: Yoshimoto, T., Kotani, M., Kuriki, S., Karibe, H., Nakasato, N. (Eds.), Recent Advances in Biomagnetism. Tohoku Univ. Press, Sendai, pp. 302-305.

Sekihara, K., Nagarajan, S., 2008. Adaptive spatial filters for electromagnetic brain imaging. Berlin, Heidelber: Springer-Verlag.

Sekihara, K., Nagarajan, S., Poeppel, D., Marantz, A., 2002. Performance of an MEG adaptive-beamformer technique in the presence of correlated neural activities: effects on signal intensity and time course estimates. IEEE Trans. Biomed. Eng. 49 (12), 1534-1546.

Sekihara, K., Nagarajan, S., Poeppel, D., Marantz, A., 2004. Asymptotic SNR of scalar and vector minimum-variance beamformers for neuromagnetic source reconstruction. IEEE Trans. Biomed.Eng. 51 (10), 1726-1733.

Simoes, C., Jensen, O., Parkkonen, L., Hari, R., 2003. Phase locking between human primary and secondary somatosensory cortices. Proc. Natl. Acad. Sci. U. S. A. 100, 2691–2694.

Singer, W., 1999. Neuronal Synchrony: A Versatile Code for the Definition of Relations? Neuron 24, 49-65.

Song, T., Cui, L., Gaa, K., Feffer, L., Taulu, S., Lee, R.R., Huang, M.X., 2009. Signal Space Separation Algorithm and Its Application on Suppressing Artifacts Caused by Vagus Nerve Stimulation for Magnetoencephalography Recordings. J. Clin. Neurophysiol. 26 (6), 392-400.

Song, T., Gaa, K., Cui, L., Feffer, L., Lee, R.R., Huang, M.X., 2008.Evaluation of signal space separation via simulation. Med. Biol. Eng. Comput. 46, 923-932.

Taulu, S., Kajola, M., Simola, J., 2004. Suppression of interference and artifacts by the signal space separation method. Brain Topogr. 16, 269-275.

Taulu, S., Simola, J., 2006. Spatiotemporal signal space separation method for rejecting nearby interference in MEG measurements. Phys. Med. Biol. 51, 1759-1768.

Van Drongelen, W., Yuchtman, M., Van Veen, B.D., Van Huffelen, A.C., 1996. A spatial filtering technique to detect and localize multiple sources in the brain. Brain Topogr. 9 (1), 39-49.

Van Veen, B.D., Van Drognelen, W., Yuchtman, M., Suzuku, A., 1997. Localization of brain electrical activity via linearly constrained minimum variance spatial filtering. IEEE Trans. Biomed. Eng. 44 (9), 867-880.

Vrba, J., Robinson, S.E., 2001. Signal processing in magnetoencephalography. Methods 25 (2), 249-271.

Waberski, T.D., Gobbele, R., Darvas, F., Schmitz, S., Buchner, H., 2002. Spatiotemporal imaging of electrical activity related to attention to somatosensory stimulation. NeuroImage 17, 1347–1357.

Wood, C.C., Cohen, D., Cuffin, B.N., Yarita, M., Allison, T., 1985. Electrical sources in human somatosensory cortex: identification by combined magnetic and potential recordings. Science 227, 1051–1053.

CHAPTER 5

Conclusions

Magnetoencephalography is a rapidly developing and useful functional imaging technique for detecting neuronal activity. The major problem with MEG concerns developing an accurate inverse solution that truly represents underlying source activity computed from real magnetic measurements. Many different types of constraints may be applied to the sensor recordings in order to generate solutions. One such method, the minimum variance beamformer, is formulated as an adaptive spatial filter that employs the sensor covariance matrix to attain high spatial resolution. Furthermore, the beamformer is quick to compute and avoids the large number of parameters present in other methods (Van Drongelen et al., 1996; Van Veen et al., 1997; Robinson and Vrba, 1998; Sekihara et al., 2004). Unfortunately, the conventional beamformer assumes that the different neuronal sources are uncorrelated, hence, suffers large errors in source localization and distortion in both power and time-course estimation in the presence of correlated source activity. In the case of highly correlated sources, the conventional beamformer approaches fail to detect sources completely (Sekihara et al., 2002; Sekihara and Nagarajan, 2008).

In real experiments, it is expected that neuronal sources communicate and are therefore at least partially correlated. For example, in auditory evoked fields (AEFs), highly synchronous bilateral activation is commonplace. In spite

of its limitation with correlated sources, single beamformers are still applied widely in studying neural responses. Recently, there has been a growing trend to analyze resting state spontaneous recordings and compare the resulting brain activity to well-characterized resting state networks in fMRI (de Pasquale et al., 2010; Brookes et al., 2011; Mantini et al., 2011). However, such analyses may miss highly correlated neuronal sources and suffer distortion of time-courses.

Different techniques have been proposed to address this issue. The nulling beamformer (NB) and coherent source suppression model (CSSM) deal with correlated sources by imposing nulling constraints. However, as a practical tool, the NB and CSSM require *a priori* knowledge of source locations, making it difficult to analyze novel data (Dalal et al., 2006; Hui and Leahy, 2006; Hui et al., 2010; Quuran and Cheyne, 2010). Another approach to dealing with the correlated source problem involves pointing the beamformer spatial filter at multiple locations at once. The first such beamformer developed, the dual-source beamformer (DSBF), is capable of accurate source localization in the presence of two correlated sources without *a priori* information. However, the DSBF suffered from the inability to reconstruct individual source time-courses and required multiple and computationally time-consuming non-linear searches (Brookes et al., 2007).

In this dissertation, a logical progression of developing the multi-core beamformer (MCBF) which does not suffer from the disadvantages of the

DSBF, NB, or CSSM is presented. By incorporating the vector formulation into the DSBF, the dual-core beamformer (DCBF) is able to successfully reconstruct simulated and real data without the need for many of the expensive non-linear searches required by the DSBF, greatly speeding up and making reconstruction far more practical (Diwakar et al., 2011a). Further development of the DCBF led to the formulation of the enhanced dual-core beamformer (eDCBF), which further improves reconstructions by allowing computation of source correlation, accurate power estimates, and accurate and individual time-course estimates (Diwakar et al., 2011b). However, the presence of more than two correlated sources creates the same type of distortion present in the single beamformer.

The eDCBF was naturally extended to the multi-core beamformer (MCBF) which is capable of handling a large number of correlated sources (Diwakar et al., 2011b). However, due to the increased dimensionality of the MCBF, source localization becomes a difficult problem. To handle this issue, we also developed an MCBF source localization algorithm that was shown to successfully localize sources and detect the correct number of sources in both simulated and real experiments. Finally, detailed examination of MCBF and NB mathematics showed a very close relationship between the methods (Dalal et al., 2006). This relationship was exploited in order to allow the MCBF to reconstruct source time-courses across the entire brain region, a quality that was unavailable with the previous multi-source techniques (DSBF, DCBF,

eDCBF). In fact, mathematically, the MCBF solution is as accurate as the NB solution but also provides an automated method of determining nulling constraints, preventing the need for *a priori* information.

The development of the MCBF is significant to the field of MEG inverse modeling. Since the beamformer can accurately deal with correlated sources, it can be used in place of conventional beamformers in many applications. For example, we expect that use of the MCBF in brain connectivity analyses instead of the vector beamformer will greatly improve detection of resting-state networks in MEG. The MCBF can also play a significant role in the reconstruction of low SNR recordings, as it is not as susceptible to noise as non-beamforming time-point-by-time-point methodologies such as the L1-minimum norm, L2-minimum norm, and VESTAL.

In the future, we plan to modify the MCBF model so that it accounts for patch activation and the presence of non-dipolar sources. Such a modified model will allow better source localization and activity estimation in experiments where large parts of the cortex are simultaneously active. Furthermore, we plan to use the MCBF to analyze spontaneous recordings to develop a better understanding of resting-state networks in MEG and their correlates in fMRI. The MCBF provides an important and needed tool for the advancement of our understanding of brain activity in states of both health and disease.

5.1 References

Brookes, M.J., Hale, J.R., Zumer, J.M., Stevenson, C.M., Francis, S.T., Barnes, G.R., Owen, J.P., Morris, P.G., Nagarajan, S.S., 2011. Measuring functional connectivity using MEG: methodology and comparison with fcMRI. NeuroImage 56, 1082-1104.

Brookes, M.J., Stevenson, C.M., Barnes, G.R., Hillebrand, A., Simpson, M.I.G., Francis, S.T., Morris, P.G., 2007. Beamformer reconstruction of correlated sources using a modified source model. NeuroImage 34, 1454-1465.

Dalal, S.S., Sekihara, K., Nagarajan, S.S., 2006. Modified Beamformers for Coherent Source Region Suppression. IEEE Trans. Biomed. Eng. 53, 1357-1363.

Diwakar, M., Huang, M.X., Srinivasan, R., Harrington, D.L., Robb, A., Angeles, A., Muzzatti, L., Pakdaman, R., Song., T., Theilmann, R.J., Lee, R.R., 2011a. Dual-Core Beamformer for obtaining highly correlated neuronal networks in MEG. NeuroImage 54, 253-263.

Diwakar, M., Tal, O., Liu, T.T, Harrington, D.L., Srinivasan, R., Muzzatti, L., Song, T., Theilmann, R.J., Lee, R.R., Huang, M.X., 2011b. Accurate Reconstruction of Temporal Correlation for Neuronal Sources using the Enhanced Dual-core MEG Beamformer. NeuroImage 56, 1918-1928.

Hui, H.B., Leahy, R.M., 2006. Linearly constrained MEG beamformers for MVAR modeling of cortical interactions. 3rd IEEE International Symposium on Biomedical Imaging: Nano to Macro, 2006, pp. 237–240.

Hui, H.B., Pantazis, D., Bressler, S.L., Leahy, R.M., 2010. Identifying true cortical interactions in MEG using the nulling beamformer. NeuroImage 49, 3161-3174.

Mantini, D., Della Penna, S., Marzetti, L., de Pasquale, F., Pizzella, V., Corbetta, M., Romani, G.L., 2011. A signal-processing pipeline for magnetoencephalography resting-state networks. Brain Connectivity 1, 49-59.

de Pasquale, F., Della Penna, S., Snyder, A.Z., Lewis, C., Mantini, D., Marzetti, L., Belardinelli, P., Ciancetta, L., Pizzella, V., Romani, G.L., Corbetta, M., 2010. Temporal dynamics of spontaneous MEG activity in brain networks. Proc. Natl. Acad. Sci. U. S. A. 107, 6040-6045.

Quuran, M.A., Cheyne, D., 2010. Reconstruction of correlated brain activity with adaptive spatial filters in MEG. NeuroImage 49, 2387-2400.

Robinson, S., Vrba, J., 1998. Functional neuroimaging by synthetic aperture magnetometry. In: Yoshimoto, T., Kotani, M., Kuriki, S., Karibe, H., Nakasato, N. (Eds.), Recent Advances in Biomagnetism. Tohoku Univ. Press, Sendai, pp. 302-305.

Sekihara, K., Nagarajan, S., 2008. Adaptive spatial filters for electromagnetic brain imaging. Berlin, Heidelberg: Springer-Verlag.

Sekihara, K., Nagarajan, S., Poeppel, D., Marantz, A., 2002. Performance of an MEG adaptive-beamformer technique in the presence of correlated neural activities: effects on signal intensity and time course estimates. IEEE Trans. Biomed. Eng. 49 (12), 1534-1546.

Sekihara, K., Nagarajan, S., Poeppel, D., Marantz, A., 2004. Asymptotic SNR of scalar and vector minimum-variance beamformers for neuromagnetic source reconstruction. IEEE Trans. Biomed. Eng. 51 (10), 1726-1733.

Van Drongelen, W., Yuchtman, M., Van Veen, B.D., Van Huffelen, A.C., 1996. A spatial filtering technique to detect and localize multiple sources in the brain. Brain Topogr. 9 (1), 39-49.

Van Veen, B.D., Van Drognelen, W., Yuchtman, M., Suzuku, A., 1997. Localisation of brain electrical activity via linearly constrained minimum variance spatial filtering. IEEE Trans. Biomed. Eng. 44 (9).